

FERRITIN NANOCONJUGATES FOR AUGMENTING CANCER PHOTODYNAMIC THERAPY AND IMMUNOTHERAPY

by

XUEYUAN YANG

(Under the Direction of Jin Xie)

ABSTRACT

Photodynamic therapy (PDT) is an effective modality for cancer treatment where light is used to activate photosensitizers to produce toxic radicals, by direct destruction on cancer cells, tumor vascular damage, and initiation of immune response. However, the immunity induced by PDT is often inadequate to prevent systemic tumor control or tumor recurrence, because of immunosuppressive mechanisms involved in tumor microenvironment. Cancer immunotherapy is a recent discovered anti-cancer treatment, which aims to train immune cells by targeting immunoregulatory mechanisms to achieve tumor eliminating effect, such as PD-1/PD-L1, CTLA-4, indolamine-2,3-dioxygenase (IDO), etc. IDO is an enzyme that catabolizes tryptophan to kynurenine, and recruits immunosuppressive immune cells into tumor to suppress immune system. Therefore, synergizing PDT with cancer immunotherapy targeting IDO holds great potential in anti-cancer therapies. In the first chapter, we developed PPF nanoparticles (PPF NPs) for simultaneous PDT and immune checkpoint blockage therapy at an optimal rate, which is consisted of two nanocomponents, PLGA-PEG nanoparticles carrying IDO inhibitor, NLG919, and zinc hexadecafluoro-phthalocyanine (ZnF_{16}Pc) encapsulated in ferritin. When tested in murine melanoma tumor model, we found that the treatment caused excellent tumor suppression while

eliciting a strong anticancer immunity that effectively rejected a second inoculation with live cancer cells to prevent tumor relapse.

Except the involvement in cancer treatments, nanomedicines can also be applied in anti-inflammatory therapies, either as carrier to deliver anti-inflammatory agents to lesion or itself to against inflammation. In the second chapter, we developed dopamine melanin nanoparticles (DM NPs) to scavenge free radicals for osteoarthritis treatment. Unlike small molecules, DM NPs, with the size of ~110 nm, showed prolonged retention time in the joint, sustained radical suppression, great inflammatory cytokines management, slowed down the cartilage degradation. In the third chapter, we designed Tanshinone IIA loaded PLGA-PEG nanocarrier for anti-inflammatory purpose. Tanshinone IIA, an effective anti-inflammatory drug, tends to aggregate together under aqueous solution, which lower its administration effectiveness, bioavailability, and may cause side effects. Owing to the hydrophilicity given by PLGA-PEG NPs, hydrophobic Tanshinone IIA has the possibility to effectively reach to the lesion with enhanced stability and bioavailability for ischemic stroke treatment.

INDEX WORDS: cancer immunotherapy; ferritin; indoleamine 2,3-dioxygenase;
nanoparticles; photodynamic therapy, anti-inflammatory

FERRITIN NANOCONJUGATES FOR AUGMENTING CANCER PHOTODYNAMIC
THERAPY AND IMMUNOTHERAPY

by

XUEYUAN YANG

BE, Chengdu University of TCM, China, 2016

A Dissertation Submitted to the Graduate Faculty of The University of Georgia in Partial
Fulfillment of the Requirements for the Degree

DOCTOR OF PHILOSOPHY

ATHENS, GEORGIA

2021

© 2021

XUEYUAN YANG

All Rights Reserved

FERRITIN NANOCONJUGATES FOR AUGMENTING CANCER PHOTODYNAMIC
THERAPY AND IMMUNOTHERAPY

by

XUEYUAN YANG

Major Professor:	Jin Xie
Committee:	Jeffrey Urbauer
	Leidong Mao

Electronic Version Approved:

Ron Walcott
Vice Provost for Graduate Education and Dean of the Graduate School
The University of Georgia
May 2021

ACKNOWLEDGEMENTS

I would like to thank all people who taught, cared, assisted, and sometimes gave me suggestions to help me grow during my Ph.D. study. First, I want to thank my advisor, Pro. Jin Xie, for all the help, support, guidance, patience and suggestions he gave to me to learn how to manage my research and study. He is a great scientist and an excellent leader with knowledge, integrity, rigor, enthusiasm, which inspired me to learn and conduct my research projects with ambition.

Also, I would like to thank all members in our group and all the help, constructive advice they gave to me in my research and my life. I gained a lot from all of you, not only the experimental skills, techniques, but also, the skills of how to show support and help each other, how to give a great presentation, how to live a great life with caring friends.

Finally, I would like to thank my families in China, my mom, dad, naughty little sister and my grandparents for being supportive to my study, always picking up my phone whenever I miss you, giving me advice and helping me to think positively whenever I feel stressed and depressed.

TABLE OF CONTENTS

	Page
ACKNOWLEDGEMENTS	iv
LIST OF TABLES	viii
LIST OF FIGURES	ix
 CHAPTER	
1 INTRODUCTION AND LITERATURE REVIEW	1
Photodynamic therapy	1
Immune checkpoint blockades and cancer immunotherapy	10
Indoleamine-2,3-dioxygenase (IDO) as a target in cancer immunotherapy	14
Nanomedicines in cancer therapy	21
Nanomedicines in combination therapy.....	26
Nanoparticles as anti-inflammatory treatment.....	27
Dissertation focus and outline.....	29
2 NANOCONJUGATES TO ENHANCE PDT-MEDIATED CANCER IMMUNOTHERAPY BY TARGETING THE INDOLEAMINE-2,3- DIOXYGENASE (IDO) PATHWAY	31
Abstract	32
Introduction.....	32
Results and Discussion	34
Conclusion	45

Materials and Methods.....	46
3 DOPAMINE-MELANIN NANOPARTICLES SCAVENGE REACTIVE OXYGEN AND NITROGEN SPECIES AND ACTIVATE AUTOPHAGY FOR OSTEOARTHRITIS THERAPY	52
Abstract	53
Introduction.....	53
Results.....	55
Discussion	69
Conclusion	71
Materials and Methods.....	71
4 INTRACISTERNAL ADMINISTRATION OF TANSINONE IIA-LOADED NANOPARTICLES LEADS TO REDUCED TISSUE INJURY AND FUNCTIONAL DEFICITS IN A PORCINE MODEL OF ISCHEMIC STROKE	82
Abstract.....	83
List of abbreviations	84
Introduction.....	85
Results.....	89
Discussion	102
Conclusion	106
Materials and Methods.....	106
5 CONCLUSTIONS AND FUTURE WORK.....	116
REFERENCES	118
APPENDICES	

A	Supporting information for Chapter 2.....	157
B	Supporting information for Chapter 3.....	162
C	Supporting information for Chapter 4.....	166

LIST OF TABLES

	Page
Table 1.1: Overview of photosensitizers and their applications	4
Table 1.2: Overview of IDO-mediated tryptophan catabolism inhibitors in clinical trials	20
Table 1.3: Nanomedicines in cancer therapy via IDO inhibition pathway	23
Table 1.4: Ferritin-based nanomedicines in PDT	25
Table 1.5: Nanoplatfroms used in inflammatory diseases	28

LIST OF FIGURES

	Page
Figure 1.1: Mechanism of ROS generation by photodynamic therapy.	2
Figure 1.2: Three main mechanisms of PDT-mediated tumor elimination.	9
Figure 1.3: Mechanisms in suppression effector T cells activation.....	12
Figure 1.4: Mechanisms involved in IDO-mediated immune suppression.....	18
Figure 1.5: Binding mechanism of NLG919 to IDO1	19
Figure 2.1: Preparation of characterizations of PPF NPs	35
Figure 2.2: Drug release and IDO inhibition efficiency	37
Figure 2.3: <i>In vivo</i> treatment efficacy	39
Figure 2.4: Antitumor immune response elicited by the combination therapy.....	42
Figure 2.5: Potential side effects caused by the combination treatment.....	44
Figure 3.1: Physical characterizations of DM nanoparticles	56
Figure 3.2: DM nanoparticles as a radical scavenger	57
Figure 3.3: Chondro-protective effects of DM nanoparticles on IL-1 β - induced chondrocytes ...	58
Figure 3.4: Effect of DM nanoparticles on the treatment of OA	61
Figure 3.5: Effect of DM nanoparticles on the oxygen free radicals and autophagy	63
Figure 3.5: Effect of DM nanoparticles on the oxygen free radicals and autophagy	63
Figure 3.6: Effect of DM nanoparticles on ACLT-induced OA.....	67
Figure 4.1: Baic, Piog, and Tan IIA are capable of undergoing NP packaging.....	91

Figure 4.2: Tan IIA-NPs show significantly reduced toxicity in NSCs than freeform drug and Tan IIA-NPs and Baic-NPs reduce oxidative stress in NSCs.....	93
Figure 4.3: Tan IIA-NPs reduce hemispheric swelling, MLS, and ischemic lesion volumes	95
Figure 4.4: Tan IIA-NPs lead to reduced cytotoxic edema and WM damage post-ischemic stroke	95
Figure 4.5: Tan IIA-NPs lead to reduced hemorrhage post-ischemic stroke.....	98
Figure 4.6: Spatiotemporal and kinetic gait deficits are less severe post-stroke in Tan IIA-NP treated pigs	101

CHAPTER 1

INTRODUCTION AND LITERATURE REVIEW

Photodynamic therapy

Light has been used as therapy over thousands of years.^{1, 2} At the end of the nineteenth century, Niels Finsen developed “phototherapy” or the use of light to treat diseases, which was the beginning of the modern light therapy, and, in 1903, Finsen was awarded a Nobel Prize for his discoveries.³ At the same year, Herman Von Tappeiner and A. Jesionek topically applied eosin and white light to treat skin tumors, which was termed as the “photodynamic therapy” later.³

The modern photodynamic therapy (PDT) is a modality with superior merits compared to the conventional cancer therapy, owing to its minimal invasiveness, repeatability without cumulative toxicity and reduced morbidity.⁴ In recent decades, PDT has been used in the treatment of non-oncological diseases as well as cancers of various types and locations, in which nontoxic photosensitizer (PS) is administered locally or systemically, followed by activation of light at a specific wavelength in an oxygen-dependent manner, leading to the generation of cytotoxic species and consequently to cell death and tissue destruction.^{3, 5, 6} When the specific wavelength light is applied on PS, energy from light can be absorbed by ground state (singlet state) PS and aid PS migrating to excited state (triplet state) via a short-lived excited singlet state and intersystem crossing. Then, the photochemical process of PS in the excited triplet state is undergoing two different pathways (**Figure 1.1**).^{6, 7} First, it can directly react with a substrate such as the cell membrane or biomolecule, and transfer a hydrogen atom or electron to produce radical cation or

anion, which can further interact with molecular oxygen to produce oxygenated products, specifically, the form of superoxide anion radical ($O_2^{\bullet-}$), subsequently giving the hydrogen peroxide (H_2O_2) or hydroxyl radical (HO^{\bullet}), leading to the elevated oxidative stress rising the devastation of cells (type I reaction).³ Second, the triplet can transfer its energy directly to oxygen to produce singlet oxygen species (1O_2), while it can go back to the ground state, which is characterized by extremely oxidizing properties causing cancer cell death (type II reaction).³ Both reactions occur simultaneously, but type II reaction plays major role in cell destruction. The cell damage efficiency induced by PDT or therapeutic outcome are multifactorial and depend on several aspects of the three basic elements involved in PDT, including types and localization of PS, dosage and delivery mode of light, and oxygen availability.³

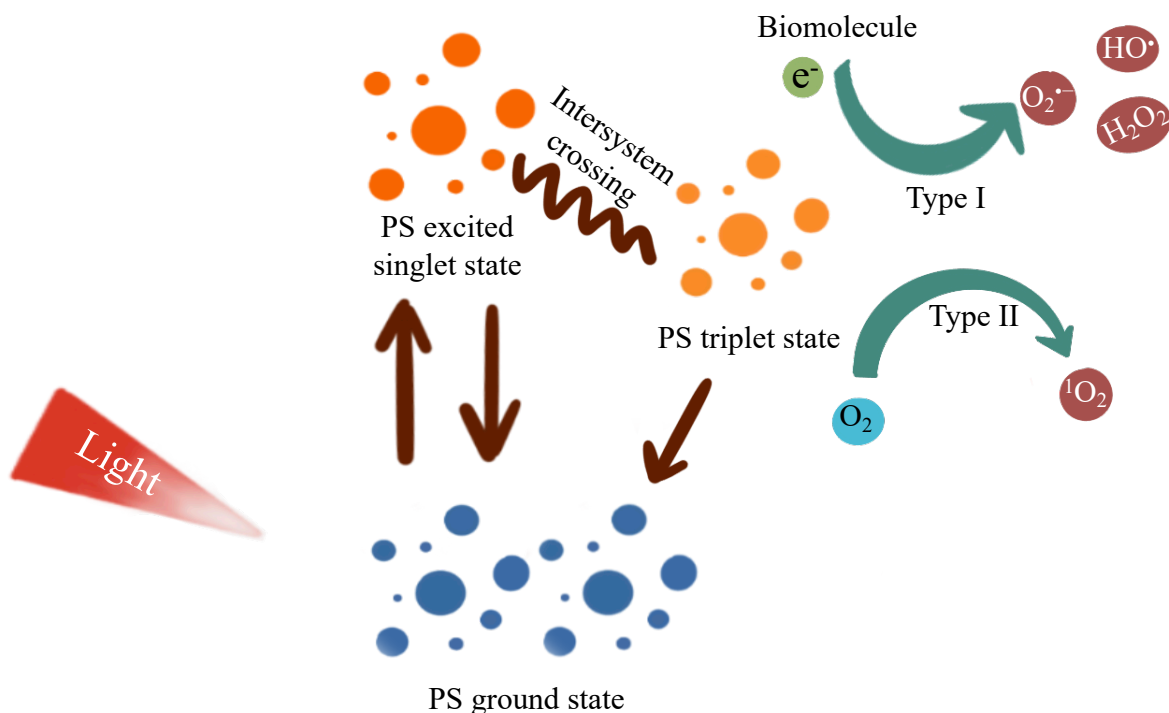


Figure 1.1. Mechanism of ROS generation by photodynamic therapy.

Effects of photosensitizer, light and oxygen on PDT

Over the decades, trends in PDT have led to a proliferation of studies that multiple PSs have been discovered, moved into clinical trials, and some of them are clinically approved as effective treatments in various diseases.⁸ In general, PSs are divided into three generations based on the time of development and achievements (**Table 1.1**). The first generation photosensitizers, hematoporphyrin derivatives (HpD), were applied in early clinical trials of PDT, which showed great effects on various tumors.⁹ In 1993, the first PDT reagent, Photofrin[®], was clinically approved by U.S. Food and Drug Administration (FDA) and the European Medicine Agency (EMA) for the use in the clinic to treat various types of cancer and pre-cancer.⁸ Even though HpD are the most widely used PS for cancer treatment, but they has some limitations, such as low light absorption, poor tissue specificity and inadequate tissue penetration of light.¹⁰ Thence high dosage of HpD is needed for sufficient therapeutic effect, which may result in prolonged patient skin sensitivity after PDT.¹¹ This led to the development of second generation PSs that are consisted of all sorts of porphyrins generally divided into porphyrins, chlorins, pheophorbides, bacteriopheophorbides, texaphyrins and phthalocyanines, which possess high purity, reproducibility, reduced overall drug dose and tumor selectivity.^{9, 12} Besides these remarkable properties, the improvements of second generation PSs, which can be activated by the light at a longer wavelength, are revealed by the faster clearance, shorter circulation half-life, deeper light penetration to tissue, compared to the first generation.^{8, 9} However, PSs are normally facing low accumulation in site of action and low bioavailability, since most of the PSs are hydrophobic and tend to aggregate together. Thus, the third generation PSs are developed, which come from the modified second generation PSs by conjugating to or encapsulated within carrier molecules, such as nanocarriers, monoclonal antibodies (mAbs), liposomes and polymers to achieve designed size,

structure, surface charge, or other specific properties via the functional groups, and, improve their physical, chemical and therapeutical performance.^{8, 13} By conjugating with monoclonal antibodies, the third generation PSs can be delivered to the targeting lesion specifically to augment the bioavailability of PSs or the accumulation in tumor tissue, causing designated damage to the tumor tissue while leaving healthy normal tissue unaffected.¹¹ Also, when the PSs packaged within the nanocarrier, the toxicity of the therapeutics is largely diminished because of the biocompatible materials applied in the preparation of nanocarriers, which also aid to increase the circulation half-life of PSs to get enhanced therapeutic outcome.

Table 1.1. Overview of photosensitizers and their applications

Generation	Photosensitizer	Applications	Ref.
1 st Generation	Hematoporphyrin derivative (HpD)	Mesothelioma, glioma, brain tumor, advanced gastrointestinal cancer	⁹
2 nd Generation	Benzoporphyrin derivative monoacid (BPD-MA)	Ovarian cancer cells	¹⁴
	N-aspartyl chlorin e6, NPe6	Human cholangiocarcinoma	¹⁵
	5'-Aminolevulinic acid (5-ALA)	Basal cell carcinoma, squamous cell carcinoma	¹⁶
	Phthalocyanines	Cutaneous T-cell lymphoma, squamous cell carcinoma, human hepatocellular carcinoma, breast malignancy	¹⁷
	Chlorin	Human lung adenocarcinoma	¹⁸
	Bacteriochlorin	Bacteria	¹⁹
	Methylene blue	Head and neck cancer	²⁰

	Toluidine blue	Bacteria	21
3 rd Generation	Antibody- bis(triethanolamine)Sn(IV) Ce6 conjugates	EDB domain of fibronectin*	22
	Glycoconjugated Porphyrins	HeLa cells	23
	Galactose-phthalocyanines conjugates	Human hepatocellular carcinoma	24
	Saccharide-porphyrin conjugates	Human breast cancer cell	25
	RGD motif-chlorin conjugates	Murine mammary carcinoma	26
	Arginine oligopeptide-TPC conjugates	Human breast carcinoma	27
	Graphene oxide-Ce6 conjugates	Human lung cancer cell	28
	Gold nanorod-Ce6 conjugates	Human lung cancer cell	29
	ZnF ₁₆ Pc loaded RGD4C- modified ferritin	Human glioblastoma cells	30
	ZnF ₁₆ Pc loaded fibroblast- activation protein-modified ferritin	Murine breast carcinoma	31
	Ce6 loaded nanoparticles	Murine melanoma	32

* a component of modified extracellular matrix that surrounds tumor blood vessels' endothelia cells.²²

In addition, the precise localization of PS on or in the cell is crucial for therapeutic outcome by evoking different cell death pathways or impairment.⁸ In 1991, Moan and Berg discovered that the half-life of singlet oxygen in biological systems is less than 40 ns, and, therefore, singlet oxygen's radius of action is within 20 nm.³³ Because of the high reactivity and extreme short half-life of the singlet oxygen and radicals, only molecules or structures that are proximal to the region of their production, or the localization of PS, are affected by PDT.⁵ For example, PSs that localize to mitochondria are most likely to induce apoptosis.³⁴ This is because the photodamage that induces permeabilization to the membrane of mitochondria, causing the leakage of cytochrome c into the cytosol, initiating the caspase mediated apoptotic pathway.³⁵ Also, PSs that located in the plasma membrane are able to trigger necrosis, resulting in leakage of intracellular materials to the *in vivo* milieu which can arise local inflammation and systemic immune response via the cross-talk between innate and adaptive immune system.⁷

The clinical efficacy of PDT also depends on the properties and delivery mode of light.⁶ There are several light sources used for PDT, such as ultraviolet light (330-400 nm), red light (600-700 nm) and near infrared (NIR) light (700-1000).¹⁰ In general, light penetration was reported to be ~3 mm underneath of the skin, and light at longer wavelength has the capability to penetrate deeper tissue than short wavelength.³⁶ Theoretically, we can employ the PS in the hidden tumor treatment, which is activated by the light at an extreme long wavelength, such as over 800 nm. However, light up to 800 nm can generate $^1\text{O}_2$, since longer wavelengths have insufficient energy to initiate a photodynamic reaction.^{36, 37} As such, the window for light used in majority PDT application lies in the red region of the spectrum between 620 to 800 nm achieving optimal tissue penetration and PS activation.⁸ Delivery mode of light, which is another important factor influencing therapeutical effect, includes conventional lamp, laser and light emitting diodes

(LEDs).^{6, 8, 10} Conventional lamp was the most common light applicator for topical lesions or disease. Even though it's cheap, safe and has broad emission that can be applied on several PSs, it has several inadequacies include significant thermal effect, low light intensity, and difficulty in controlling light dose.⁸ So far, laser is extensively employed in clinical PDT as it is powerful, provides monochromatic light of a specific wavelength, and also, can be used to irradiate hidden located tumors via optical fibres.⁶ LED is another emerging light source in PDT, which can provide light of specific bandwidth between 350 to 800 nm in a variable power for a broad range of PSs.⁶ Except providing the broad range of wavelength, LED holds several potentials, like affordable, easy to manufacture, high-power output.⁶ Another parameter that can influence therapeutic outcome of PDT is the availability of oxygen within the tissues. Oxygen shortage can happen as a result of the photochemical consumption of oxygen during the photodynamic process.^{36, 37} Previous studies have found that rapid and considerable reduction in the tissue oxygen tension during and after irradiation of photosensitized tissue, leading to the ROS diminution extenuating PDT therapeutic effect.^{38, 39}

Mechanisms of PDT-mediated tumor elimination

It is now known that PDT has been clinically approved cancer therapy leading to systemic anti-cancer response, which is mediated by three main mechanisms (**Figure 1.2**).³ Firstly, apoptosis and necrosis of tumor cells are directly caused by ROS or mainly singlet oxygens produced via PDT as mentioned above. However, the distribution of PS in tumor tissues is non-homogenous, and, availability of oxygen within the tissue is limited, which lead to the incomplete tumor elimination.^{3, 5} That is to say the thorough tumor eradication is not relying on this mechanism solely.^{3, 5} As such, cancer cells that have evaded death by the direct photocytotoxic effects of PDT can be destroyed via another mechanism, the indirect influence of PDT on tumor-

associated vascular system.^{8, 37} The viability of tumor cells depends on the amount of nutrients supplied by the blood vessels.⁴⁰ There have been numbers of reports that PDT causing microvascular collapse, leading to severe tissue hypoxia and anoxia.⁴⁰⁻⁴³ Also, it has been reported that ROS damages of vascular endothelial cells activates clotting cascades, aggregate platelets and block vessels by forming thrombi, leading to tumor infarction.^{3, 40} Furthermore, tumor elimination can be also achieved by the third pathway, systemic immune response, which is evoked after PDT application. PDT can exterminate the structure of the tumor and stimulates direct interaction between immune cells and cancer cells, by inducing an acute inflammatory response and immunogenic cell death (ICD), which is any type of cell death eliciting a host-defense immune response that promote tumor managements.⁴⁴ To be more specific, direct destruction in tumor tissue leads to the development of a strong inflammatory reaction and neoplasm infiltration by leukocytes.^{37, 45} Membrane photodamages prime to the initiation of phospholipases and cyclooxygenases, thus, massive inflammatory mediators emitting.⁴⁶ For example, in 1997, Gollnick and her group discovered that the inflammatory cytokines interleukin (IL)-6 and IL-1 have been shown to be upregulated in response to PDT.⁴⁶ In addition, as early as in the late 1980s, and early 1990s, there were several studies ascertained the infiltration of lymphocytes, leukocytes and macrophages into PDT-treated tissue, indicating the crosstalk between cancer cells and immune cells and the activation of the immune response.^{45, 47} Investigation on various cancer using diverse PSs has been conducted and showed promising therapeutic achievements.

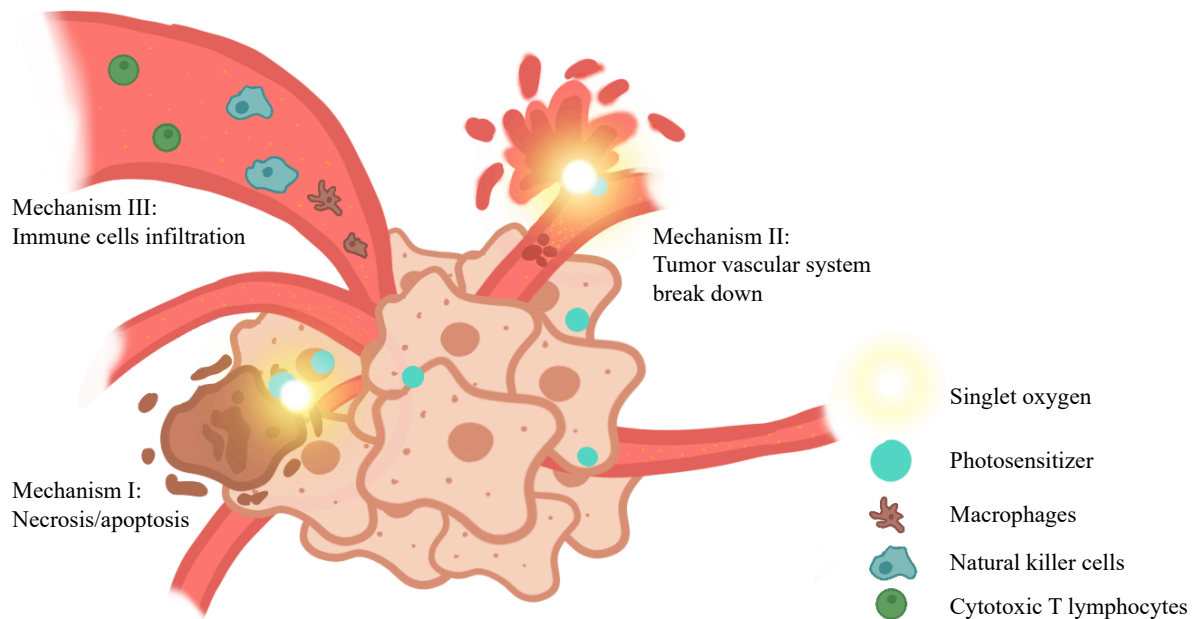


Figure 1.2. Three main mechanisms of PDT-mediated tumor elimination

Challenges remained in PDT

Even though PDT has remarkable properties of insignificant invasiveness, reduced toxicity, etc., PDT as a monotherapy is still facing some challenges or limitations, such as poor phototoxic efficiency, insufficient tumor elimination and long-term tumor control.⁴⁸⁻⁵² One reason is when the local inflammatory response induced by PDT, there might be compensatory anti-inflammatory response induced at the same time to restrict the hyperactive immune responses and thereby reduce nearby tissue damage, during which the expression of anti-inflammatory cytokines or other immunosuppressive modulator are elevated, like interleukin (IL)-10, transforming growth factor- β (TGF- β).^{48, 52} In addition, PDT can induce both apoptotic and necrotic cancer cell death, which may indirectly interfere PDT outcome. There are some studies showed that dendritic cells (DCs) can efficiently activate both cluster of differentiation 4+ (CD4+) and CD8+ T cells (which is also called cytotoxic T lymphocytes, or CTLs) if cancer cell dies through necrosis, while the apoptotic

cells may only lead to CD8⁺ T cell activation, which may become anergic and tolerogenic with absence of CD4⁺ T cells.^{52, 53} Also, it is believed that damage associated molecular patterns (DAMPs) from PDT-treated cancer cells can induce anti-cancer immune responses, such as DNA-binding protein high-mobility group box 1 protein (HMGB1), which is responsible for binding to toll-like receptors to activate immune responses.⁵² However, it has been also reported that ROS produced after PDT weighing an important role in immunoediting process, in which ROS can oxidize HMGB1 resulting in tolerance instead of stimulation.^{52, 54} Another major reason associated with the high tumor recurrence rate is immunosuppressive tumor microenvironment (TME). Even though PDT has the capability to induce anti-cancer immune response, it is inadequate for disrupting or reversing immunosuppressive TME to immune reacting TME, where cancer cells develop several immune-regulatory mechanisms to escape immune attack protecting or promoting tumor.^{44, 55} In an effort to augment the effectiveness of PDT and achieve sufficient immune response eradicating tumor cells and possessing long-term tumor control, it can be beneficial to explore the combination therapy of PDT together with the engagement of cancer immunotherapy.

Immune checkpoint blockades and cancer immunotherapy

Immune cells involved in immunosuppressive mechanisms and TME

The interaction between different immune cells and tumor cells contributes to the development of immune suppression and tumorigenesis, which is a complex and dynamic process.^{48, 56, 57} At the initiation of tumor, natural killer (NK) cells from innate immune system can recognize and kill tumor cells without exposure to tumor associated antigens (TAAs).⁵⁷ Interferon (IFN)- γ released from cytotoxic NK cells promotes the expression of major histocompatibility class I (MHC-I) on cancer cells and MHC-II on antigen-presenting cells (APCs), priming

subsequent T cell responses.^{58, 59} Also, MHC-I molecules and TAAs released from dying tumor cells can be captured by APCs initiating and regulating the anticancer immunity by presenting TAAs to T cells through MHC-II molecules in secondary lymphoid organs, facilitating the connection of innate and adaptive immunities, priming to the activation of effector T cells against tumor.⁵⁹ Activated effector T cells, also the CTLs, are capable to travel through tissues, infiltrate into tumor and bind to cancer cells by identifying TAAs presented on MHC-I molecules, subsequently, leading to cancer cells death in a T cell receptor (TCR) dependent manner.⁵⁹ However, CTLs encounter a tumor immunosuppressive milieu with a variety of mechanisms adopted by tumor cells, which can affect the phenotype and function of CTLs and finally inhibit CTLs' proliferation to give assistance to maintain immunosuppressive TME, avoid immune recognition and immune-mediated destruction.⁴⁸ For example, B7 molecules, include B7-1 (CD80) and B7-2 (CD86) expressed on DCs, a professional APC, bind with CD28, a switch TCR of effector T cell activation, to achieve adaptive immune response initiation.⁶⁰ However, cytotoxic T lymphocyte antigen 4 (CTLA4), an immune checkpoint molecule expressed on T cells discovered by Dr. James Allison in 1990s, can compete with CD28 and bind to B7 molecule at a higher binding affinity, attenuating T cells activation and compromising antitumor immunity (**Figure 1.3**).^{61, 62} In addition, upon TCR stimulation, although CD28 provides critical signals that are essential for T cell activation, programmed death 1 (PD-1), another immune checkpoint target discovered by Tasuku Honjo in 1992, can interfere TCR/CD28 signaling to induce or maintain peripheral tolerance for immune response to avoid immunopathology.⁶³ PD-1, a homology to CD28 expressed on T cells, can be induced through the TCR or the exposure to cytokines, such as interleukin (IL)-2, IL-7, IL-15 and IL-21.^{61, 64} PD-1 has two ligands, PD-L1 and PD-L2, which are found on the surface of APCs and tumor cells.⁶⁵ Engagement of PD-1 leads to the dephosphorylation of TCR proximal

signaling components, through the signaling cascade mediated by immunoreceptor tyrosine-based inhibition motif and immunoreceptor tyrosine-based switch motif on the PD-1 intracellular tail (Figure 1.3).^{61, 66} Therefore, participation of PD-1 leads to the inhibition of T cell receptor-mediated lymphocyte proliferation and cytokine immune response promoting tumor cell growth.

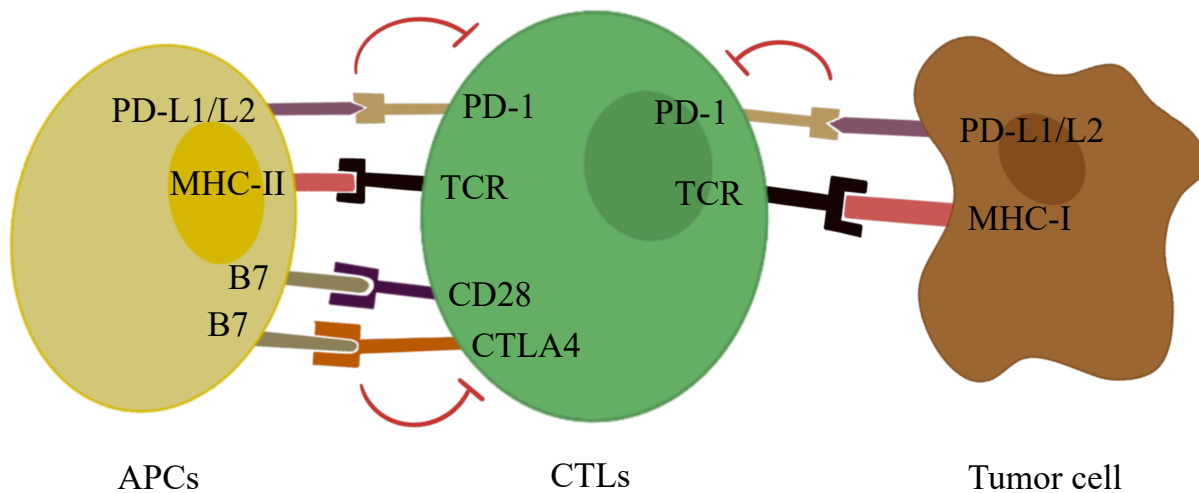


Figure 1.3. Pathways involved in suppressing CTLs' activation

Except immune regulatory mechanisms manipulated by tumor cells to avoid immune attack, there are several immunosuppressive cells also contributing significantly to immunosuppressive TME, such as regulatory T cells (Tregs), myeloid-derived suppressor cells (MDSCs) and so on. To be more specific, activated Tregs can directly suppress T cells by producing anti-inflammatory IL-10 and transforming growth factor- β , which can inhibit co-stimulatory ligands (also known as B7 molecule) expression on dendritic cells.^{67, 68} Also, tumor-infiltrating Tregs have upregulated expression of CTLA-4, hindering T cell stimulation and activation through CTLA-4 pathway.^{59, 68}

Moreover, MDSCs, an immunosuppressive phenotype of tumor-infiltrating macrophages, secrete immunosuppressive agents, such as nitric oxide, arginase and reactive oxygen species (ROS) in tumors.^{67, 69, 70} Also, tumor progression promotes MDSCs infiltrating, which can inhibit CTLs' proliferation and cytotoxicity, to further inhibit adaptive immunity and facilitate tumor progression and metastasis.⁵⁹ Therefore, targeting these immunosuppressive pathways or cells provides great potential for modulating TME systemically and locally, in order to reprogram immune response to cancer.

Cancer immunotherapy reverses immunosuppression

Cancer immunotherapy aims to train the host immune cells in lymphoid tissues and antitumor immune cells in the TME to search for and destroy tumor cells, which has revolutionized oncology and offers new treatment options for many types of cancer.^{31, 59, 67, 71} Antitumor immune responses primed by immunotherapy can stimulate systemic immune surveillance and eliminate local and disseminated metastatic tumors.⁶⁹ Thus, to fully realize the potential of cancer immunotherapy, approaches are needed to intensify anti-tumor T cell immune responses, converting immunosuppressive tumors into immunoreactive tumors and sensitizing tumors to immunotherapies with minimal off-target toxicity and immune-related adverse events.^{67, 72} Owing to the clinical success of immune checkpoint blockade (ICB) therapy, immunotherapy has now been established as a new pillar of cancer treatments.⁶⁷ For example, immune checkpoint blockade therapy targeting PD-1 and PD-L1, CTLA4, have been studied extensively and achieved significant breakthrough in recent years.⁷³ Anti-CTLA4 is mainly working at tumor draining lymph nodes where CD28 stimulation can be involved. In tumor draining lymph nodes, not only anti-CTLA4 antibodies target CTLA4 molecules expressed on effector T cells to release the negative regulation of effector T cells activation, but also they are able to deplete Tregs to induce

aberrant effector T cell activation and give rise to sufficient immune response to tumor.⁷³ Also, based on the molecular mechanisms involved in PD-1 and PD-L1 pathway, antibodies targeting PD-1 or PD-L1 significantly contribute to the upregulation of antitumor immune response, which is mainly occurred in tumor.⁷³ Anti-PD1 antibodies compete with PD-L1 expressed on tumor cells to activate CTLs, while anti-PD-L1 antibodies are utilized to block PD-L1 to prime CTLs activation.⁷³ Also, anti-PD-L1 can block PD-L1⁺ APC cells to block the interaction between PD-L1 and B7 molecule, giving rise to enhanced effector activity.^{73, 74} Conventional cancer treatment modalities, such as surgery, chemotherapy and radiotherapy, have limited efficacy against advanced cancer with adverse off-target toxicity, whereas cancer immunotherapy can ameliorate the toxic effects, augment protective antitumor immunity as an essential component in the curative mechanism, and disrupt the immune-regulatory circuits.⁷² Also, immune checkpoint blockers can be applied to durably eliminate tumors in a subset of patients with advanced metastatic disease, improving patient survival.^{67, 75, 76} Additionally, immunotherapy can establish long-term immune memory and mediate immune protection against tumor recurrence.

Therefore, in an effort to augment the effectiveness of PDT and achieve sufficient immune response eradicating tumor cells and possessing long-term tumor control, it is beneficial to explore the combination therapy of PDT together with the engagement of cancer immunotherapy.⁷⁷⁻⁷⁹

Indoleamine-2,3-dioxygenase (IDO) as a target in cancer immunotherapy

IDO-mediated Trp catabolism

Indoleamine-2,3-dioxygenase (IDO), a heme-containing intracellular enzyme, is an immune checkpoint element frequently involved in immunosuppress TME, which catalyzes the first and rate-limiting step in tryptophan (Trp) catabolism.⁸⁰ Trp is an essential amino acid, which is

important for cell survival and involved in a variety of physiological regulation and processes, such as being a precursor for serotonin, melatonin and proteins.⁸⁰ Besides these physiological pathways Trp are tangled in, Trp can be oxidized into kynurenine (Kyn) by IDO pathway that cleaves the 2,3-double bond of the indole ring in Trp molecule with the incorporation of molecular oxygen merging into the unsealed molecule to produce *N*-formylkynurenine, which then transforms into Kyn rapidly and spontaneously.^{80, 81} There are three types of enzymes that control Trp homeostasis, IDO1, IDO2 and tryptophan-2,3-dioxygenase (TDO). In human, IDO is encoded by IDO1 gene, which is widely expressed in various tissues and cells, such as lungs, placenta and peripheral lymph organs, endothelial cells, APCs, fibroblasts, macrophages, DCs and cancer cells.⁸² In general, IDO1 has been shown to be upregulated in tumor site compared to normal tissues or organs, which is attributed by not only cancer cells that constitutively express IDO1 or are stimulated to do so by tumor infiltrating immune cells that secrete inflammatory cytokines, IFN- γ , but also tumor infiltrating dendritic cells that also express high level of IDO1.⁸³⁻⁸⁵ However, IDO2 is more narrowly expressed than IDO1 and has only 3-5 % enzymatic activity of IDO1, with the similar suppressive effect on the proliferation of CD4⁺ and CD8⁺ T cells as IDO1.⁸³ Also, the majority of systemic Trp catabolism is attributed by IDO1, while IDO2 enzymatic activity is associated with particular subcellular localization, such as perinuclear/nuclear in liver.⁸⁶ It is worthy to mention that although the functional difference between two enzymes have been reported, their accurate contributions to immune regulation is not yet completely understood.^{84, 87,}
⁸⁸ Subsequently, IDO1 and IDO2 in immunoediting or immunoregulating field are sometimes referred as “IDO” collectively. Another type of Trp catabolic enzyme is TDO, which has much lower expression level than IDO, and distributed in different tissues than IDO and additionally present in bacteria.^{83, 89}

Actions involved in IDO-mediated immune suppression and tumor progression

IDO was originally describes as a mediator regulating innate immune response that defends the host organism against infections.⁹⁰ However, recent studies show that IDO is correlated with poor patient prognosis in various cancer types and involved in multiple mechanisms in building immunosuppressive TME (**Figure. 1.4**).^{74, 83, 91} First, it is believed that IDO is entangled in three phases of immune tumor editing process contributing to the progression of tumor.^{81-83, 92, 93} The first phase of immunoediting is called “elimination”, which means the sporadically appearing transformed cells are recognized and destroyed by immune system, via direct eradication from tumor reactive antibodies produced by activated B cells, and indirect tumor growth inhibition due to Trp starvation in TME.^{81, 83} The second phase is named as “equilibrium” phase, in which existing tumor cells accumulate and mutate rapidly, but are still controlled by the immune system.^{81, 84} In this phase, tumor cells continuously and quickly response and acclimatize to the attack from immunity, whilst cultivating regulatory mechanisms as discussed above to prevent immune system exclusion.^{81, 82} When the immunity no longer blocks or destroys the abnormal and constant growing cells, tumor steps into the third phase, “escape”.⁸¹ High level of IDO is accompanying in this phase, which are predominantly expressed by tumor cells and tolerogenic immune cells, such as tolerogenic DCs, MDSCs, tumor-associated macrophages (TAMs).⁸¹

During these three immunoediting phases or tumor progression, Trp depletion and Kyn production are involved and contributed significantly to build and maintain immunosuppressive TME. Specifically, in TME, Trp is reported to be nearly 100 times lower than in plasma, resulting the significant hindered T cell proliferation and arrested cell cycle in tumor tissue.^{82, 83, 94} Trp depletion leads to the accumulation of uncharged t-RNA, which is subsequently sensed by general control non-depressible-2 (GCN-2) kinase through binding to uncharged t-RNA.^{95, 96} In response

to the activated GCN-2 kinase, protein synthesis is blocked, thus attenuating CD8⁺ T cell proliferation and activation.⁹⁷ In addition, because of the Trp starvation, TCR-zeta (TCR- ζ) chain is downregulated, which is capable to not only jeopardize the cytotoxic effector function of CD8⁺ T cells, but also hinders enzyme synthesis to reduce CD4⁺ T cell proliferation and altering its function by promoting CD4⁺CD25⁺FoxP3⁺ Tregs differentiation.^{95, 96} Trp depletion also upregulate inhibitory receptors expression on DCs to induce tolerogenic DCs, promoting Tregs differentiation, such as immunoglobulin-like transcript (ILT) 3 and ILT4.⁹⁸ Moreover, Trp deprivation suppresses the master metabolic kinase mammalian target of rapamycin complex 1 (mTORC1), which is responsible for protein synthesis coordinating to the diminished amino acid level and controls cell autophagy or growth.^{91, 99} When CD8⁺ T cells face low level of Trp, mTORC1 is downregulated, which initiates cell autophagy.

Moreover, increased Kyn levels are known to suppress NK cells function, prevent the activation of effector T cells, stimulate the differentiation and activation of Tregs by binding to aryl hydrocarbon receptor (AHR), induce the differentiation of tolerogenic DCs, and promote the recruitment of MDSCs to tumor.^{85, 100-105} Kyn and kynurenic acid (KynA) are the catabolites of Trp, which are capable to activate AHR to reprogram immune cells.^{106, 107} It has been reported that Kyn-mediated AHR activation can increase PD-1 expression on CD8⁺ T cell, initiate CD8⁺ T cells mortality, and also, induce Tregs differentiation.^{106, 108} Additionally, anti-inflammatory cytokines induced by DCs are upregulated upon the AHR stimulation, such as IL-10, TGF- β .¹⁰⁹ Also, AHR activation by Kyn promotes C-C motif chemokine receptor 2 (CCR2) and CD39 expression on TAMs, which in turn to aid the recruitment of TAMs into tumor and contribute to the dysfunction of CD8⁺ T cells, respectively.^{91, 110} As such, Trp shortage, Kyn excess and IDO enzymatic activity initiate several pathways to induce and sustain immunosuppressive TME,

which spark the interest in inhibiting IDO-mediated Trp catabolism to abrogate immune suppression to eradicate tumor cells and prevent future tumor recurrence.

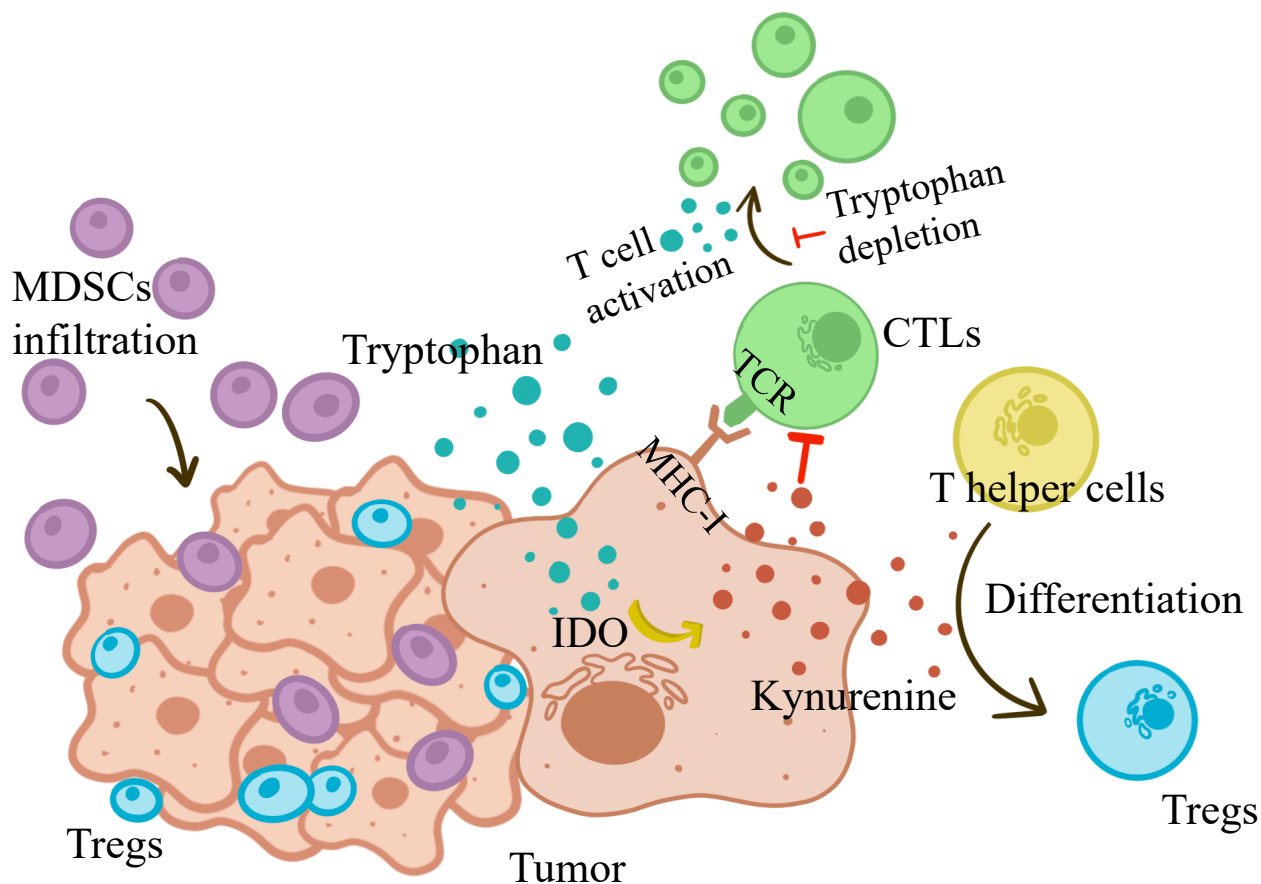


Figure 1.4. Mechanisms involved in IDO-mediated immune suppression

Inhibitors targeting IDO-mediated Trp catabolism

Currently, various studies in preclinic and clinical investigation support that IDO-mediated Trp catabolism represents a potential immune blockade therapy target, and shows amplified tumor suppression effect when synergizing with other treatment modalities, like ICB, chemotherapy, PDT, etc.^{91, 111, 112} There are numerous agents showed great potential in binding to IDO enzyme to

inhibit Trp catabolism, and some of them acquired widespread attention and impelled into clinical investigation (**Table 1.2**). For example, NLG919 or Navoximod is a highly IDO-selective inhibitor with an EC₅₀ of 75 nM and high tumor regression rate, which is normally employed in cancer treatment with other cancer treatment to accomplish augmented therapeutic effects.¹¹³⁻¹¹⁶ NLG919 exhibits great bind affinity to IDO1 protein by binding to the heme iron atom of IDO1 enzyme covalently and locating at the sixth coordination site of heme, via imidazole nitrogen of NLG919, which greatly contributes to IDO inhibition effect.^{117, 118} Not only the covalent bond came from the heme bind site of action promotes the binding of NLG919 to IDO1 enzyme, but also the imidazoleisoindole core and cyclohexylethanol moiety help to situated NL919 within IDO1 enzyme (**Figure1.5**).^{117, 118} Imidazoleisoindole structure can stay in the binding site (pocket A) via the extensive hydrophobic interaction with Tyr126, Cys129, Val130, Phe163, Phe164, Gly262, Ala264 and porphyrin ring.¹¹⁷ Also, because of the strong hydrophobic interaction between cyclohexylethanol with Phe226, Ile354, Leu384 and Arg231 in the adjacent hydrophobic pocket (pocket B), NLG919 can be stabilized and bind to IDO1.¹¹⁷ Therefore, robust binding affinity of NLG919 to IDO1 can compete with Trp to achieve superior IDO1 suppression.^{91, 113}

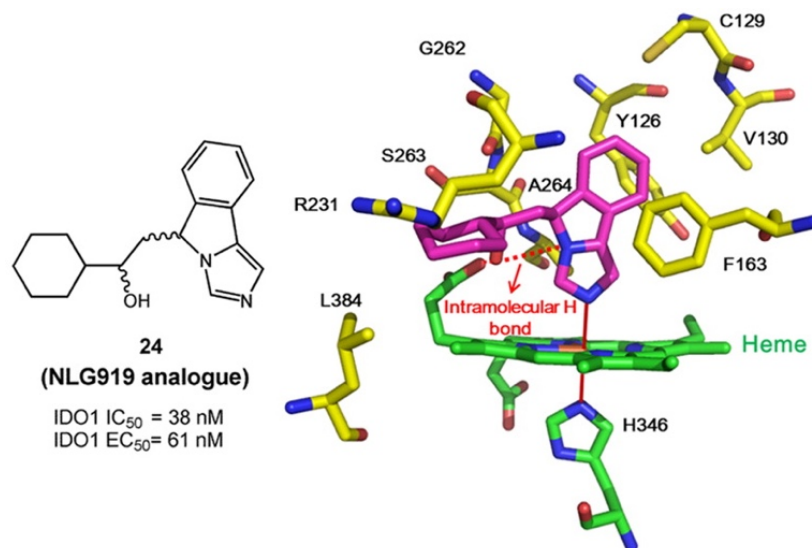
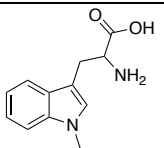
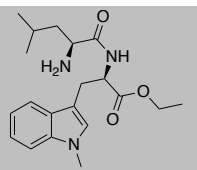
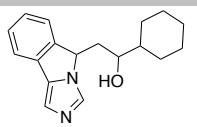
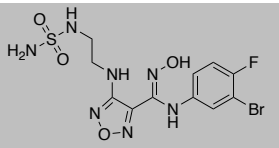
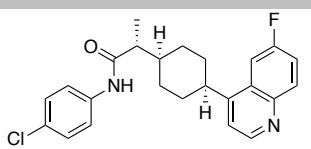
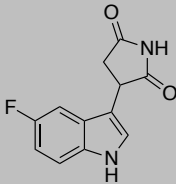


Figure 1.5. Binding mechanism of NLG919 to IDO1. Reprinted with permission from (*J. Med. Chem.* 2016, 59, 1, 282-293). Copyright (2021) American Chemical Society.

Table 1.2. Overview of IDO-mediated tryptophan catabolism inhibitors in clinical trials

Target	Agent	Structure	Clinical Phase	NCT
mTORC1*	Indoximod (NLG-8189)		Phase II	NCT04049669
IDO1	NLG-802		Phase I	NCT03164603
IDO1	Navoximod (NLG919)		Phase I	NCT02048709
IDO1	Epacadostat (INCB024360)		Phase I	NCT03217669
			Phase II	NCT02364076
			Phase II	NCT03414229
			Phase II	NCT03532295
			Phase III	NCT03348904
IDO1	BMS-986205		Phase II	NCT04106414
			Phase I	NCT03192943
			Phase III	NCT03329846
			Phase III	NCT03417037
			Phase II	NCT03854032

IDO1	PF-06840003		Phase I	NCT02764151
IDO1	KHK2455	Not available	Phase I	NCT03915405

* Instead of directly targeting IDO1, Indoximod restores mTORC1 activity, which is pivotal in immunoediting and downregulated in response of Trp depletion.

Nanomedicines in cancer therapy

Conventional cancer therapies tend to apply small molecules for the treatment and management of tumors, which remains fundamental problems to achieve adequate effect to eliminate tumors or deficient accumulation of these small molecule drugs in the site of action, mainly owing to the hydrophobic nature and fast clearance of these small molecules.⁴ Also, conventional cancer treatment generally exhibits some side effects, such as high toxicity for both cancer and healthy cells, acute immune response, etc.¹¹⁹ Different strategies have been employed to overcome the current limitations, often by the means of nanomaterials that not only enables a stable dispersion of these small molecules with improved hydrophilicity, enhanced drug loading and improved tumor uptake over free drugs, but also offers the remarkable capability of a direct effect of drugs on diseased cells and preserve the structure and function of the healthy tissue, preventing the high toxicity associated with conventional small molecule therapies.^{119, 120} Except these excellent properties to provide solution of the shortcomings of conventional therapies, nanomedicines, with 1-100 nm size, possess the merits of a) large surface to volume ratios that can effectively increase the amount of therapeutic agents delivered to the target site; b) capability of preventing prerelease of encapsulated drugs and the potential inactivation caused by plasma components; c) enhanced drug accumulation in tumor owing to the enhanced permeability and

retention (EPR) effect, which is due to the abnormally leaky tumor vascular system and dysfunctional lymphatic drainage within the TME; d) feasibility to be modified or conjugated with conjugating with functional groups, or targeting moieties to be bestowed with multiple functions, such as targeting performance, enhanced cell uptake, prolonged circulation half-life, and so on; e) ability of conjugating with other nanoparticles or carrying multiple cargoes as combination therapy to achieve synergized therapeutic effect and boosted tumor control.¹²⁰⁻¹²⁵ These remarkable merits urge nanotechnology ahead into clinical investigation. One successful example is Abraxane, an albumin-bound paclitaxel nanoparticle, which is approved by FDA as treatment for breast cancer, non-small-cell lung cancer, and pancreatic cancer.¹²⁶

Owing to the remarkable properties aforementioned, a variety of nanoparticles (NPs) with diverse physicochemical properties have been developed for cancer immunotherapy via IDO inhibitive pathway (**Table 1.3**). For instance, poly (lactide-co-glycolide)-polyethylene glycol (PLGA-PEG) nanoparticles is one of the most extensively studied nanocarriers that offers excellent biocompatibility and biodegradability.¹¹⁹ PLGA-PEG nanoparticles is prepared by PLGA-PEG amphiphilic copolymer with the string of hydrophobic PLGA chain and hydrophilic PEG chain, which are approved by FDA in clinical application.¹²⁷ Also, PLGA-PEG nanoparticles can undergo slow hydrolysis to produce nontoxic metabolizable monomers, lactic acid and glycolic acid, followed by metabolism via Krebs cycle and removal as carbon dioxide and water.^{127, 128} Also, nanoparticle with a hydrophilic surface is more favorable to escape from natural defense systems, molecular phagocytic system, which means hydrophilic PEG has the ability to grant polymeric nanoparticle with a biocompatible mask to extend nanoparticles' circulation time accomplishing sufficient accumulation in targeted area.¹²⁷ Owing to the exceptional nature of PLGA-PEG copolymer, a variety of hydrophobic molecules can be encapsulated in PLGA-PEG

nanoparticles to avoid aggregation and increase its bioavailability via hydrophobic-hydrophobic interaction with PLGA end. By enveloping hydrophobic drug in its cavity, PLGA-PEG nanoparticles offer prodrug with thermodynamic biostability, even distribution in aqueous system, long circulation, as well as enhanced accumulation in tumor area, due to EPR effect.^{127, 128} Therefore, the above mentioned potent IDO inhibitors can take advantage of PLGA-PEG nanoparticle to better and elevate its chances in clinical evaluation.

Table 1.3. Nanomedicines in cancer therapy via IDO inhibition pathway

Agents	Nanoformulation	Tumor Model	Ref.
NLG919	Polymeric nanoparticle	4T1	129
Indoximod	Liposome	4T1	130
Epacadostat	Polymeric nanoparticle	B16F10	131
NLG919	Liposome	4T1	114
Indoximod	Mesoporous silica nanoparticle	KPC	132
NLG919	Polymeric nanoparticle	4T1	115
Indoximod	Liposome	4T1	133

In addition, nanoparticles are not only widely utilized in IDO inhibition, but also in PDT to bestow PS with amplified solubility and stability in bioenvironment, ameliorated overall photosensitivity, augmented specificity to tumor and retention in tumor tissues, etc.⁴ As mentioned and summarized above, small molecule PSs are generally hydrophobic and tend to aggregate under aqueous bioenvironment. Encapsulating in nanocarriers or conjugates with other molecules assists therapeutic PS to accumulate in tumor area at an adequate dose and improved pharmacokinetic

properties.⁴ Currently, there are plentiful nanoplateforms that are utilized for PDT, which generally categorized into two, a) nanocarriers encapsulated with PSs, such as polymeric nanoparticles,¹³⁴ liposomes,¹³⁵ mesoporous silica nanoparticles,¹³⁶ dendrimer based nanoparticles,¹³⁷ PS-modified gold nanoparticles,¹³⁸ etc.; and b) PSs by itself, such as fullerenes,¹³⁹ titanium dioxide nanoparticles,¹⁴⁰ Zinc oxide nanoparticles,¹⁴¹ etc.⁴ Among them, ferritin (FRT), is a fascinating nanocarrier that spark the interest in the field of photodynamic nanomedicines (**Table 1.4**).

FRT, a hollow globular intracellular protein, presents in every cell type, which acts as the primary iron transportation mechanisms, stores iron in a non-toxic form and recycled it in a controlled fashion.^{126, 142} FRT is composed of 24 subunits of light chain and heavy chain (L-chain, 19 kDa; H-chain, 21 kDa).¹²⁶ The molecular weight FRT alters when the composition of L-chain and H-chain vary, leading to different types of FRT in various tissues or species.¹⁴² For example, H-chain is the major component in FRT located in human heart tissue, while L-chain in FRT is overly expressed in human liver tissue.¹⁴² Also, ferritin in vertebrates is consisted of both light and heavy chains at a mass of ~450 kDa, while FRT in plants and bacteria is mostly composed by H-chain, leading to a higher molecular weight, ~500 kDa.¹⁴² The inner and outer diameter of FRT is about 8 nm and 12 nm, respectively, with an unique property that 24 subunits can dissociate at acidic environment and self-assemble back into original cage-like structure at neutral conditions.¹²⁶ The interior room of FRT is general occupied by iron as ferrihydrite, which can store up to ~4500 iron atoms.¹²⁶ It has been reported that not only iron can be deposited in the cavity, but also other metallic species and hydrophobic molecules can be encapsulated in apo-ferritin, such as Cu, Co, zinc hexadecafluorophthalocyanine (ZnF₁₆Pc), and so on.^{30, 143, 144} In addition, the surface of FRT presents multiple functional groups that can be modified as a bridge to connect with other moieties to achieve multifunction, such as carboxyl acid group (Aspartic acid and

Glutamic acid), amine group (Lysine), thiol group (Cysteine), etc.¹⁴² These multifaceted characterizations bestow FRT as an ideal delivery vector for a variety of drugs. Not only the high loading efficiency that FRT possesses, but also minimal immune response could be induced by FRT owing to its exceptional nature.¹²⁶ FRT as a nature protein found in every cell type causes almost minimal immune response or side effect, leading to less clinical concerns than traditional synthetic carriers.^{126, 145}

In recent decades, FRT as nanocarrier has been extensively studied and applied in various treatment, showing great potential in tumor management compared to traditional therapies.¹⁴⁶⁻¹⁴⁸ Among them, FRT has been widely discovered by our group as a nanovector in PDT.^{30, 31, 146, 149-151} ZnF₁₆Pc, a metal containing potent photosensitizer, showed high loading efficiency in FRT, up to 60 wt%.³⁰ ZnF₁₆Pc can be activated by 671 nm laser to produce ¹O₂ to cause damage to surround cells or organisms.^{30, 146} However, ZnF₁₆Pc is a highly insoluble photosensitizer and tend to aggregate in aqueous environment, which limited its clinical evaluation. With the assistance of FRT, the hydrophilicity of ZnF₁₆Pc and its homing to tumor tissue are greatly enhanced when systemically injected, exhibiting great improvement in tumor suppression.³⁰ Therefore, FRT, as a nanocarrier, is a promising candidate in the field of photodynamic nanomedicines with long circulation half-live, low toxicity, easy surface modification and high loading capacity.

Table 1.4. Ferritin-based nanomedicines in PDT

Photosensitizers	Ferritin-based Nanoformulation	Tumor Model	Ref.
Zinc(II) phthalocyanine (ZnPc)	Caspase-3 specific substrates and black hole quencher-3 (BHQ3) modified ferritin	MDA-MB-435	145

Sinoporphyrin sodium (DVDMS)	RGD-modified ferritin	4T1	152
ZnF ₁₆ Pc	Single chain variable fragment (scFv) modified ferritin	4T1	149
ZnF ₁₆ Pc	Single chain variable fragment (scFv) modified ferritin	bilateral 4T1 tumor models	153
ZnF ₁₆ Pc	RGD-modified ferritin	U87MG	30
ZnF ₁₆ Pc	RGD-modified ferritin	4T1, U87MG, and PC-3	151
ZnF ₁₆ Pc	Folic acid modified ferritin	4T1	150
Manganese phthalocyanine (MnPc)	anti-EGFR modified ferritin	A431	154

Nanomedicines in combination therapy

As mentioned above, tumorigenesis are complex and dynamic activities, which involved in multiple mechanisms. Even though PDT can induce direct destruction on tumor cells and initiate innate and adaptive immune responses against tumor cells owing to ICD, but the monotherapy is still facing the incompetency to achieve complete tumor elimination and long-term tumor control.^{67, 155} This is because of not only the immunity induced after PDT is too weak to reprogram or reverse established immunosuppressive TME, but also it may provoke anti-inflammatory cytokines and oxidize DAMPs to abolish anti-tumor immune response as aforementioned. Therefore, the synergy of PDT with IDO-targeting cancer immunotherapy by the means of nanomedicines not only aims to prime the TME and to reprogram immune cells response to enhance therapeutic effect, but also offers a promising strategy to address current limitations faced

by the field of conventional cancer treatment or monotherapy to achieve systemic antitumor immunity and advanced long-term tumor management.⁷⁷⁻⁷⁹

Currently, there are two types of nano-formulations employed in combination therapy, nanoparticle comprised of more than one prodrug, or nanoconjugates consisted of more than one nanocomponent. In general, nanoparticle encapsulated with more than one prodrug tends to release all therapeutic agents slowly and simultaneously in the bioenvironment. The released molecules are associated with variable hydrophilicity and pharmacokinetics, that is to say agents may be excluded from body with different half-life, which may end with undesired insufficient accumulation in targeted tissue limiting its clinical evaluation. Also, it is hard to control the actual drug ratio at a desired place, which may affect therapeutic outcome, due to distinctive half maximal effective concentration (EC_{50}) of these molecules. However, nanoconjugates can overcome these shortcomings, owing to a sophisticatedly designed platform by enveloping therapeutic agents in separate nanocomponents, followed by conjugating them together to be one synergized nanovector. As such, based on the nature of prodrug, it is feasible to choose the appropriate nanocarrier to carry specific drug, leading to a controllable releasing profile in bioenvironment. Also, according to the purpose of the treatment, separately enveloped molecules in nanoconjugates can be manufactured at an optimal ratio to maximize their bioevaluation and achieve preferred therapeutic effects.

Nanoparticles as anti-inflammatory treatment

Except being a potent therapeutic in cancer treatment, nanomedicine can also apply in inflammatory diseases. Unlike the traditional anti-inflammatory medications, which are non-selective with adverse effects and limited delivery efficiency, sophisticatedly designed nanomedicines showed reduced side effects, capability to target lesions specifically, augmented

delivery efficiency.¹⁵⁶ Nanomedicines generally reach their site of action by passive and active targeting to the specific tissues, via the functional groups on surface of these nanocarrier manipulated to conjugated with additional molecules/materials.^{119, 157} Various types of nanoparticles exploited in inflammatory diseases have been developed, which can be divided into two categories (**Table 1.5**). The first one is to operate as drug delivery vehicle to dispatch encapsulated anti-inflammatory agents to the site of inflammation, such as polymeric nanoparticles, liposomes, etc.^{119, 158} Most of the materials used in synthesizing these nanocarriers are biocompatible, suggesting reduced immune responses and decelerated clearance, such as PLGA, PEG, polyvinyl acetate (PVA), phospholipids, and so forth.^{119, 158, 159} Except the reduced side effects, the advantages of nanocarriers include not only depositing the encapsulated cargoes in a controlled fashion, but also protecting drug and other bioactive molecule from the interaction with other nontargeting biomolecules, which can definitely improve prodrugs' bioavailability and therapeutic index.^{119, 158, 160} The second category is the nanomedicine itself can serve as anti-inflammatory agent to capture or inhibit ROS, free radicals as well as downregulate other inflammatory mediator, which are elevated within the reactive sites and remain low in the healthy tissues, such as dopamine-melanin nanoparticles, cerium oxide nanoparticles, silver nanoparticles, etc.¹⁶¹⁻¹⁶³

Table 1.5. Nanoplatfroms used in inflammatory diseases

Nanocarrier			Nanoparticles		
Nanoplatfrom	Encapsulated Agent	Ref.	Nanoplatfrom	Mechanism	Ref.

Polymeric nanocarrier	Tanshinone-IIA	164	Polydopamine- melanin nanoparticles	Radical scavenger	162
Nanoemulsion	Aspirin	165	Selenium nanoparticles	Anti- inflammation	166
Polymeric nanocarrier	Curcumin	167	Nanocrystalline silver	Anti- inflammation	168
Hydrotalcite-like compound nanoshell	Diclofenac	169	Hydroxyapatite nanoparticles	Anti- inflammation	170
Nanoemulgel	Curcumin	171	Cerium Oxide nanoparticles	Anti- inflammation	161
Chitosan-alginate nanocarrier	Benzoyl peroxide	172			
Liposome	Prednisolone acetate	173			

Dissertation focus and outline

The next three chapters, I will discuss three different nanomedicines we developed for combination cancer immunotherapy and anti-inflammatory therapy, followed by a chapter 5 to summarize the progress of the current work and suggest future exploration in the new field of nanomedicine. In the first study shown in Chapter 2, we aim to efficiently deliver two therapeutic agents by using one nanoconjugate at an optimized drug ratio to initiate ICD process via PDT, followed by IDO-targeting cancer immunotherapy to achieve synergistic tumor elimination and

future tumor prevention. We loaded IDO inhibitive chemotherapeutic into the core nanocomponent, with multiple potent PS encapsulated nanosatellites. After irradiation, nanoconjugate acted as an effective cancer regimen with complete tumor elimination, and vaccine that successfully prevented second tumor inoculation. The second study in Chapter 3 was published on *Nanoscale*, **2019**, *11*, 11605-11616. We aim to investigate whether nanoparticle itself can serve as anti-oxidative agents for osteoarthritis (OA) therapy. We prepared dopamine melanin (DM) nanoparticle that served as an incredible radical scavenger for reactive oxygen species (ROS) to protect chondrocytes, which diminished inflammatory cytokine release and reduced proteoglycan loss in rodent cartilage with undetectable side effects, suggesting DM nanoparticles are a safe and promising therapeutic for OA. The last study in Chapter 4 was published on *IBRO Neuroscience Reports* **2021**, *10*, 18-30. We engineered nano-based delivery system as an anti-inflammatory therapy for ischemic stroke treatment, which was encapsulated with Tanshinone IIA, anti-inflammatory drug, showed a reduction in SOD activity and inflammatory cytokine release in treated neural stem cells and microglia. Also, ischemic stroke pigs exhibited reduced hemispheric swelling, consequent midline shift and ischemic lesion volumes, indicating Tanshinone IIA nanoparticles could be a novel treatment for ischemic stroke.

CHAPTER 2

NANOCONJUGATES TO ENHANCE PDT-MEDIATED CANCER IMMUNOTHERAPY BY TARGETING THE INDOLEAMINE-2,3-DIOXYGENASE (IDO) PATHWAY¹

¹ Xueyuan Yang, Weizhong Zhang, Wen Jiang, Anil Kumar, Shiyi Zhou, Zhengwei Cao, Shuyue Zhan, Wei Yang, Jin Xie.
Submitted to *Nanoscale Horizons*, 02/16/2021.

Abstract:

Herein we explore combination therapy involving photodynamic therapy (PDT) and immune checkpoint blockade using a composite nanoparticle. Briefly, we separately encapsulate ZnF₁₆Pc, a photosensitizer, and NLG919, an indoleamine 2,3-dioxygenase (IDO) inhibitor, into ferritin nanocages and PLGA nanoparticles; we then conjugate these two nanocompartments to form a satellite/core nanostructure referred to as PPF NPs. When tested in B16F10-tumor bearing C57/BL6 mice, PPF plus photo-irradiation significantly improved tumor suppression and animal survival. The treatment increased tumor infiltration of CD8⁺ T cells, while reducing frequencies of MDSCs and Tregs. Thirty percent of the animals showed complete tumor eradication, and successfully rejected a second tumor inoculation. Overall, our studies introduce a unique nanostructure that allows for co-delivery of photosensitizer and IDO inhibitor with minimal inter-species interference, which is ideal for combination therapy.

Introduction

Photodynamic therapy or PDT has been extensively tested for cancer treatment. During PDT, a large amount of reactive oxygen species such as singlet oxygen are produced, which cause physical damage to cancer cells or tumor vasculature.³ PDT also induces immunogenic cell death (ICD), eliciting an antitumor immunity that benefits long-term tumor management.⁴⁴ However, PDT as a monotherapy is associated with a relatively high recurrence rate. While the reasons are multi-fold, one factor is that PDT may cause excessive inflammation that induces immunosuppressive mechanisms,^{44, 55, 174} leading to cancer cell immune escape and repopulation. Immune checkpoint inhibitors, which can selectively block related regulatory axes, can be used in combination with PDT to improve therapy outcomes.⁷⁷⁻⁷⁹ For instance, several groups, including

us, have demonstrated that PDT combined with anti-PD-1/PD-L1/CTLA4 antibodies augments immune response,^{175, 176} facilitating suppression of both primary and distant tumors.¹⁵⁵

Indoleamine 2,3-dioxygenase (IDO) is another immune checkpoint frequently implicated in tumor immunosuppression.⁴⁴ IDO is a monomeric, heme-containing enzyme that metabolizes tryptophan (Trp) to kynurenine (Kyn). IDO is frequently upregulated in both cancer cells and host antigen-presenting cells (APCs).⁸⁵ IDO overexpression leads to the depletion of Trp, which is essential to the survival and functions of effector T cells, causing their G1 cycle arrest and apoptosis.^{85, 94} Meanwhile, the metabolite Kyn can promote the differentiation and activation of regulatory T cells (Tregs);¹⁰¹ this in turn promotes the recruitment of myeloid-derived suppressor cells (MDSCs), leading to a tolerogenic tumor microenvironment (TME).^{85, 100, 101} Multiple molecule IDO inhibitors have been developed and tested in pre-clinical and clinical studies.¹⁷⁷ Combining PDT with IDO inhibition has only very recently been tested and shown promising results.⁴⁴

Herein, we report a composite, core/satellite nanoparticle that allows for co-delivery of photosensitizer and IDO inhibitor for combination PDT and immune checkpoint blockade (ICB) therapy. Photosensitizers and IDO inhibitors belong to two categories of therapeutics that have different physiochemical and pharmacokinetic properties. While it is possible to load both types of therapeutics onto one nanoplatform, the drugs may interfere with each other and negatively affect loading and release. To solve the issue, we construct a composite nanostructure where zinc hexadecafluoro-phthalocyanine (ZnF₁₆Pc) and NLG919 are encapsulated into separate nanocompartments. More specifically, ZnF₁₆Pc, a near-infrared photosensitizer (ex: ~670 nm) is encapsulated into ferritin (FRT) protein cage, whereas NLG919, a potent enzymatic inhibitor of IDO, is encapsulated into poly(lactide-co-glycolic)-*block*-poly(ethylene glycol) (PEG-PLGA)

nanoparticles. The two particles are covalently conjugated to form a core/satellite nanostructure (Figure 1a).¹⁷⁷ While ZnF₁₆Pc is minimally released from ferritin thus enabling steadfast production of reactive oxygen species (ROS) under photo-irradiation,^{30, 126} NLG919 is released from PEG-PLGA nanoparticles in a controlled fashion to allow for sustained inhibition of IDO post PDT. We administered the resulting, PEG-PLGA and FRT composite nanoparticles (hereafter referred to as PPF NPs), into B16F10-tumor-bearing mice to examine their tumor suppression efficacy and antitumor immunity.

Results and Discussion

Heavy-chain ferritin was prepared and purified according to our published protocol.¹⁷⁸ ZnF₁₆Pc was encapsulated into ferritin through a pH-mediated disassembly-and-reassembly approach, and purified on a desalting column to remove unbound ZnF₁₆Pc.^{30, 31} The resulting, ZnF₁₆Pc encapsulated ferritin or ZnF₁₆Pc@FRT, contains 40 wt% ZnF₁₆Pc and has a diameter of ~12 nm. Meanwhile, NLG919 was encapsulated into polymeric nanoparticles made of PLGA-*b*-PEG-COOH (Mn: 7,000 Da for PLGA and 1000 Da for PEG) through nanoprecipitation. This yielded NLG919-encapsulated PEG-PLGA nanoparticles (NLG919@PLGA NPs) with a loading rate of 6.63 wt% (**Figure S2.1&2.2**).

To construct PPF core/satellite nanoparticles, the surface carboxyl groups of NLG919@PLGA NPs were activated by ED C/NHS chemistry; the resulting nanoparticles were mixed with ZnF₁₆Pc@FRT to form a covalent linkage. The ratio between the two nanocompartments were adjusted so that in the final conjugate (i.e. PPF NPs), the NLG919 to ZnF₁₆Pc ratio was ~7:1; this ratio was chosen based on the effective doses of the two therapeutics according to previous studies (Supporting Information).^{30, 113} The successful coupling can be

visualized under transmission electron microscopy (TEM, **Figure 2.1b**). Dynamic light scattering (DLS) found an increased hydrodynamic diameter from 112.9 ± 0.7 to 144.0 ± 1.3 nm (**Figure 2.1c**). This was accompanied by a surface charge increase from -33.30 ± 1.03 to -20.23 ± 1.72 mV (**Figure 2.1d**), also confirming the conjugation.

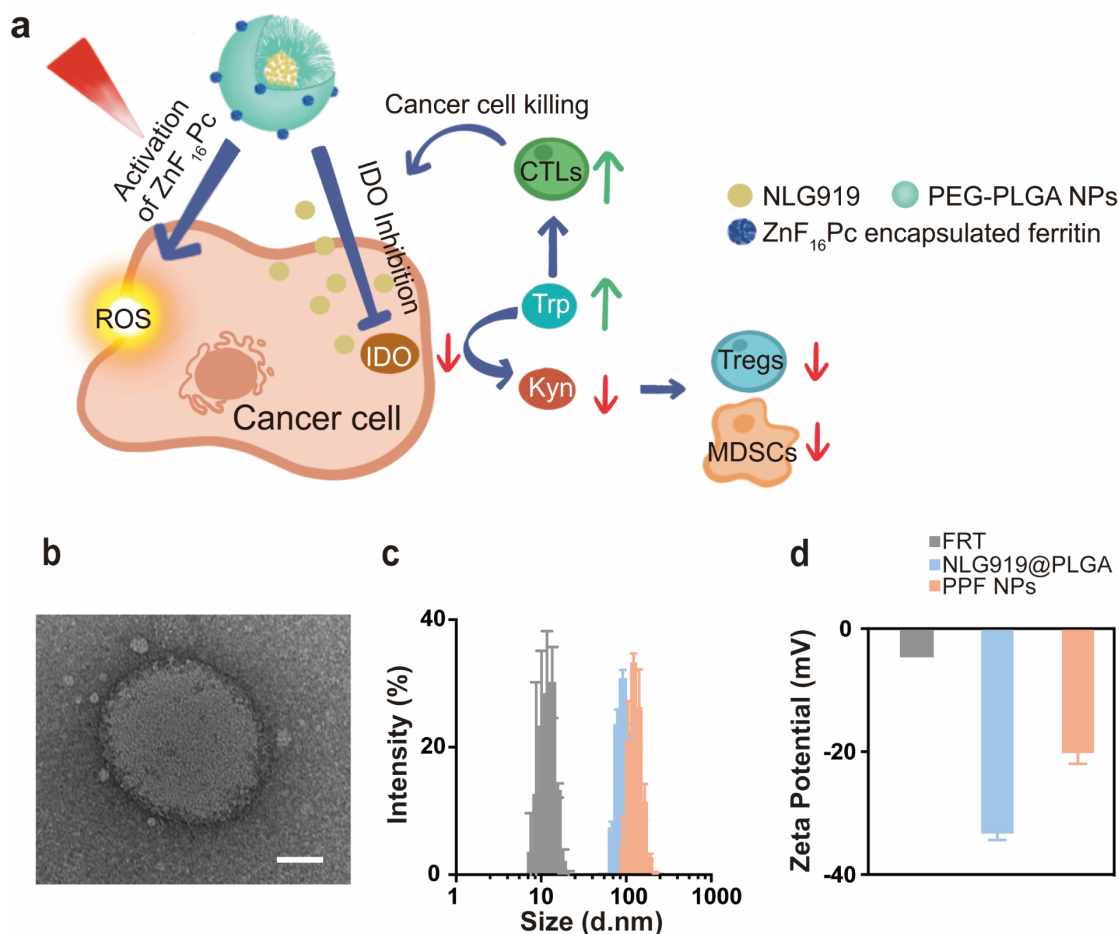


Figure 2.1. Preparation and characterizations of PPF NPs. a) Schematic illustration showing the mechanism behind PPF NPs enabled immunotherapy. The PPF conjugate contains two nanocompartments, which are FRT and PLGA NPs. These two compartments are separately encapsulated with ZnF₁₆Pc and NLG919, and covalently linked. Under photo-irradiation, ZnF₁₆Pc is activated, leading to cancer cell death and release of tumor associated antigens. Meanwhile,

NLG919 causes the suppression of IDO and restored the Trp/Kyn balance; this results in reduced tumor infiltration of Tregs and MDSCs and increased cytotoxic T cell activity, leading to enhanced antitumor immunity. b) TEM images of PPF NPs. Scale bar, 50 nm. c) Hydrodynamic sizes of FRT, NLG919@PLGA and PPF NPs, measured by DLS. d) Zeta potential of FRT, NLG919@PLGA and PPF NPs.

We also studied drug release using UV-vis spectrophotometry. The release of NLG919 from PPF NPs was relatively slow at pH 7.4 (77.5% at 24 h, **Figure 2.2a**), and accelerated under acidic conditions (98.2% at 24 h, **Figure 2.2a**). Meanwhile, ZnF₁₆Pc release was minimal at both neutral and acidic pH (**Figure 2.2b**), which is consistent with our previous observations.³¹ Notably, photo-irradiation did not significantly accelerate the release of either drug molecules (**Figure 2.2a&b**).

We then evaluated the cytotoxicity of PPF NPs in B16F10 cells, which are a murine melanoma cell line. Briefly, B16F10 cells were incubated with PPF NPs (25 µg/mL, ZnF₁₆Pc concentration) in the dark and irradiated at 4 h (671 nm, 0.1 W/cm², 200 s). PPF NPs in the absence of radiation showed low toxicity (**Figure S2.3**). Under radiation, there was a significant viability drop, which is attributed to PDT. We also evaluated the IDO inhibition efficacy of PPF NPs. This was examined in HeLa cells, which express a high level of IDO and are commonly used for *in vitro* IDO inhibition assessment.^{113, 179, 180} Briefly, HeLa cells were treated with IFN-γ to induce IDO expression, followed by incubation with PPF NPs for 48 hrs; the amounts of Kyn in the culturing medium were quantified using a colorimetric assay (**Figure 2.2c**).¹¹³ PPF NPs showed efficient and concentration-dependent inhibition of Kyn production. The EC₅₀ is 1.25 µg/mL, which is comparable to free NLG919 (**Figure 2.2c**).

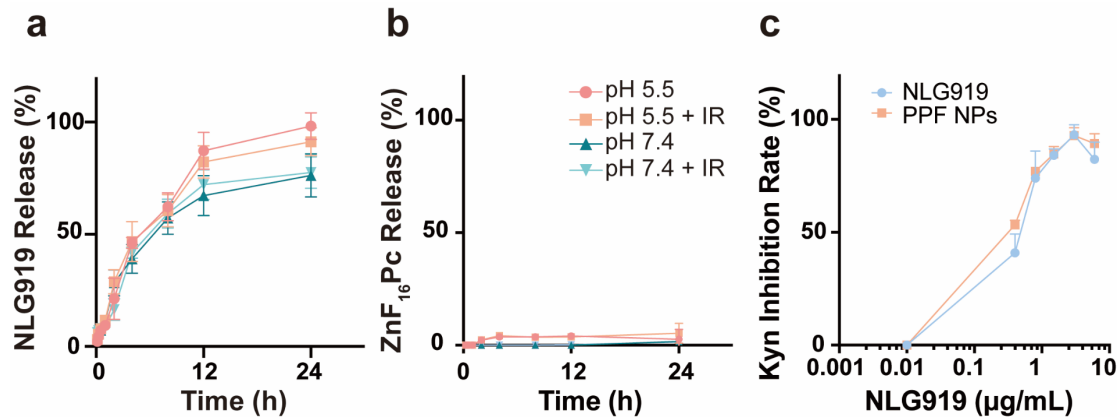


Figure 2.2. Drug release and IDO inhibition efficiency. a,b) Drug release kinetics, tested with PPF NPs in buffer solutions with pH 5.5 and 7.4 in the presence and absence of photo-irradiation (IR). a) NLG919 release profiles. b) ZnF₁₆Pc release profiles. c) IDO inhibition, examined by measuring Kyn released from HeLa cells. HeLa cells were first treated with IFN- γ along with either free NLG919 or PPF NPs. Kyn in the supernatant was quantified 48 h later, and compared to PBS-treated cells. The experiments were conducted in triplicate. Values are presented as means \pm SD.

We next evaluated the therapeutic effects of PPF NPs *in vivo* in B16F10 tumor bearing C57BL/6 mice. We intratumorally (i.t.) injected PPF NPs (2.5 mg/kg NLG919, equivalent to 0.375 mg/kg ZnF₁₆Pc) into the animals (n=10). This was followed by photo-irradiation with a 671-nm laser (0.3 W/cm², 15 min) applied to tumors at 4 h (Day 0, the treatment group was denoted as PPF+IR). Two more treatments were applied on Day 3 and 6. For comparison, NLG919@PLGA NPs in the absence of irradiation (NLG919@PLGA, n=10) and ZnF₁₆Pc@FRT plus irradiation (ZnF₁₆Pc@FRT+IR, n=10) were also tested. PBS only in the absence of irradiation was tested as a control (PBS, n = 8).

ZnF₁₆Pc@FRT+IR caused a modest tumor suppression, inhibiting tumor growth by 51.27% relative to the PBS control group on Day 12 (**Figure 2.3a**). However, this was followed by a rapid tumor rebound (**Figure 2.3a&c**), with 40% of the animals reaching a humane endpoint point by Day 15. NLG919@PLGA failed to suppress tumor growth but rather promoted it in the short-term, although the difference was insignificant between the NLG919@PLGA and PBS groups ($p = 0.81$, **Figure 2.3a&c**). All animals in the NLG919@PLGA group either died or had to be euthanized by Day 12. As a comparison, PPF+IR resulted in remarkable tumor suppression (84.19% on Day 12, **Figure 2.3a&c**). Thirty percent of the mice in the PPF+IR group showed complete tumor eradication and remained alive after 6 months. For dead or euthanized animals, we harvested their tumors and major organ tissues for histology analysis. H&E and Ki-67 staining confirmed efficient cancer cell killing and tumor growth suppression in the PPF+IR group (**Figure 2.3d**).

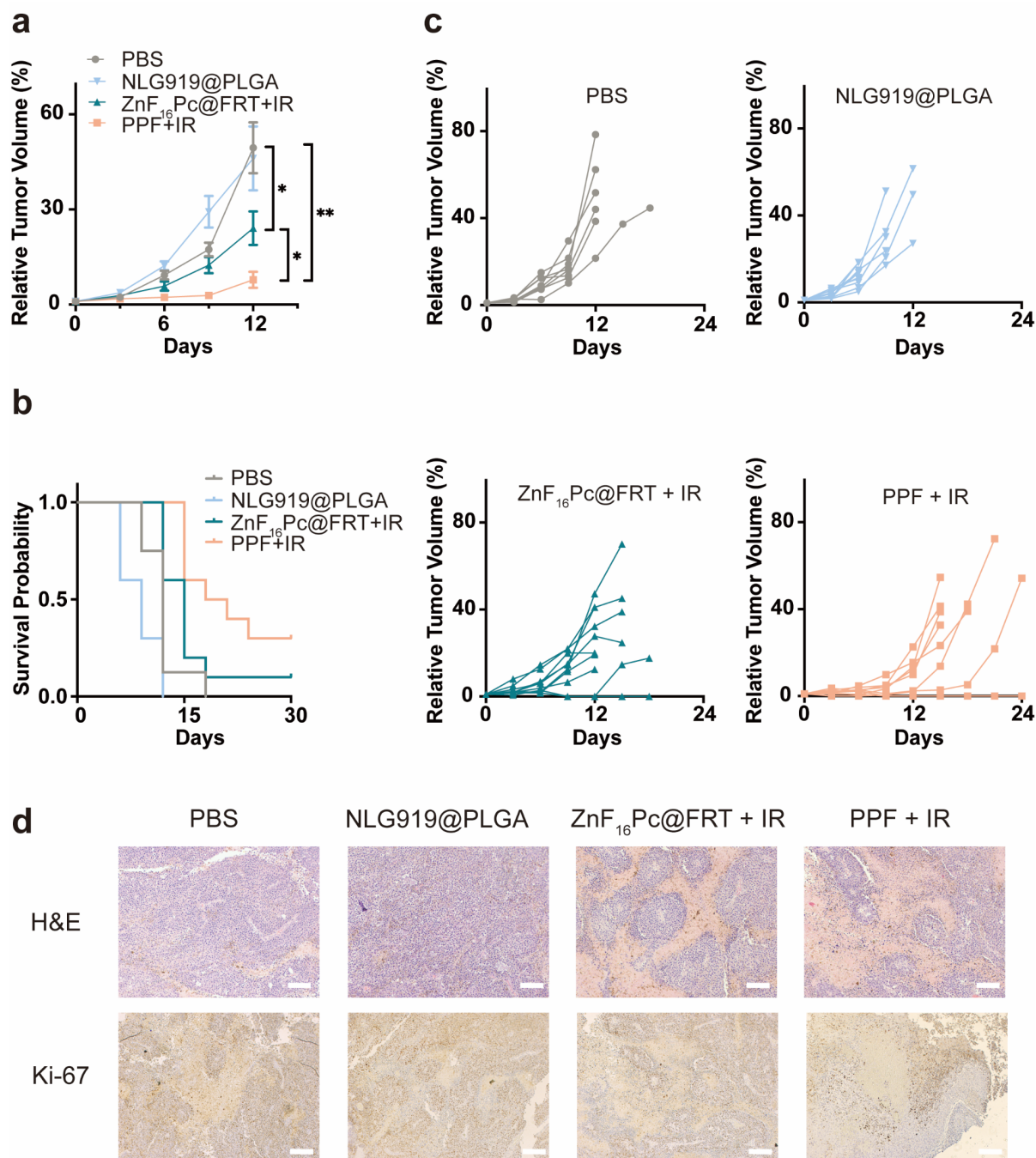


Figure 2.3. *In vivo* treatment efficacy, tested in C57BL/6 mice bearing B16F10 tumors. The animals were i.t. injected with PPF NPs and irradiated with a 671-nm laser at 4 h (PPF+IR). A total of three doses of treatment were given two days apart. PBS, NLG919@PLGA NPs in the absence of irradiation (NLG919@PLGA), and ZnF₁₆Pc@FRT plus irradiation (ZnF₁₆Pc@FRT+IR) were tested for comparison (n = 8-10). a) Relative tumor volume change.

Values are presented as means \pm SEM. * $p < 0.05$, ** $p < 0.01$. b) Animal survival. c) Relative volume change for individual tumors from different treatment groups. d) H&E and Ki-67 staining with tumor samples taken from all treatment groups. Scale bars, 100 μ m.

For animals showing complete tumor elimination in the PPF+IR group, a re-challenge study was performed to assess whether the treatment promoted anticancer immunity. Briefly, we injected live B16F10 cells into the opposite flank of these animals on Day 69 and monitored the tumor growth. All of the mice successfully rejected the second inoculation, and remained healthy through the remainder of the experiment (**Figure S2.4&2.5**). As a comparison, the only surviving animal from the ZnF₁₆Pc@FRT+IR group succumbed to the second inoculation on Day 84. We euthanized animals from the PPF+IR group on Day 159, and analyzed memory T cells by flow cytometry. We found that both central and effector memory T cell populations were significantly increased relative to naïve mice (**Figure S2.6a-b**). These results suggested that animals treated with PPF+IR developed a strong antitumor immunity.

To better understand treatment-induced immune responses, in a separate study, we treated animals with the same regimens (PPF+IR, PP, ZnF₁₆Pc@FRT+IR, and PBS, single dose) and euthanized them one day after the treatment. We collected blood samples and analyzed serum concentrations of Trp and Kyn by LC-MS. We found that Trp/Kyn ratio was slightly reduced in the ZnF₁₆Pc@FRT+IR group relative to the PBS control (Figure 2.4a, $p = 0.28$), which is attributable to PDT-induced IDO upregulation. In both NLG919@PLGA and PPF+IR groups, Trp/Kyn ratios were significantly increased (**Figure 2.4a**), which is owing to NLG919-based IDO inhibition.

We then repeated the therapy study but euthanized animals 7 days after the third treatment and collected tumor and spleen tissues to examine lymphocyte profiles. Compared to the PBS and ZnF₁₆Pc@FRT groups, there was a significant decrease of MDSCs population in tumors treated with NLG919@PLGA (**Figure 2.4b**). PPF+IR led to an even greater reduction in the MDSCs population. More remarkable reduction was observed with Tregs, whose abundance was decreased by 74.03% and 68.15%, respectively, in the NLG919@PLGA and ZnF₁₆Pc@FRT+IR groups, and by 95.97% in the PPF+IR group (**Figure 2.4b**). Similar trends were observed in spleen tissue samples (**Figure 2.4c**). Meanwhile, PPF+IR led to a significant increase in the dendritic cell and cytotoxic T cell populations in both tumor and spleen samples (**Figures 2.4b-c**). CD8/Treg ratio was dramatically increased from 54.52% in the ZnF₁₆Pc@FRT+IR group to 848.43% in the PPF+IR group in tumor (**Figure 2.4d**). Overall, these studies confirm that combination PDT and ICB with PPF NPs plus photo-irradiation induced a strong anticancer immunity.

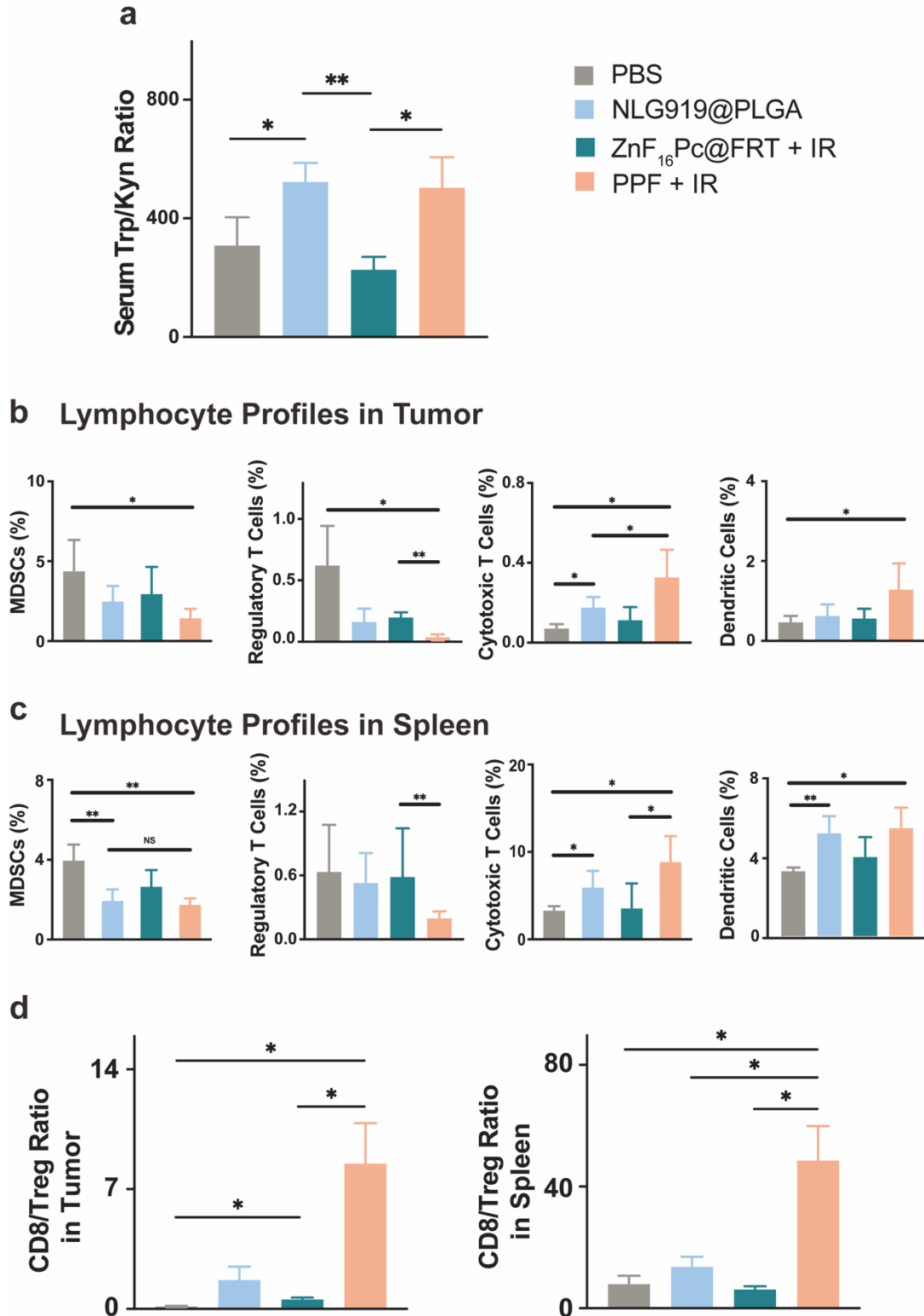


Figure 2.4. Antitumor immune response elicited by the combination therapy. a) Serum Trp/Kyn ratios, measured by LC/MS. Blood samples were taken from animals one day after the treatments.

b,c) Lymphocyte frequencies in tumor (c) and spleen (d). Tissues were harvested 7 days after the third treatment. d) CD8/Treg ratios in tumor (left) and spleen (right) tissues. Values are presented as means \pm SD. $*p < 0.05$, $**p < 0.01$.

Meanwhile, the treatment was well tolerated by the animals. There were no signs of acute toxicity after PDT. No body weight loss was observed throughout the studies (**Figure 2.5a**). We also harvested tissues from normal organs, such as the heart, kidney, liver, lung, and spleen, and H&E staining found no signs of toxicity in the PPF+IR group (**Figure 2.5b**).

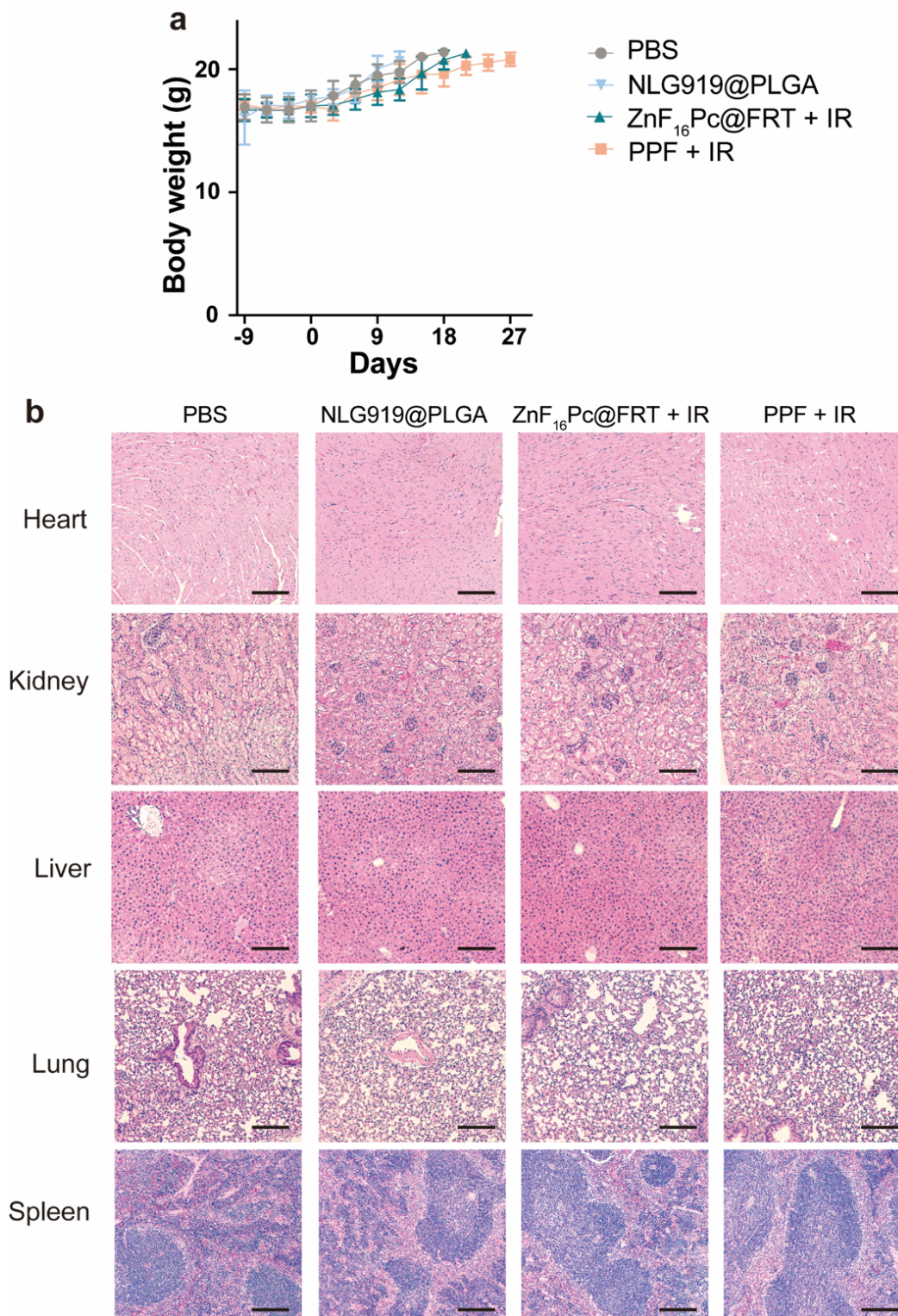


Figure 2.5. Potential side effects caused by the combination treatment. a) Body weight curves. No significant body weight loss was observed throughout the study. b) H&E staining of normal tissues,

including the heart, kidney, liver, lung, and spleen. No signs of toxicity were detected. Scale bars, 100 μm .

Conclusion

PDT can cause ICD, promoting recruitment and activation of innate immune cells such as dendritic cells.¹⁵⁵ This in turn may enhance antigen cross-presentation to T cells, stimulating specific antitumor immune responses. However, tumors may hijack immunoregulatory mechanisms to subvert PDT-induced immunity. Taking the current study for instance, ZnF₁₆Pc@FRT+IR only caused a modest benefit in tumor suppression and animal survival, and failed to induce an abscopal effect. As a comparison, PPF NPs enable combination PDT and ICB therapy that significantly improves tumor management, resulting in complete tumor eradication in 30% of the treated animals and protecting them from a subsequent live cell challenge. Our unique composite nanoparticle is considered an important factor for effective treatment, for it enables efficient PDT and controlled release of IDO inhibitors. In current studies, nanoparticles were topically applied, which is suitable for melanoma therapy. It is postulated that this strategy can be used to treat stage III and recurrent melanoma, eliciting an antitumor immunity that not only eradicates local or residual cancer cells after surgery but also prevents metastasis. Melanoma is relatively resistant to PDT due to the absorbance and anti-oxidant effects of melanin.¹⁸¹ It is possible that switching to a photosensitizer with even longer excitation wavelength may improve the treatment. PPF nanoparticles may be systemically administered for treatment of other cancer types such as prostate and head and neck cancer. PPF treatment may also synergize with anti-PD-1/PD-L1 antibodies that block other immunoregulatory pathways. These possibilities will be explored in future studies.

Materials and Methods:

PLGA-COOH (MW: 7000, Lactel; cat#: B6013-1G); *N*-Hydroxysuccinimide (NHS) (Sigma Aldrich; cat#: 56480-25G); *N*-Ethyl-3-(3-dimethylaminopropyl)carbodiimide (EDC) (Sigma Aldrich; cat#: E7750); Dichloromethane (DCM) (Sigma Aldrich; cat#: 270997); Methanol (Fisher Scientific; cat#: A456-4); Diethyl Ether (Sigma Aldrich; cat#: 91238); NH₂-PEG-COOH (MW: 1000, Biochempeg Scientific; cat#:HE005017-1K); *N,N*-Diisopropylethylamine (DIEA) (Alfa Aesar; cat#:A11801); Acetonitrile (Sigma Aldrich; cat#:271004-1L); NLG919 (Advanced Chemblocks; cat#:L14096); Hydrochloric Acid (HCl) (J.T.Baker; cat#:9535-03); Sodium Hydroxide (NaOH) (Fisher Scientific; cat#:S318-3); zinc hexadecafluoro-phthalocyanine (ZnF₁₆Pc) (Sigma Aldrich; cat#:444529); Dimethyl Sulfoxide (DMSO) (Sigma Aldrich; cat#: 276855); Uranyl Acetate 2% solution (Fisher Scientific, cat#:NC1085517); Illustra NAP-10 columns (GE Healthcare; cat#: 17-0854-02); Dulbecco's Modified Eagle's Medium (DMEM) (ATCC; cat#:30-2002); Eagle's Minimum Essential Medium (EMEM) (ATCC; cat#:30-2003); Fetal Bovine Serum (ATCC; cat#:30-2020); Penicillin-streptomycin (Sigma Aldrich; cat#: P0781-100mL); 3-(4,5-dimethylthiazol-2-yl)-2,5-diphenyl Tetrazolium Bromide (MTT) (Sigma Aldrich; cat#:M2128); Human IFN- γ (R&D Systems; 285-IF); Trichloroacetic Acid (Fisher Scientific; cat#: ICN15259291); p-dimethylamino-benzaldehyde (Sigma Aldrich; cat#: 109762); Glacial Acetic Acid (J.T.Baker; cat#:9508-00).

PLGA-b-PEG-COOH Synthesis:

PLGA-PEG-COOH polymer was synthesized using EDC/NHS chemistry. Briefly, 500 mg PLGA-COOH (0.071 mmol) and 109 mg EDC (0.7 mmol) were dissolved in 7 mL DCM, under magnetic stirring at room temperature for 10 min. Then, 160 mg NHS (1.4 mmol) was dissolved

in 7 mL DCM, followed by dropwise addition into the above solution. The reaction was conducted overnight at room temperature. PLGA-NHS was washed with cold 1:1 methanol/diethyl ether mixture for three times, collected by centrifugation, and lyophilized. Then, 200 mg PLGA-NHS (0.028 mmol) was dissolved in 5 mL DCM under magnetic stirring at room temperature for 10 min. 30 mg NH₂-PEG-COOH (0.03 mmol) and 60 μ L DIEA (0.28 mmol) were dissolved in 2 mL DCM, and dropwise added into the PLGA-NHS solution. The reaction was conducted overnight. The conjugated PLGA-*b*-PEG-COOH polymer was washed with cold, 1:1 v/v methanol/diethyl ether mixture for three times, collected by centrifugation, and lyophilized. The product was stored at -20 °C. Chemical structure was confirmed by ¹H-NMR on a Varian Mercury Plus 400 system.

NLG919@PLGA Nanoparticle Synthesis:

NLG919@PLGA NPs were synthesized through a nanoprecipitation method. Briefly, PLGA-*b*-PEG-COOH and NLG919 were first dissolved in acetonitrile; the final concentrations were 5 mg/mL for PLGA-*b*-PEG-COOH and 1.5 mg/mL for NLG919. The mixture was dropwise added into sterilized nanopure water with constant stirring for 2 h in fume hood. The resulting NLG919@PLGA NPs were collected on an amicon ultracentrifugation unit (MWCO 100 kDa) and washed 3-4 times with sterilized nanopure water. Finally, the purified NLG919@PLGA NPs were resuspended in sterilized nanopure water and kept at 4 °C.

Preparation of ZnF₁₆Pc@FRT:

Protocols for ferritin (FRT) expression and purification were published before.³⁰ ZnF₁₆Pc loading was achieved by following a published protocol with modification. Briefly, FRT was dispersed in PBS (pH 7.4), and the solution pH was reduced to 2.0 by adding 0.2 M HCl. ZnF₁₆Pc (5 mg/mL in DMSO) was added into the above solution to reach a final FRT/ZnF₁₆Pc w/w ratio

of 5:1. After gently shaking at room temperature for 30 min, the pH of the mixture was slowly adjusted back to 7.4 by adding 1 M NaOH. NAP-10 column was used to remove unloaded ZnF₁₆Pc.

Preparation of PPF NPs:

Briefly, NLG919@PLGA NPs (10 mg/ml) were resuspended in 3 mL sterilized nanopure water with constant stirring. Then, 720 μ L EDC (10 mg/mL) was dropwise added, followed by the addition of 440 μ L NHS (10 mg/mL), with constant stirring for 2 hours under room temperature. The conjugates were collected by centrifugation for 3 times at 15 °C. The purified nanoparticles were suspended in 5 mL PBS (pH 7.4) with constant stirring at 4 °C in the dark, followed by the addition of ZnF₁₆Pc@FRT (0.25 mg, based on FRT weight) into the solution. The mixture was stirred for 4 hours. Finally, the conjugated nanoparticles were collected and purified by PBS (pH 7.4) for three times. PPF NPs were stored at 4 °C protected from light.

The ZnF₁₆Pc to NLG919 ratio was adjusted to be ~ 1:7, based on previous research and experience. ZnF₁₆Pc@FRT at a dose of 1.5 mg/kg of ZnF₁₆Pc is commonly tested in tumor bearing mice with i.v. administration. According to our experience, about 10% of ZnF₁₆Pc@FRT could accumulate in the tumor site. NLG919 at a dose of 25 mg/kg on mice with i.v. injection is normally used in cancer immunotherapy.¹¹³ Polymeric nanoparticles are reported to accumulate in tumors at a rate of 3-5%. Based on our computation, a ZnF₁₆Pc-to-NLG919 ratio of 1:7 is reasonable for combination therapy.

Nanoparticles Characterizations:

For TEM analysis, a drop of diluted sample solution was deposited onto a TEM grid, followed by staining with 2% uranyl acetate. TEM images were taken on a JEOL JEM-1011 Transmission Electron Microscope operating at an accelerating voltage of 80 KV. Hydrodynamic size and zeta potential of nanoparticles were analyzed on a Malvern Zetasizer Nano ZS system.

Drug Release:

For drug release studies, 100 μL nanoparticle solution was loaded onto a dialysis unit, with or without irradiation (671 nm, 0.1 W/cm^2 for 200 s). The unit was floated on top of a 1.1-mL buffer solution (pH 5.5 or 7.4). The system was positioned on an Eppendorf shaker set at 37 $^{\circ}\text{C}$. At each time point (0.5, 1, 2, 4, 8, 12, 24, 36 and 48 h), 100 μL external solution was transferred into a 96-well plate. The drug contents were assessed by measuring the relevant absorbance (NLG919: 263 nm, ZnF_{16}Pc : 700 nm) and comparing to pre-established standard curves.

Cell Culturing:

B16F10 and HeLa cells were obtained from American Type Culture Collection (ATCC) and cultured in DMEM or EMEM medium supplemented with 10% fetal bovine serum and 1% penicillin-streptomycin. The cells were incubated humidly at 37 $^{\circ}\text{C}$ with 5% CO_2 .

Cytotoxicity Assays:

B16F10 cells were seeded onto a 96-well plate at 8000 cells per well density and allowed to grow overnight. Nanoparticles of varied concentrations were added to the incubation medium. After 4 hours, the cells were exposed to a 671-nm laser (0.1 W/cm^2 for 200 s). Cells not exposed to photo-irradiation were tested for comparison. After another 12 hours, cell viability was measured by MTT assay.

IDO Activity:

Briefly, HeLa cells were seeded onto a 96-well plate at a density of 8000 cells per well and allowed to grow overnight. Recombinant human IFN- γ was added to each well to reach a final concentration of 50 ng/mL. Meantime, a gradient of NLG919@PLGA NPs or PPF NPs (NLG919 concentration 0, 0.4, 0.8, 1.5, 3, 6 $\mu\text{g}/\text{mL}$) were added to the incubation medium. After 48 hours, 150 μL of the supernatants per well was transferred to a separate 96-well plate. 75 μL 30%

trichloroacetic acid was added into each well and incubated with cells at 50 °C for 30 min, converting N-formylkynurenine to kynurenine. The supernatant was transferred to a new 96-well plate, mixed with equal volume of Ehrlich reagent (2% p-dimethylamino-benzaldehyde w/v in glacial acetic acid), and incubated for 10 min at room temperature. Reaction product was quantified by measuring 490-nm absorbance using a plate reader.

Animal Model:

C57BL/6 mice were purchased from Envigo laboratories. The animal model was established by subcutaneously injecting 2×10^5 B16F10 cells into the right hind limb of each mouse. All of the experimental procedures were conducted following a protocol approved by the University of Georgia Institutional Animal Care and Use Committee.

Therapy Studies:

C57BL/6 mice bearing B16F10 tumors were randomly divided into four groups (n=8-10): (1) PBS, no irradiation; (2) NLG919@PLGA NPs (NLG919 2.5 mg/kg), no irradiation; (3) ZnF₁₆Pc@FRT (ZnF₁₆Pc 0.375 mg/kg), with irradiation; (4) PPF NPs (NLG919 2.5 mg/kg, ZnF₁₆Pc 0.375 mg/kg), with irradiation. All mice received i.t. injection every 3 days for 3 times. For the ZnF₁₆Pc@FRT+IR and PPF+IR groups, tumors received photo-irradiation 4 hours after the injection (671 nm, 0.3 W/cm² for 15 min). Tumor size and body weight were monitored every 3 days. Tumor volume was computed using formula: tumor volume = length x (width)²/2. After therapy, major organs as well as tumors were collected and sectioned into 8-μm slices for H&E and Ki-67 staining. For re-challenge studies, each of the surviving animals was subcutaneously injected with 1×10^5 B16F10 cells to the left hind limb. Tumor size and body weight of were monitored every three days.

Serum Tryptophan and Kynurenine Analysis:

Trp/Kyn ratios in serum samples were examined by LC/MS on a Bruker Daltonics Impact II system. C57BL/6 mice bearing B16F10 tumor at $\sim 50 \text{ mm}^3$ were treated with single-dose of PBS, NLG919@PLGA NPs, ZnF₁₆Pc@FRT+IR, or PPF+IR (NLG919 2.5 mg/kg, ZnF₁₆Pc 0.375 mg/kg). One day after the treatment, the plasma samples were collected and mixed with methanol (plasma: methanol, 1:2.5, v/v) and centrifuged at 13,500 rpm for 15 min. Supernatants were collected and purified with TopTip for LC-MS quantification of kynurenine and tryptophan.

Lymphocyte Profiling Studies:

Seven days after the third treatment, animals were euthanized; spleen and tumors were harvested, and immune cell populations in the tissues was examined by flow cytometry. Briefly, single-cell suspensions from tissue samples were filtered and red blood cells were lysed. For extracellular staining, cells were incubated with the indicated combinations of antibodies (e.g. anti-CD11c, -Gr-1, -CD3, -CD8 α , -CD4, and -CD45). For intracellular staining, cells were fixed and permeabilized immediately after cell surface staining according to manufacturer's protocol (eBioscience). Antibodies (e.g. anti-Foxp3) were added into the permeabilization buffer and incubated with cells. Animals surviving from re-challenge studies were euthanized after 30 days, and spleen tissues were harvested for analysis of memory T cell populations. Immune cell populations were examined on a Beckman Coulter CytoFLEX system. Data analyzed was performed using FlowJo software.

Statistical Analysis

Comparison of multiple assays was performed using a one-way ANOVA test. Comparisons of only two groups was performed using a paired *t*-test. Significance was set at $p < 0.05$. All experiments were performed with at least three replicates unless specified otherwise. All the data is represented as mean \pm S.D.

CHAPTER 3

DOPAMINE-MELANIN NANOPARTICLES SCAVENGE REACTIVE OXYGEN AND
NITROGEN SPECIES AND ACTIVATE AUTOPHAGY FOR OSTEOARTHRITIS
THERAPY²

² Xueyuan Yang[†], Gang Zhong[†], Xianfang Jiang[†], Anil Kumar, Huiping Long, Jin Xie*, Li Zheng*, Jinmin Zhao († Equal contribution) *Nanoscale*, 2019,11, 11605-11616.
Reprinted here with permission of the publisher.

Abstract

Anti-oxidative agents hold great potential in osteoarthritis (OA) therapy. However, most radical scavengers have poor biocompatibility and potential cytotoxicity, which limit their applications. Herein we explore dopamine melanin (DM) nanoparticles as a novel scavenger of reactive oxygen species (ROS) and reactive nitrogen species (RNS). DM nanoparticles show low cytotoxicity and a strong ability to sequester a broad range of ROS and RNS, including superoxides, hydroxyl radicals, and peroxynitrite. This translates to excellent anti-inflammatory and chondro-protective effects by inhibiting intracellular ROS and RNS and promoting antioxidant enzyme activities. With an average diameter of 112.5 nm, DM nanoparticles can be intra-articularly (i.a.) injected into an affected joint and retained at the injection site. When tested in vivo in rodent OA models, DM nanoparticles showed diminished inflammatory cytokine release and reduced proteoglycan loss, which in turn slowed down cartilage degradation. Mechanistic studies suggest that DM nanoparticles also enhance autophagy that benefits OA control. In summary, our study suggests DM nanoparticles as a safe and promising therapeutic for OA.

Introduction

Osteoarthritis (OA) is a major cause of chronic disability and it affects more than 400 million people worldwide. OA is characterized by the gradual progression of chronic inflammation and cartilage degeneration, leading to stubborn joint pain and joint deformity.¹⁸² Current treatments, including analgesics, non-steroidal anti-inflammatory drugs (NSAIDs), and intra-articular injection of hyaluronic acid or corticosteroid ¹⁸³, aim to ease the symptoms rather than altering the course of disease progression. There is an urgent need for new and safe options for OA.

Recent studies reveal that ROS and RNS play an essential role in OA development and progression¹⁸⁴. ROS and RNS are produced mainly by NADPH oxidase and iNOS, and remain at low levels in normal articular chondrocytes. In OA patients, the antioxidant mechanisms, including superoxide dismutase (SOD), catalase (CAT), and glutathione peroxidase (GPX), are deregulated and insufficient to detoxify ROS and RNS¹⁸⁵⁻¹⁸⁷. This leads to elevated oxidative stress that induces DNA, lipid, and protein damage, as well as cytotoxicity. Reagents that can suppress ROS and RNS in the chondrocytes are therefore promising OA therapeutics. Previously, anti-oxidants like melatonin and N-acetylcysteine (NAC)^{188, 189} have been tested but these small molecules show short retention in the joint. More recently, nanozymes and metal nanomaterials such as PEGylated bilirubin nanoparticles¹⁹⁰, sialic acid-modified selenium nanoparticles¹⁹¹, and TEMPO-conjugated gold nanoparticles¹⁹² have been explored for OA therapy. But the poor biocompatibility and/or biodegradability have limited their applications.

Herein we investigate melanin nanoparticles as a novel type of radical scavenger for OA therapy. Natural melanin is known to protect the skin from ultraviolet (UV) irradiation. This is in large part attributed to its surface quinone residues that can efficiently scavenge radicals. Artificial melanin nanospheres have been prepared by polymerization of dopamine¹⁹³. The Shi group recently investigated the anti-oxidant mechanisms of these melanin nanoparticles, showing that materials can scavenge a broad range of radicals¹⁹⁴. Rageh et al. demonstrated that melanin nanoparticles can protect mice from DNA damage induced by γ -radiation and effectively restore hematopoietic tissues¹⁹⁵. To the best of our knowledge, however, there has been no attempt on exploiting melanin nanoparticles for OA treatment. Unlike small molecule scavengers, melanin nanospheres are large in size (~110 nm) and thereby affording much longer retention in the joint, which is beneficial for sustained ROS/RNS suppression and OA management. We hypothesize

that i.a. injected melanin nanospheres can efficiently suppress cartilage RNS and ROS levels, leading chondrocyte protection and OA suppression. Specifically, we first assessed whether DM nanoparticles can suppress ROS and RNS in IL-1 β induced rat chondrocytes, and tested their efficacy in vivo in a rat OA model. The underlying mechanism of action was also investigated.

Results

DM nanoparticles synthesis and characterizations

DM nanoparticles were synthesized following a published protocol with minor modifications¹⁹³. Briefly, we dissolved dopamine hydrochloride in an ethanol/water mixed solution and added into the solution ammonium hydroxide. After 24 h reaction in the open air, the nanoparticle products were collected by centrifugation and purified with water. Scanning emission microscopy (SEM) and transmission emission microscopy (TEM) showed that the products were uniform nanospheres, with an average diameter of 112.5 nm (**Figure 3.1a, and b**). Dynamic light scattering (DLS) found that the hydrodynamic size of the nanoparticles was ~230 nm (**Figure 3.1c**). Zeta potential analysis showed that the surface of the nanoparticles was negatively charged (-13.5 mV, **Figure 3.1d**). This is attributed to the multiple catechol groups on the nanoparticle surface, which was confirmed by FR-IR (**Figure. S3.1a**). No benzene ring ¹H atom was detected in DM nanoparticles by ¹H NMR (**Figure. S3.1b**), suggesting successful polymerization.

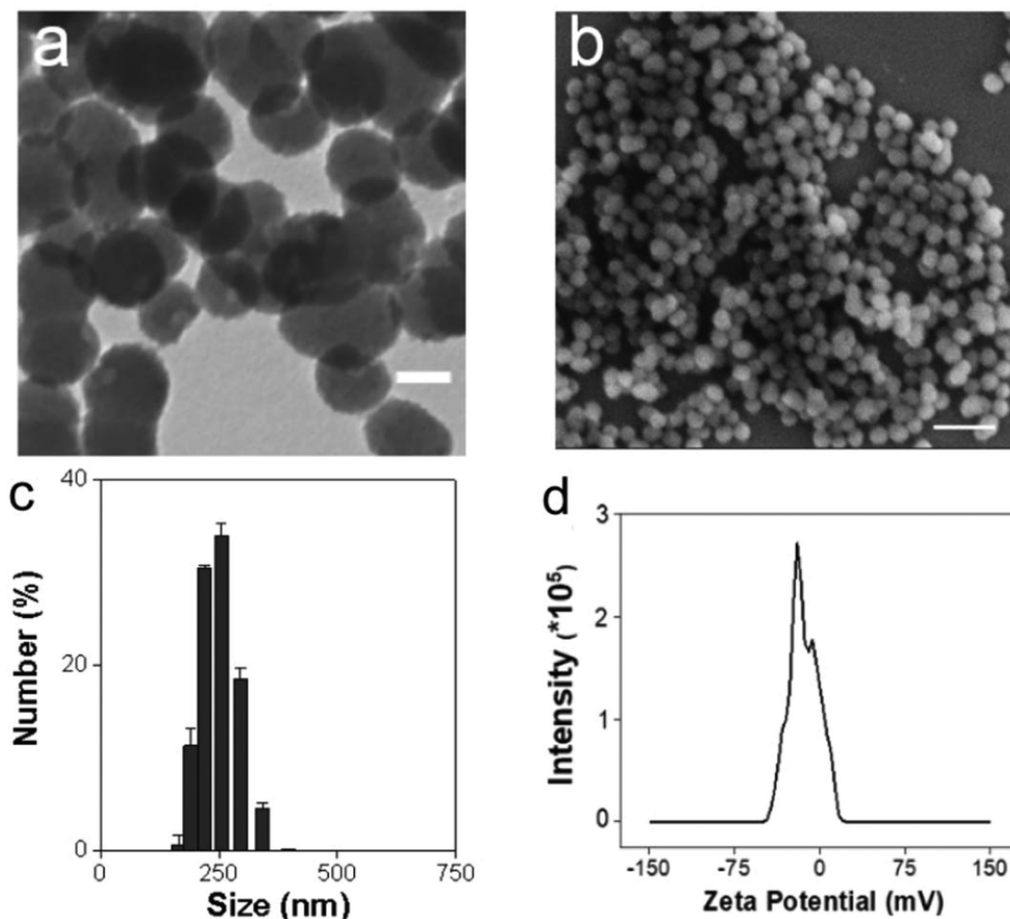


Figure 3.1. Physical characterizations of DM nanoparticles. (a) TEM of DM nanoparticles. (b) SEM of DM nanoparticles. (c) DLS of DM nanoparticles. (d) Zeta potential of DM nanoparticles.

We then analyzed the capacity of DM nanoparticles for scavenging radicals (**Figure 3.2**). We first assessed free radical scavenging by DPPH assay. Our studies showed effective and concentration dependent DPPH suppression (**Figure 3.2a**). Compared with PBS control, DM nanoparticles (80 $\mu\text{g/mL}$) inhibited the DPPH fluorescence by 64%. Similarly, Evans Blue bleaching, NBT reduction and deoxyribose test-tube method assays showed significant sequestration with peroxynitrite, superoxide, and hydroxyl radicals (**Figure 3.2b, c, d**). These

results confirm the capacity of melanin nanoparticles to efficiently scavenge a broad range of ROS and RNS.

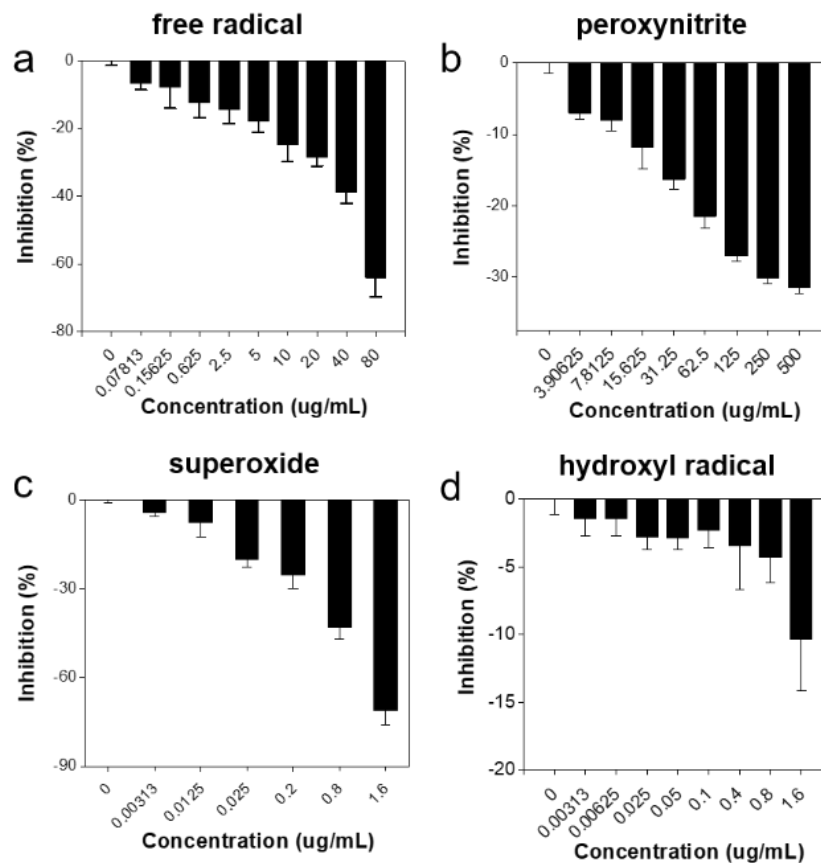


Figure 3.2. DM nanoparticles as a radical scavenger. (a) Free radical inhibition by DM nanoparticles. (b) The capacity of DM nanoparticles to scavenge peroxynitrite radicals. (c) Superoxides inhibition by DM nanoparticles. (d) The capacity of DM nanoparticles to scavenge hydroxyl radicals.

Anti-inflammatory and chondro-protective effects of DM nanoparticles on IL-1 β - induced chondrocytes

We first studied the chondro-protective effects of DM nanoparticles. This was investigated with rat chondrocytes with IL-1 β . As shown in **Figure 3.3a**, DM nanoparticles showed no cytotoxicity below 120 $\mu\text{g/mL}$ but rather increased the chondrocytes viability. In particular, DM nanoparticles of 10, 30 and 60 $\mu\text{g/mL}$ significantly promoted cell growth compared with the IL-1 β control ($P<0.001$). Thus, DM nanoparticles of 10, 30 and 60 $\mu\text{g/mL}$ were chosen for further investigation.

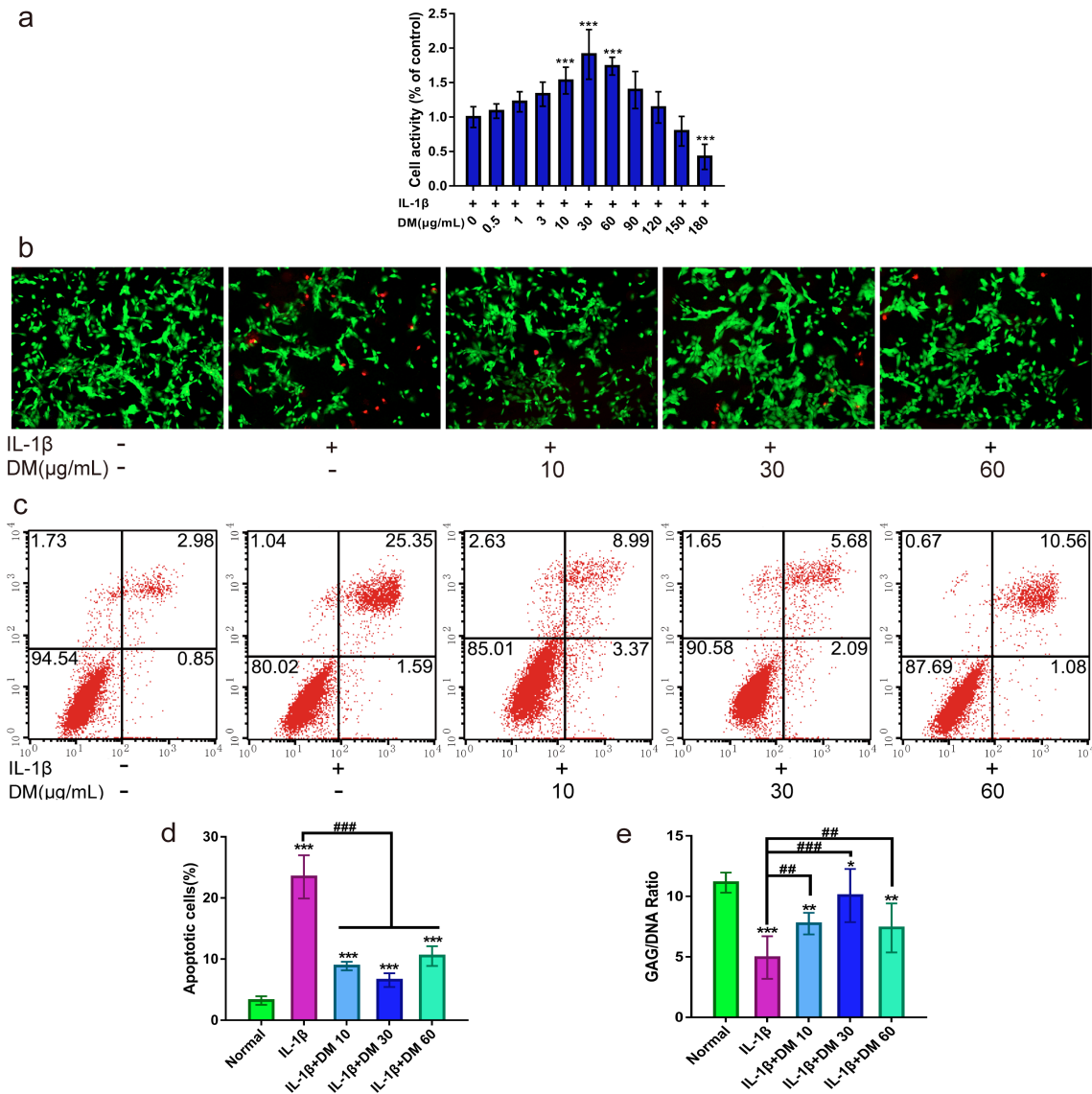


Figure 3.3. Chondro-protective effects of DM nanoparticles on IL-1 β - induced chondrocytes. MTT assay was to detect the cytotoxicity of DM nanoparticles. (Control: only with 10ng/mL IL-1 β). (b-e) Chondrocytes were treated with IL-1 β (10 ng/mL) and/or various concentrations of DM nanoparticles (10, 30, 60 μ g/mL) for 24 hours. (b) FDA//PI stained for cell viability. (c) Flow cytometry for cell apoptosis. (d) Quantitative flow cytometry for apoptosis. (e) Quantification of matrix production of GAG (n=6) for cell proliferation. Normal (without IL-1 β); IL-1 β (with 10ng/mL IL-1 β); IL-1 β +DM 10 (with 10ng/mL IL-1 β and 10 μ g/ml DM nanoparticles); IL-1 β +DM 30 (with 10ng/mL IL-1 β and 30 μ g/ml DM nanoparticles); IL-1 β +DM 60 (with 10 ng/mL IL-1 β and 60 μ g/ml DM nanoparticles). Values are the means \pm SD, n=6, * indicate $p < 0.05$, ** indicate $p < 0.01$, *** indicate $p < 0.001$ relative to respective control groups; # indicate $p < 0.05$, ## indicate $p < 0.01$, ### indicate $p < 0.001$.

This chondro-protective effect was confirmed by FDA/PI live/dead assay. As shown in **Figure 3.3b**, a significantly reduced number of live cells (green) and an increased number of dead cells (red) were found in chondrocytes treated with IL-1 β . This toxicity was largely inhibited when DM nanoparticles were co-incubated, with 30 μ g/ml DM showing the most prominent viability improvement. The cyto-protective effects of DM nanoparticles were further analyzed by flow cytometry. As shown in **Figure 3.3c, d**, IL-1 β induced remarkable chondrocyte death with the apoptosis level increased by 7.51 fold relative to the PBS control. On the contrary, co-incubation with DM nanoparticles greatly attenuated IL-1 β induced cell apoptosis, decreasing the population by 64.50%, 77.59% and 58.34%, respectively, when the DM concentration was 10, 30, 60 μ g/mL.

During cartilage development, GAGs play an important role in the integrity of the cartilage matrix. Loss of GAG is a hallmark for early-stage OA ¹⁹⁶. To evaluate the impact of DM

nanoparticles on GAG expression, we used DMMB assay. As shown in **Figure 3.3e**, a significant loss of GAGs in chondrocytes was induced by IL-1 β (up to 58.39%). However, DM nanoparticles rescued IL-1 β induced GAG loss, restoring its contents by 50.98 %, 56.86% and 47.06% for 10, 30 and 60 μ g/mL DM nanoparticles respectively. 30 μ g/ml DM in particular promoted the GAG production to nearly a normal level.

Protective effects of DM nanoparticles on IL-1 β -induced inflammation

In order to further explore the effects of DM nanoparticles on mRNA levels of inflammatory factors such as IL-6, IL-1 β , TNF- α , MMP-13, COX-2 and iNOS, chondrocytes were pre-treated with DM nanoparticles for 2 h, followed by IL-1 β treatment for 24 h. As shown in **Figure 3.4a**, the expression of inflammatory markers was remarkably elevated after IL-1 β treatment. As a comparison, DM nanoparticles led to significant decreased regulation of all tested mRNA. Particularly, 30 μ g/ml DM nanoparticles induced the most prominent decline, with all inflammatory factors approximating normal chondrocytes. This was further confirmed by Western blot analysis (**Figure 3.4b**), which showed that DM nanoparticles at 30 μ g/mL greatly inhibited IL-1 β induced upregulation of the inflammatory factors at the molecular levels.

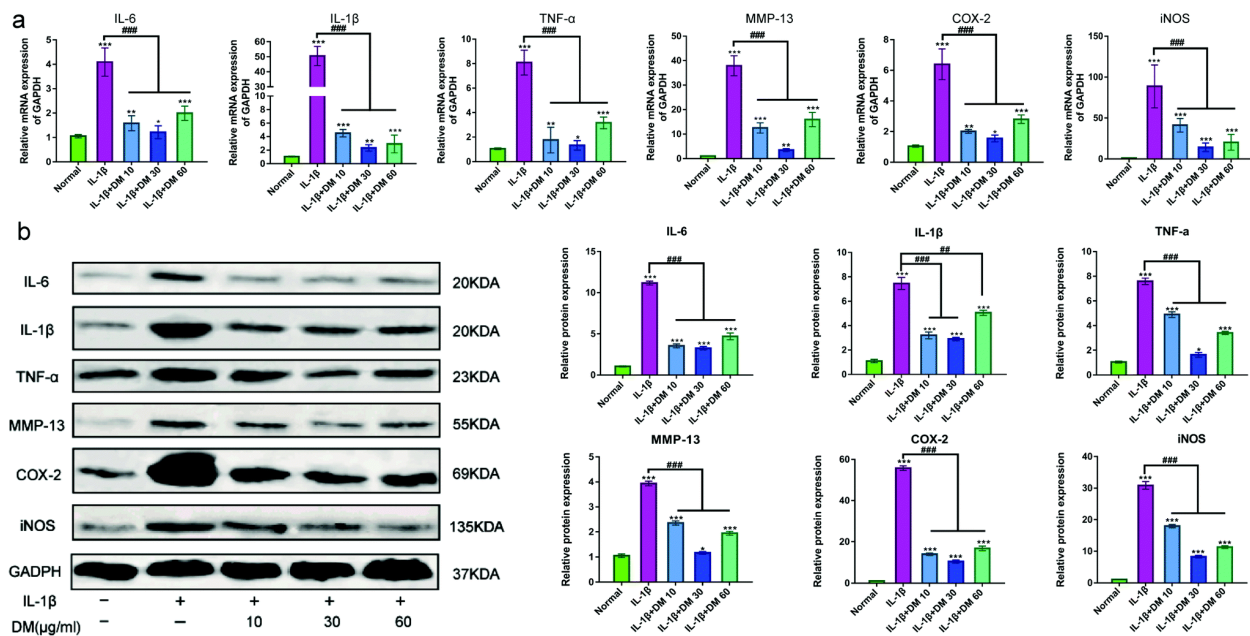


Figure 3.4. Effect of DM nanoparticles on the treatment of OA. (a) QRT-PCR was used to analyze the gene expression levels of IL-1 β , TNF- α , IL-6, MMP-13, COX-2 and iNOS in vitro. (b) Western Blot was used to analyze the protein expression of IL-1 β , TNF- α , IL-6, MMP-13, COX-2 and iNOS. Values are the means \pm SD, n=6, * indicate p <0.05, ** indicate p <0.01, *** indicate p <0.001 relative to respective control groups; # indicate p <0.05, ## indicate p <0.01, ### indicate p <0.001.

DM nanoparticles suppressed IL-1 β -induced free radicals

Intracellular ROS generation induced by IL-1 β was investigated by flow cytometry. As shown in **Figure 3.5a, b**, increased ROS was produced in IL-1 β -mediated chondrocytes over time. Nevertheless, administration of DM nanoparticles remarkably reduced the ROS production. Especially at the time point of 24 h, ROS was reduced greatly, close to the level of normal cells. Of note, there was a slight increase of ROS production ranged from 3 h to 6 h, followed by a drop afterwards. These results indicated DM nanoparticles have powerful ability to scavenge intracellular ROS.

Next, we detected intracellular levels of RNS using BBoxiProbeTM R21 fluorescent probe. As shown in **Figure 3.5c**, IL-1 β mediated the increase of RNS production, which was 12.43 times higher than that of the normal group. The treatment of DM greatly reduced the production of RNS in a dose-dependent manner. Administration of 30 μ g/mL DM led to a decrease of 75.86 % in RNS levels compared with IL-1 β group.

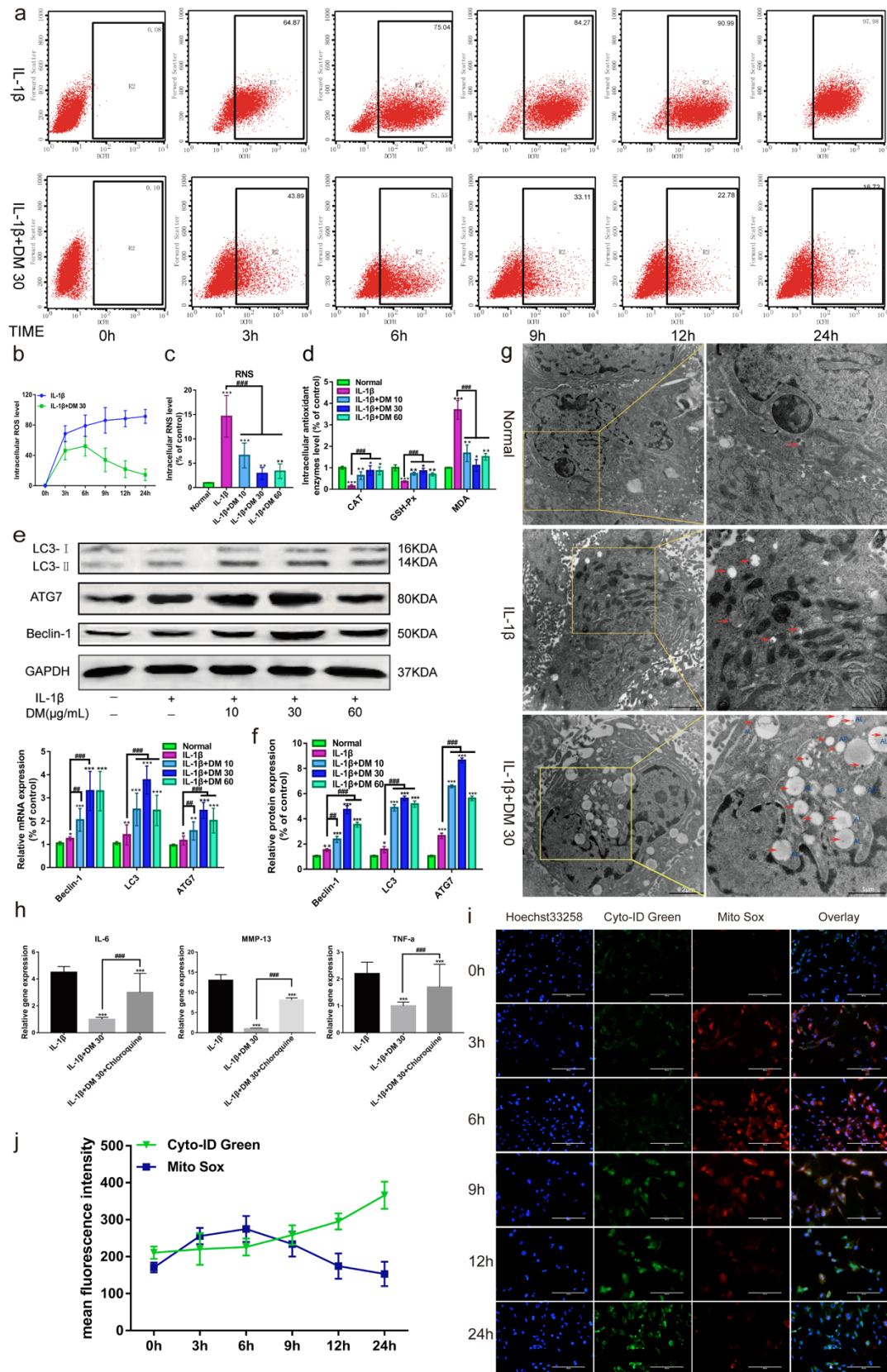


Figure 3.5. Effect of DM nanoparticles on the oxygen free radicals and autophagy. The chondrocytes stained with DCFH 30 minutes, followed by analyzed using flow cytometry. Upper-right corner region represents Chondrocyte ROS levels. (b) Quantifying the production of ROS in chondrocytes from flow cytometry. (c) Quantifying the production of RNS in chondrocytes. (d) Production of CAT, GSH-Px, MDA was assayed by a microplate fluorescence reader. (e) Western Blot was used to analyze the protein expression of LC3, ATG7 and Beclin-1. (f) QRT-PCR was used to analyze the gene expression of LC3, ATG7 and Beclin-1 in vitro. (g) TEM was used to analyze the uptake of DM nanoparticles and intracellular autophagy. (h) QRT-PCR was used to analyze the gene expression of MMP-13, IL-6 and TNF- α after Chondrocytes Treated with Autophagy Inhibitor Chloroquine. IL-1 β (with 10 ng/mL IL-1 β); IL-1 β +DM (with 10ng/mL IL-1 β and 30 μ g/ml DM nanoparticles); IL-1 β +DM+Chloroquine (with 10 ng/mL IL-1 β , 30 μ g/ml DM nanoparticles and 1 μ mol/L Chloroquine). (i) After treated with DM nanoparticles (30 μ g/mL) and IL-1 β (10 ng/mL) for 0h, 3h, 6h, 9h, 12h and 24h, cell samples concurrently stained with Cyto-ID Green dye and MitoSox Red dye were analyzed by confocal microscopy. (j) The fluorescence intensity of chondrocytes was analyzed by Image J. (Values are the means \pm SD. n=6, * indicate $p < 0.05$, ** indicate $p < 0.01$, *** indicate $p < 0.001$ relative to respective control groups; # indicate $p < 0.05$, ## indicate $p < 0.01$, ### indicate $p < 0.001$. Scale bars, 200 μ M.

Further, we detected intracellular antioxidant enzymes CAT and GSH-Px, which are key indicators of oxidative stress. As shown in **Figure 3.5d**, the levels of CAT and GSH-Px in chondrocytes were notably down-regulated by IL-1 β , while the downregulation was reversed by DM nanoparticles treatment. 30 μ g/mL of DM nanoparticles, in particularly, upregulated the levels of CAT and GSH-Px the most in all the groups. MDA, which is one of compounds produced in

the process of lipid peroxidation was also investigated. As shown in **Figure 3.5d**, MDA activity was dramatically activated in the IL-1 β group compare with normal cells, but suppressed after DM treatment. Especially in the IL-1 β +30 group, MDA level comes up to that in normal cells. These results revealed that DM nanoparticles act as potent ROS scavengers protect chondrocytes from damage by reducing excessive intracellular oxidative stress.

DM nanoparticles stimulate autophagy for chondrocyte protection

Autophagy as a protective process in the pathogenesis of OA has been demonstrated¹⁹⁷. It was also shown that enhanced autophagy is linked to consumption of excessive ROS and thus protection of chondrocytes¹⁹⁸. Quantitative RT-PCR analysis showed that IL-1 β led to a marginal increase of specific autophagy markers, including LC3-II, ATG7 and Beclin-1, compared with normal chondrocytes. By contrast, DM nanoparticles drastically elevated the expression of these autophagy markers in IL-1 β -pretreated chondrocytes (**Figure 3.5f**). In particular, 30 μ g/ml DM nanoparticles showed the most prominent induction. Western blot analysis also confirmed this, finding that LC3, ATG7 and Beclin-1 protein levels were significantly increased upon DM nanoparticles treatment (**Figure 3.5e**). Conversion of LC3-I to LC3-II is an initiating step in autophagy. It is noteworthy that the production of LC3-II in OA chondrocytes was facilitated by DM nanoparticles, indicating autophagy activation. Further, a large number of autophagosomes were observed in chondrocytes treated with 30 μ g/ml DM nanoparticles using TEM (**Figure 3.5g**).

For further validation, we con-incubated chondrocytes with chloroquine, an autophagy inhibitor. As shown in **Figure 3.5h**, quantitative RT-PCR results showed increased levels of inflammatory factors (MMP-13, IL-6, and TNF- α) when IL-1 β -induced chondrocytes were incubated with DM nanoparticles in the presence of chloroquine. This indicated that autophagy inhibition attenuates the anti-inflammatory and chondro-protective effects of DM nanoparticle.

Taken together, these findings demonstrate that DM nanoparticles may suppress IL-1 β -induced oxidative stress by activating autophagy.

DM nanoparticles mediated ROS scavenging followed by autophagy activation

In order to verify the sequential events of DM nanoparticle-mediated autophagy and ROS scavenging in IL-1 β -induced OA chondrocytes, we used immunofluorescence assay with cyto-ID Green probe for autophagy and MitoSox Red dye for ROS at different time point. At the first 6h, oxidative fluorescence (red) intensified gradually, while the intensity of autophagic fluorescence (green) remained weak (**Figure 3.5i, j**). Interestingly, the autophagic fluorescence was enhanced dramatically in a time-dependent manner between 6 to 24 h. In contrast, the intensity of oxidative fluorescence decreased sharply. These indicated that ROS was cleared while autophagy was activated.

Therapy studies in ACLT-induced rat OA models

To assess the effect of DM nanoparticles on pathological manifestations of OA, we established an OA model of rats by conducting an anterior cruciate ligament transaction (ACLT) surgery at the lower end of the femur and the upper end of the tibia in the knee-joint. And i.a. injection of DM nanoparticles with three different doses (10, 30, and 60 $\mu\text{g/mL}$, 0.1mL) was performed. Degeneration of cartilage was evaluated by macroscopic observation. As shown in Figure 6a, characteristics of OA, such as erosion and osteophyte formation was observed in the femoral condyles and tibial plateau in the ACLT surgery group (OA), while the normal cartilage was presented with a glistening, smooth surface without any defects and osteophyte formation (sham-operation group). However, 4-week injection of DM nanoparticles led to markedly reduced cartilage damage with the glistening cartilage surfaces resembling normal cartilage. Among all the treatment groups, 30 $\mu\text{g/mL}$ DM nanoparticles showed the best performance. Consistent with the

macroscopic observation, the macroscopic scores were ranked in the order of OA, DM 10, DM 60 and DM 30 (**Figure 3.6b**).

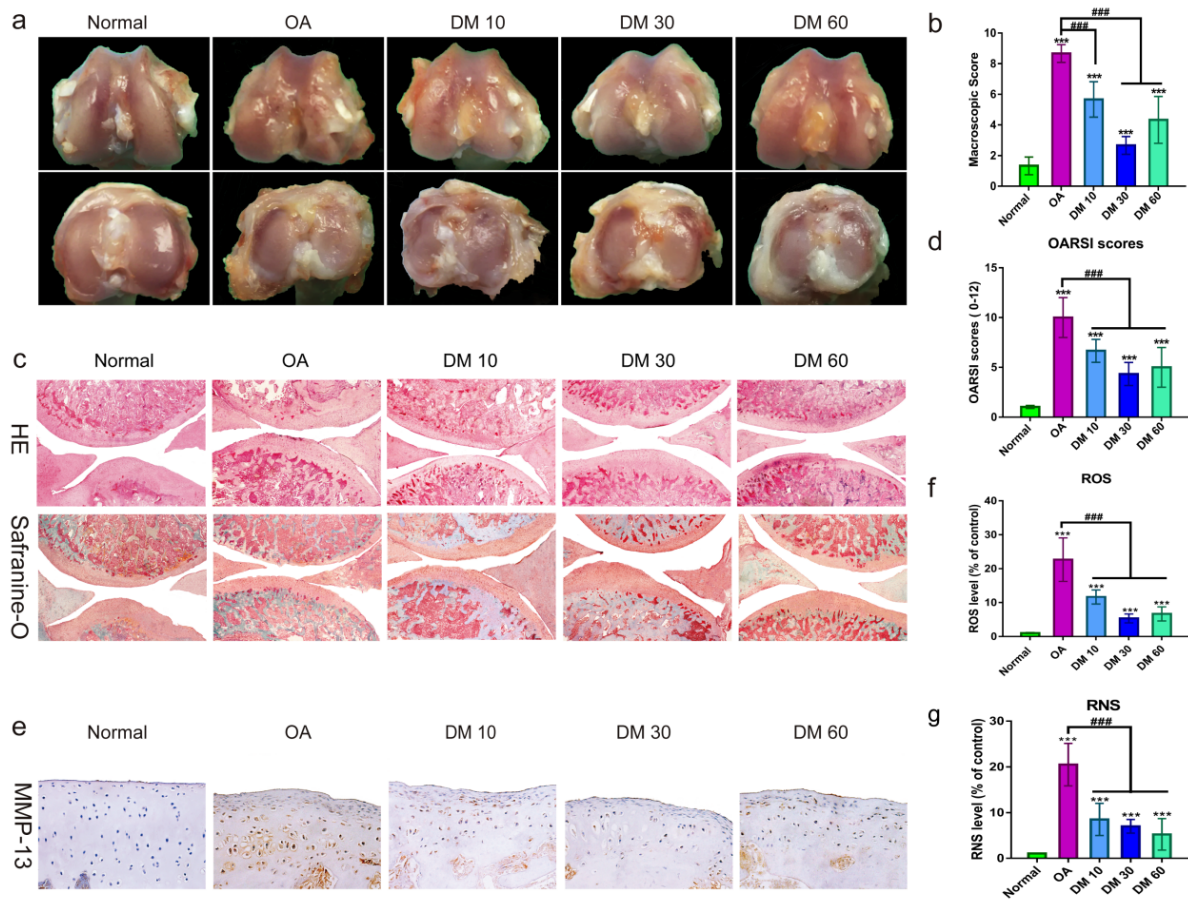


Figure 3.6. Effect of DM nanoparticles on ACLT-induced OA. SD rats were randomly divided into five groups: Normal group, OA group, DM 10 group, DM 30 group, DM 60 group. Normal group underwent sham operation, DM 10 group, DM 30 group and DM 60 group respectively received different concentrations of DM nanoparticles (10, 30, and 60 $\mu\text{g/mL}$), while OA group received with nothing in OA rats. All the samples were harvested after 8 weeks. (a) Macroscopic appearance. (b) Macroscopic scores of femoral condyles from normal and OA rats. (c) Histological analysis of OA was evaluated by Hematoxylin-Eosin staining and Safranin O staining. (d) OARSI

score of articular cartilage was determined. (e) (f) Quantifying the production of ROS in articular cartilage. (g) Quantifying the production of RNS in articular cartilage. Values are the means \pm SD, n=6, * indicate $p < 0.05$, ** indicate $p < 0.01$, *** indicate $p < 0.001$ relative to respective control groups; # indicate $p < 0.05$, ## indicate $p < 0.01$, ### indicate $p < 0.001$.

Histopathological examination by H&E and Safranin-O fast green staining showed severe pathologic changes in the OA group, as evidenced by fissures and fibrillation, a loss of cartilage superficial zone and osteophyte proliferation (**Figure 3.6c**). On the contrary, DM nanoparticles significantly slowed down cartilage degeneration, manifested in a remarkable reduction in the severity of histologic lesions and an increased GAG content. The OARSI Score was used to assess cartilage degeneration and damage (**Figure. 3.6d**). Relative to the OA control, 10, 30 and 60 $\mu\text{g/mL}$ DM nanoparticles reduced the OARSI score by 27.28%, 52.52% and 45.46 % respectively, which is consistent with the macroscopic findings.

As a marker of OA, MMP-13 is commonly used in the evaluation of OA. As shown in **Figure 3.6e**, intense positive staining of MMP-13 was observed in the cartilage layer of the OA group. As a comparison, much less positive staining was shown in DM nanoparticles groups, particularly the 30 $\mu\text{g/mL}$ group. In addition, we examined ROS production in the articular cartilage using BBcellProbeTM probe. As shown in **Figure 3.6f, g**, ROS and RNS levels were increased by 24.35 and 28.87 times, respectively, in OA group. With DM nanoparticles therapy, on the other hand, the ROS and RNS levels in cartilage were dramatically reduced. In summary, these results suggest that DM nanoparticles could effectively scavenge free radicals in the articular cartilage and as a result alleviate pathological progression of OA.

Discussion

Under physiological conditions, minute concentrations of ROS and RNS have important roles in various aspects of intracellular signaling and metabolic regulation¹⁹⁹. Excessive ROS and RNS produced by injured chondrocytes accelerate cell death and cartilage degradation in OA progression²⁰⁰⁻²⁰⁴. ROS scavengers have been demonstrated as effective OA therapeutics, but many are associated with poor biocompatibility, low degradation, or short drug retention. In this study, we are the first to explore DM nanoparticles as a safe therapeutic for OA treatment. We found that DM nanoparticles prevented elevated oxidative stress and autophagy, both contributing to inhibited cartilage remodeling in inflammatory diseases.

It has been reported that high density of extracellular matrix (ECM) of avascular cartilage hinders drug penetration and that nanoparticles with a size between 100 to 300 nm are favorable with regard to entering the cartilage ECM while staying long in the joint²⁰⁵. DM nanoparticles have an average diameter of 112.5 nm (**Figure 3.1a, b**) and a hydrodynamic size of 230 nm (**Figure 3.1c**), and are well within this optimal nanoparticle size range. The nanoparticles' colloidal stability comes from their negatively charged surface (-13.5 mV, **Figure 3.1d**), that prevents nanoparticles aggregation²⁰⁶.

In this study, we found that DM nanoparticles exhibited the capacity of scavenging multiple types of ROS and RNS (**Figure 3.2**), which is beneficial for protecting chondrocytes from oxidative stress, inflammatory reactions, and cartilage degeneration (**Figure 3.3, 3.4, 3.6**). RNS and ROS play an essential role in OA development and progression¹⁸⁴, and are potential therapy targets. NO inhibition may maintain the articular phenotype by maintaining Dickkopf-1 (DKK1) and Frizzled related protein (FRZB)²⁰⁷ and suppressing the release of NO, ROS, PGE2 and MMP-13, thus attenuating chondrocyte death in OA²⁰⁸. Salerno et al. reported that iNOS knockout mice

have lower rates of OA compared with the wild type ²⁰⁹. DM nanoparticles serve as a trap for potentially harmful radicals because they contains quinone residues ²¹⁰ that can react with ROS ²¹¹. DM nanoparticles as a dopamine derivative can also react with RNS and thus inhibiting their nitrating effects ²¹². This includes reduced NO production and protection against LPS-induced cell damage ²¹³. Previous studies showed that increased levels of ROS and RNS, can modify the Cys residues at the DNA-binding sites and influence the binding between DNA and transcription factors ²¹⁴, leading to proteoglycan loss in chondrocytes²¹⁵⁻²¹⁷ and thus cartilage degradation ²¹⁸.

Interestingly, we found that DM nanoparticles exert anti-inflammatory and chondro-protective effects by autophagy activation, which was demonstrated by the increased production of LC3-II/LC3-I, ATG7 and Beclin-1 and induced autophagic vesicles formation in chondrocytes (**Figure 3.5e, f, g**). Treatment of an autophagy inhibitor, chloroquine, reversed the anti-inflammatory effect of DM nanoparticles, evidenced by increased production of MMP-13, IL-1 β and TNF- α (**Figure 3.5h**). These results suggest that ROS and RNS scavenging effects of DM nanoparticles might be related to its autophagy activation. Autophagy is a vital cellular homeostatic mechanism for eliminating damaged cellular organelles and macromolecules ²¹⁹. It was found that autophagic activity decreases with aging, meaning better cyto-protective effects in young cartilage ²²⁰ to prevent damage caused by ROS and inflammatory cytokines ^{221, 222}. Pharmacological activation of autophagy is widely used in OA therapy ^{197, 223, 224}. Over-expression of iNOS inhibits autophagosome formation²²⁵ and NO inhibits autophagy by downregulating JNK1 by S-nitrosylation and activating the mTOR complex1 ²²⁶. As a ligand of DRD3 (dopamine receptor D3), dopamine could induce the DRD3 internalization and LC3B upregulation, activating autophagy ²²⁷ through the PI3K/Akt and mTOR pathways ²²⁸.

Conclusion

In conclusion, as a novel ROS and RNS scavengers, DM nanoparticles alleviated the pathological process of OA and cartilage degeneration. DM nanoparticles exert excellent anti-inflammatory effects by inhibiting intracellular ROS and RNS generation and activating antioxidant enzymes by autophagy, thereby inhibiting cartilage degradation and OA progression. This study provides a novel insight for therapy of OA by nanoparticulated ROS and RNS scavengers.

Materials and Methods:

Materials

Dopamine hydrochloride (Sigma-Aldrich, H8502), ammonium hydroxide (Sigma-Aldrich, 320145), H₂O₂ (Fisher Chemical, H325-500), nitrotetrazolium blue chloride (NBT, Sigma-Aldrich, N6876), deoxyribose (Sigma-Aldrich, 121649), ferric chloride (Acros Organics, 423705000), ascorbic acid (Sigma-Aldrich, A5960), riboflavin (Sigma-Aldrich, PHR1054), ethylenediaminetetraacetic acid (EDTA, Sigma-Aldrich, EDS-500G), NaCN (Alfa Aesar, L13278), 2,2 diphenyl-1-picryl hydrazyl (DPPH, Sigma-Aldrich, D9132), sodium nitroprusside (Sigma-Aldrich, PHR1423), HCl (baker analyzed, 0000170466), potassium nitrite (Fisher Scientific, P263-500), diethylenetriaminepentaacetic acid (DTPA, Sigma-Aldrich, D6518), peroxyxynitrite (Cayman, 81565), Evans Blue (Sigma-Aldrich, E2129), trichloroacetic acid (Fisher Scientific, ICN15259291)

Synthesis of dopamine melanin nanospheres

Two milliliters of ammonium hydroxide (28-30%) was added to a mixed solution containing 40 mL ethanol and 90 mL DI water. The solution was magnetically stirred at 30°C for

30 minutes. 0.5 g of dopamine hydrochloride in 10 mL DI water was dropwise added into the above solution. The color of the solution immediately turned to pale yellow and gradually become dark brown. The solution was magnetically stirred for another 24 hours. The products were collected by centrifugation and purified three times with DI water.

Characterization of DM Nanoparticles

Physical characterizations

Scanning electron microscopy (SEM) images were acquired on a FEI Teneo field emission SEM. Transmission electron microscopy (TEM) was carried out on a FEI Tecnai 20 transmission electron microscope operating at an accelerating voltage of 200 kV. Particle size distribution was analyzed on a Malvern Zetasizer Nano ZS system. Fourier-transform infrared (FT-IR) spectra were recorded on a Nicolet iS10 FT-IR spectrometer ²²⁹. HNMR analysis was performed on a Varian Mercury Plus 400 system. Zeta potential was measured by Zetasizer Nano-ZS.

Radical scavenging assays

DPPH assay: Free radical-scavenging capacity of DM nanoparticles was also measured by the DPPH scavenging method ²³⁰. The test was carried out in a 96 well plate using a total volume of 200 μ L methanol containing 0.004 μ g DPPH and a series of sample aliquots with the final concentration at 1, 0.5, 0.25, and 0.125 μ g/mL. The measurements were done in triplicate. DPPH solutions at the same concentration without the tested samples were used as control. The 520-nm absorbance was read every 5 min for 30 min. Samples were analyzed in triplicate.

Peroxynitrite assay: The peroxynitrite scavenging capacity was determined by Evans Blue bleaching assay with slight modifications. The reaction mixture contained 50 mM phosphate buffer (pH 7.4), 0.1 mM DTPA, 90 mM NaCl, 5 mM KCl, 12.5 μ M Evans Blue, various concentrations of DM nanoparticles (10–400 μ g/mL), and 1 mM peroxynitrite, and the final volume of the

solution was 1 mL. The absorbance at 611 nm was measured 30 min later. The percentage of ONOO- that was scavenged was calculated by comparing the results with the blank samples. Gallic acid was used as the standard.

Superoxide radical assay: The superoxide radical generated from the photo reduction of riboflavin was detected by NBT reduction ²³¹. The reaction mixture in PBS (67 mM, pH 7.8) contained EDTA (0.1 M), 0.0015% NaCN, riboflavin (0.12 mM), NBT (1.5 mM) and various concentrations of DM nanoparticles (10-1000 µg/mL) and the total volume was 3 mL. The tubes were uniformly illuminated by light for 15 min. The optical density at 530 nm was measured before and after the illumination.

Hydroxyl radical assay: The scavenging capacity against hydroxyl radicals was measured using the deoxyribose test-tube method with minor changes ²²⁹. All solutions used as freshly prepared. These include 200 µL of 2.8 mM 2-deoxy-2-ribose, 5 µL of DM nanoparticles (3.125 µg/mL - 400 µg/mL), 400 µL of 200 mM FeCl₃, 1.04 mM EDTA, 200 µL H₂O₂ (1.0 mM), and 200 µL ascorbic acid (1.0 mM). The resulting mixture was incubated for 1 h at 37°C. 1.5 mL aqueous solution containing 2.8% TCA was added, and the solution was first kept at room temperature for 20 min and then at 90°C for 15 min. Afterwards, the solution was cooled down and the absorbance at 532 nm measured and compared.

Isolation and culture of chondrocytes

Primary chondrocytes were isolated from knee joint cartilage of 3-day-old Sprague-Dawley (SD) rats (Guangxi Medical University, Experimental Animal Center). Articular cartilage tissue was finely minced, rinsed with phosphate-buffered saline (PBS), and digested with 2mg/mL of collagenase II (Solarbio,USA) at 37 °C for 4 h after treatment with 0.25% trypsin/EDTA (Solarbio,USA) for 30 min. And chondrocytes were obtained from articular cartilage tissue and

cultured in alpha-modified eagle's medium (α -MEM, Gibco, USA) supplemented with 10% (v/v) fetal bovine serum (FBS, Gibco, USA) and 1% (v/v) penicillin/streptomycin (Solarbio, China). Cells were detached from the culture dish using 0.25% trypsin and passaged after reaching confluency. Passage 2 chondrocytes were used for further experiments. To induce OA Chondrocytes, Chondrocytes were cultured with 10 ng/mL of IL-1 β for 24h. For therapeutic group, Chondrocytes were cultured with IL-1 β and/or different concentration of DM nanoparticles (10 μ g/ mL, 30 μ g/mL and 60 μ g/mL) for indicated time points.

Cytotoxicity assay

Chondrocytes were cultured in 96-well plates at the concentration of 10^4 cells/well and added 10 ng/mL of IL-1 β (Gibco, USA) and/or 10 different concentrations of DM nanoparticles (ranging from 0 to 180 μ g/mL) after 24 hours. MTT reagent (Gibco, USA) was added to culture medium after 24 hours of treatment with IL-1 β and DM nanoparticles, cells were then incubated at 37 °C for 4 hours. Absorbance of culture medium was measured using a spectrophotometer (Thermo, USA) at a wavelength of 490 nm. The three best concentrations of DM nanoparticle (10 μ g/mL, 30 μ g/mL and 60 μ g/mL) were selected for further experiments. The test is repeated three times.

Flow cytometry for detection of apoptosis: 1×10^6 chondrocytes were seeded in a six-well plate and treated with IL-1 β and/or DM nanoparticles for 24h. After that, cells were digested by trypsin without EDTA and collected by centrifugation. The resuspended chondrocytes were processed by using 10 μ L of Annexin V-EGFP (enhanced green fluorescent protein, Key GEN Bio TECH, China) and 5 μ L of Propidium Iodide (PI, Key GEN Bio TECH, China) in the dark for 20 minutes. The prepared samples were tested using a flow cytometer.

Live/dead assay

The chondrocytes incubated with 1 μ M calcein-AM and 1 μ M PI (Invitrogen, USA) in the dark at 37 °C for 5 minutes after washing three times with PBS. After a quick rinse in PBS, the image of live/death cells were acquired by laser scanning confocal microscopy (Nikon A1, Japan).

Confocal fluorescence assay: Autophagy and intracellular ROS level of chondrocytes was detected using Cyto-ID Autophagy Detection Kit (green, ENZO Life Science, USA) and MitoSox Red mitochondrial superoxide indicator (red, Eugene, USA), respectively. Cells were incubated with 10 ng/mL of IL-1 β and/or 30 μ g/mL DM Nanoparticles for indicated times, then the mixture of MitoSox Red, Cyto-ID Green Dye and Hoechst 33342 (green, ENZO Life Science, USA) were used to treat with cells at 37 °C for 15 minutes in the dark after cells were washing by PBS. Images were captured by confocal microscopy (Nikon A1, Japan) immediately after chondrocytes were washed with α -MEM. All the relative fluorescence intensity was measure by Image J (National Institutes of Health, NIH, USA).

Transmission electron microscopy (TEM)

TEM was used to observe the localization of DM nanoparticles and Autophagosome in chondrocytes. 30 μ g/mL of DM-treated cells were collected and centrifuged at 1000 rpm for 3 min. The centrifuged cell agglomerates were fixed by 2.5% (v/v) glutaraldehyde for 24h and 1% (v/v) osmium tetroxide for 2h to stabilize the organelles and phospholipid membranes of cell. The cells were dehydrated using a concentration gradient of alcohol (30%, 50%, 75%, 90%, 99%,100%) for 15 minutes each and embedded in resin after washing with PBS. Thin sections were sliced from embedded cells and stained with 2% aqueous uranyl acetate for 1h in the dark. Pictures were captured by a TEM (Hitachi H-7650, Japan).

Quantification of intracellular glycosaminoglycan (GAG): The content of intracellular DNA was detected using Hoechst 33258 (Sigma, USA) as previous described ²³². In briefly,

cellular DNA was stained by Hoechst 33258 dye and absorbance was measured at 460 nm by using fluorescence spectrophotometer (Bio-Tek Instruments, USA). Calf thymus DNA was used as the standard. Intracellular GAG secretion was detected using 1,9-dimethylmethylene blue assay (DMMB, Sigma, USA) and the absorption at wavelength of 525 nm was recorded on fluorescence spectrophotometer (Bio-Tek Instruments, USA), and chondroitin sulfate (Sigma, USA) was used as a standard. Finally, intracellular GAG secretion was normalized to the DNA content of the chondrocytes and express as GAG/DNA.

CAT, GSH-Px and MDA activity assay

After 24h of treatment with three different concentrations of DM nanoparticles (10 µg/mL, 30 µg/mL and 60 µg/mL) and/or 10 ng/mL of IL-1β, the cultured medium of cells were collected and subjected to detection of antioxidant capacity by using Glutathione peroxidase (*GSH-Px*) and Catalase(CAT) kit (Nanjing Jiancheng Bioengineering Institute, China) and evaluation of oxidative stress level by using Malondialdehyde (MDA) assay kits (Nanjing Jiancheng Bioengineering Institute, China) according to the instructions. Then the absorbance at 450 nm was recorded using a Fluorescence microplate reader (Bio-Tek Instruments, USA). All samples were repeated in triplicate.

Intracellular ROS measurement

Chondrocytes ROS level were detected by using Reactive Oxygen Species Assay Kit (Beyotime Biotechnology, China), respectively. Cells were washed with serum-free medium and loaded fluorogenic probes 2',7'-dichlorofluorescein diacetate (DCFH-DA). After incubation with 10 µM/L of DCFH-DA at 37 °C for 30 minutes, the cells were washed three times with serum-free medium. Subsequently, the DCFH- DA-loaded chondrocytes were divided into two aliquots and subjected to determination of relative fluorescent intensity by using a fluorescence

spectrophotometer and measurement of ROS levels by using Flow cytometer, respectively. All samples were repeated in triplicate.

Intracellular RNS measurement

Chondrocytes RNS level were detected by using Reactive Nitrogen Species Assay Kit (BestBio, China). Cells were washed and suspended with serum-free medium and loaded fluorogenic probes BBoxiProbeTM R21F. After incubation with 10 μ M/L of BBoxiProbeTM R21F at 37 °C for 30 minutes, the cells were washed three times with PBS. RNS levels were quantified by using a fluorescence microplate reader (Bio-Tek Instruments, USA) with excitation wavelength of 488 nm and emission wavelength of 516 nm. All samples were repeated in triplicate.

Quantitative real-time PCR

Total RNA was extracted from the chondrocytes using RNA extraction kit (Tiangen Biotech Co., Ltd., China) and digested with DNase to remove any contaminating genomic DNA in accordance with the manufacturer's instructions. First-strand complementary DNA (cDNA) was synthesized using reverse transcription kit (Fermentas Company, USA). The qRT-PCR was performed using FastStart Universal SYBR Green Master (Roche) by quantitative PCR detection system (Realplex 4, Eppendorf Corporation). The primer sequences were listed in Table 1. Relative gene expression levels were calculated using the 2- $\Delta\Delta$ CT method and normalized to GAPDH. All samples were repeated in triplicate.

Western blotting

Protein extracts were obtained from chondrocytes by RIPA lysis buffer (BOSTER, China) with 1 mM phenylmethanesulfonyl fluoride (PMSF, BOSTER, China). 50 μ g of protein extracts were subjected to electrophoresis on 10% SDS-PAGE gel, and transferred to a polyvinylidene fluoride (PVDF, Millipore, US) membrane after concentration of protein was detected by BCA

protein assay kit (Beyotime, China). The membranes were incubated with specific antibodies, including anti-IL-6 (BOSTER, China, 1:200), anti-IL-1 β (BOSTER, China, 1:200), anti-TNF- α (BOSTER, China, 1:200), anti-MMP-13 (BOSTER, China, 1:200), anti-COX-2 (BOSTER, China, 1:200), anti-iNOS (BOSTER, China, 1:200) anti-LC3 (BOSTER, China, 1:200), anti-ATG7 (BOSTER, China, 1:200), anti-Beclin-1 (BOSTER, China, 1:200) and anti-GAPDH (BOSTER, China, 1:200) overnight at 4 °C. Subsequently, membranes were incubated with horseradish peroxidase-labelled secondary antibody (Invitrogen, USA) for 2 hours after washing. The signals were visualized using Odyssey Infrared Imaging System (LI-COR Biotechnology, USA).

OA model establishment and treatment in vivo

Thirty 7-week-old female SD rats were provided by the Experimental Animal Center of Guangxi Medical University. The use of animals was approved by Animal Ethics Committee from the Experimental Animal Center of Guangxi Medical University and all animal manipulations were carried out strictly according to the National Institutions of Health Guide for the Care and Use of Laboratory Animals. To obtain rat model of OA, we used surgically induced method. After anesthesia with 10% chloral hydrate, anterior cruciate ligament transection (ACLT) was performed on the right knee of rat, meanwhile, sham surgery was performed with the same skin incision on the left knee of rat. The rats were randomly divided into five groups as following: Normal group (the rats without ACLT surgery and its joint cavity were injected with 0.2 mL of saline three times a week); OA group (the rats were administered by an intra-articular injection with 0.2 mL of saline three times a week after 4 weeks of ACLT surgery); DM nanoparticles therapeutic group (the rats were administered by an intra-articular injection with DM nanoparticles three times a week after 4 weeks of ACLT surgery). The therapeutic group was divided into 3

subgroups base on different concentration of DM nanoparticles (10µg/mL, 30µg/mL and 60µg/mL), which were represented by DM+10, DM+30 and DM+60, respectively.

After 4 weeks, the rats were sacrificed by overdose of chloral hydrate, and the cartilages of keen joint were harvested for further investigation. The severity of OA lesions was evaluated based on integer score for cartilage structural changes (score range 0-6, 0= normal cartilage structure and 5=erosion of the cartilage down to the subchondral bone), cellular changes (score range 0-3), H&E and Safranin-O fast green staining (score range 0-4) and tidemark integrity (scored rang 0-1).

ROS detection of articular cartilage: 50mg of fresh cartilage tissue from keen joint was made into homogenate with 1 mL of buffer, and homogenate was using and centrifuged at 4 °C for 10 minutes. 190 µL of supernatant was collected and incubated with 10 µL of BBcellProbe™ O11 ROS probe (BestBio, China) in a 96-well plate at 37 °C in the dark for 30 minutes. ROS levels were quantified by fluorescence microplate reader (Bio-Tek Instruments, USA) with excitation wavelength of 488 nm and emission wavelength of 530 nm. All samples were repeated in triplicate.

RNS detection of articular cartilage

Fifty mg of fresh cartilage tissue from keen joint was made into homogenate with 1 mL of buffer, and homogenate was using and centrifuged at 4 °C for 10 minutes. 190 µL of supernatant was collected and incubated with 10 µL of BBcellProbe™ O52F RNS probe (BestBio, China) in a 96-well plate at 37 °C in the dark for 30 minutes. RNS levels were quantified by fluorescence microplate reader (Bio-Tek Instruments, USA) with excitation wavelength of 488 nm and emission wavelength of 516 nm. All samples were repeated in triplicate.

Histological staining

The knee tissues from rat were fixed in 4% paraformaldehyde for 48 hours. After decalcification in 10% (w/v) Tris-EDTA for 4 weeks on a shaker, the fixed knee tissues were embedded in paraffin. The embedded tissues were then cut into 5 μ m frontal sagittal sections. Slides of femur and tibia were stained with Hematoxylin and Eosin (H&E) (Solarbio, China) and Safranin-O fast green (Solarbio, China). The morphological manifestations of cartilage and subchondral bone were observed in a double-blind manner using a microscope (Olympus, Japan), and cartilage degeneration of knee joint was evaluated using OA Research Society International scoring system (OARSI) as described previously²³³.

Immunohistochemical analysis

Immunohistochemical staining was performed to detect protein expression of MMP-13 (BOSTER, China) in articular cartilage. Briefly, the slices were incubated with primary antibody for MMP-13 (1:100) (BOSTER, China, 1:200) at 4°C overnight after deparaffinization of paraffin-embedded sections. After extensive washes with PBS, the sections were incubated successively with the second antibody (ZSGB Bio, China) for 15 minutes and biotin-labeled horse radish peroxidase (ZSGB Bio, China) for 15 minutes. Subsequently, the sections were counter-stained with hematoxylin (Solarbio, China) after processing with a 3, 3'-diaminobenzidine tetrahydrochloride (DAB) kit (BOSTER, China) according to the protocol. Neutral resin sealed-slices were prepared for observation and pictures were captured by an Inverted microscope (Olympus, Japan).

Statistical Analysis

All tests are performed at least triplicate. Statistical analysis of all data (mean \pm S.D, n = biological replicates) was analyzed by SPSS 64.0 (SPSS Inc., Chicago, Illinois, USA). Comparison between OA and treatment groups was examined by one-way analysis of variance (ANOVA).

$P < 0.05$ was considered statistically significant. Bars with different letters are significantly different from each other at $P < 0.05$, and those with the same letter exhibit no significant difference.

CHAPTER 4

INTRACISTERNAL ADMINISTRATION OF TANSINONE IIA-LOADED
NANOPARTICLES LEADS TO REDUCED TISSUE INJURY AND FUNCTIONAL
DEFICITS IN A PORCINE MODEL OF ISCHEMIC STROKE³

³ Xueyuan Yang[†], Elizabeth S. Waters[†], Erin E. Kaiser[†], Madison M. Fagan, Kelly M. Scheulin, Julie H. Jeon, Soo K. Shin, Holly A. Kinder, Anil Kumar, Simon R. Platt, Kylee J. Duberstein, Hea Jin Park, Jin Xie, Franklin D. West*, († Equal contribution) *IBRO Neuroscience Reports* 2021, 10, 18-30.
Reprinted here with permission of the publisher.

Abstract

Background:

The absolute number of new stroke patients is annually increasing and there still remains only a few Food and Drug Administration (FDA) approved treatments with significant limitations available to patients. Tanshinone IIA (Tan IIA) is a promising potential therapeutic for ischemic stroke that has shown success in pre-clinical rodent studies but lead to inconsistent efficacy results in human patients. The physical properties of Tan-IIA, including short half-life and low solubility, suggests that Poly (lactic-co-glycolic acid) (PLGA) nanoparticle-assisted delivery may lead to improve bioavailability and therapeutic efficacy. The objective of this study was to develop Tan IIA-loaded nanoparticles (Tan IIA-NPs) and to evaluate their therapeutic effects on cerebral pathological changes and consequent motor function deficits in a pig ischemic stroke model.

Results:

Tan IIA-NP treated neural stem cells showed a reduction in SOD activity in in vitro assays demonstrating antioxidative effects. Ischemic stroke pigs treated with Tan IIA-NPs showed reduced hemispheric swelling when compared to vehicle only treated pigs (7.85 ± 1.41 vs. $16.83 \pm 0.62\%$), consequent midline shift (MLS) (1.72 ± 0.07 vs. $2.91 \pm 0.36\text{mm}$), and ischemic lesion volumes (9.54 ± 5.06 vs. $12.01 \pm 0.17\text{cm}^3$) when compared to vehicle-only treated pigs. Treatment also lead to lower reductions in diffusivity (-37.30 ± 3.67 vs. $-46.33 \pm 0.73\%$) and white matter integrity (-19.66 ± 5.58 vs. $-30.11 \pm 1.19\%$) as well as reduced hemorrhage (0.85 ± 0.15 vs. $2.91 \pm 0.84\text{cm}^3$) 24 hours post-ischemic stroke. In addition, Tan IIA-NPs led to a reduced percentage of circulating band neutrophils at 12 (7.75 ± 1.93 vs. $14.00 \pm 1.73\%$) and 24 (4.25 ± 0.48 vs. $5.75 \pm 0.85\%$) hours post-stroke suggesting a mitigated inflammatory response. Moreover, spatiotemporal gait deficits including cadence, cycle time, step time, swing percent of cycle, stride

length, and changes in relative mean pressure were less severe post-stroke in Tan IIA-NP treated pigs relative to control pigs.

Conclusion:

The findings of this proof of concept study strongly suggest that administration of Tan IIA-NPs in the acute phase post-stroke mitigates neural injury likely through limiting free radical formation, thus leading to less severe gait deficits in a translational pig ischemic stroke model. With stroke as one of the leading causes of functional disability in the United States, and gait deficits being a major component, these promising results suggest that acute Tan IIA-NP administration may improve functional outcomes and the quality of life of many future stroke patients.

List of abbreviations

Food and Drug Administration (FDA), intracerebral hemorrhage (ICH), Tanshinone IIA (Tan IIA), Poly (lactic-co-glycolic acid) (PLGA), Tan IIA-loaded nanoparticles (Tan IIA-NPs), Tissue plasminogen activator (tPA), nanoparticle (NP), reactive oxygen species (ROS), damaged-associated molecular patterns (DAMPs), tumor necrosis factor γ (TNF- γ), interleukin 6 (IL-6), polyethyleneglycol-poly(lactic-co-glycolic acid) (PEG-PLGA), blood brain barrier (BBB), cerebral spinal fluid (CSF), central nervous system (CNS), Stroke Therapy Academic and Industry Roundtable (STAIR), white matter (WM), gray matter (GM), γ -aminobutyric acid (GABA), Tan IIA PLGA NPs (Tan IIA-NPs), midline shift (MLS), poly (lactide-co-glycolide)-b-poly (ethyleneglycol)-maleimide (PLGA-b-PEG-OH), Pioglitazone (Piog), Baicalin (Baic), Puerarin (Puer), Edaravone (Edar), Resveratrol (Resv), transmission electron microscopy (TEM), phosphate buffered saline (PBS), superoxide dismutase (SOD), inhibitory concentration (IC),

University of Georgia (UGA), intramuscular (IM), transdermal (TD), middle cerebral artery (MCA), middle cerebral artery occlusion (MCAO), T2 Fluid Attenuated Inversion Recovery (T2FLAIR), T2Weighted (T2W), T2Star (T2*), Diffusion-Weighted Imaging (DWI), and Diffusion Tensor Imaging (DTI), Apparent Diffusion Coefficient (ADC), fractional anisotropy (FA), double-distilled water (ddH₂O), analysis of variance (ANOVA), arbitrary units (AU), neural stem cells (NSCs), lipopolysaccharide (LPS), dynamic light scattering (DLS)

Introduction

The absolute number of new stroke patients has increased to an estimated 10.3 million people a year ²³⁴. Unfortunately, there are few Food and Drug Administration (FDA)-approved treatments for ischemic stroke with each possessing potential risk factors. Tissue plasminogen activator (tPA), for example, has a limited administration window with potentially deadly risk factors including intracerebral hemorrhage (ICH) ²³⁵. The limited therapeutic time window results in relatively low administration rates (<5% patients) of tPA. There is a clear need for further investigation of novel stroke therapies and delivery approaches that lead to robust recovery. Therapeutic approaches that modulate key processes in the secondary injury cascade including inflammation and oxidative stress are promising neuroprotective options ²³⁶. Tan IIA is one such neuroprotectant that acts as a free-radical scavenger and has antioxidant and anti-inflammatory effects post-stroke ^{237, 238}. Tan IIA has been shown to downregulate expression of IL-1 β and TNF- α and inhibit microglia activation, as well as reverse oxidative stress and apoptosis post-brain injury ²³⁹⁻²⁴². Similar to many other neuroprotective therapeutics, administration of Tan IIA has resulted in reduced lesion volumes, reduced edema, and blood brain barrier permeability. These tissue level changes resulted in decreased mortality and improved neurological function in

preclinical rodent studies of neural injury ²⁴²⁻²⁴⁴. However, Tan IIA and many other neuroprotective therapies have demonstrated limited efficacy in human clinical trials ^{245, 246}. One potential way to improve the efficacy of Tan IIA in humans is through the use of a nanoparticle (NP) delivery system. NP drug delivery can improve drug circulation time and control release over extended periods of time while simultaneously reducing toxicity ²⁴⁷. The disconnect in neuroprotectant success between preclinical rodent studies and clinical trials is likely in part due to major differences in size, cytoarchitecture, and physiology between rodent and human brains leading to dissimilar therapeutic responses ^{248, 249}. These inherent anatomical differences have led to a demand from the stroke therapeutic community for the development and testing of novel treatments in more representative translational animal models, such as the pig, that more closely resemble human brain anatomy and physiology ^{250, 251}.

Following the primary ischemic insult, a secondary injury cascade is initiated with the release of the excitatory neurotransmitter, glutamate, from dying neurons causing excitotoxicity, peri-infarct depolarizations, production of reactive oxygen species (ROS), and inflammation ^{252, 253}. Generated ROS leads to the damage of DNA, RNA, and critical cellular machinery leading to cell death. The increase in ROS, the release of damaged-associated molecular patterns (DAMPS), and hypoxia triggers an immune response including an increase in neutrophils and the production of inflammatory cytokines such as tumor necrosis factor α (TNF- α) and interleukin 6 (IL-6) ^{254, 255}. The secondary injury cascade leads to rapid and substantial brain damage. Therefore, inhibiting ROS production and inflammation may be a promising therapeutic target.

Tan IIA has been shown to have antioxidant and anti-inflammatory effects in rodent and human stroke studies ²⁵⁶. Rodent studies showed Tan IIA was effective in reducing brain edema and infarct volume in response to ischemic injury ^{243, 244, 256}. Reduced brain edema and lesioning

correlated with rodent improvements in overall neurological function post-stroke including limb mobility, ambulation, righting reflexes, and reduced circling behavior ²⁴³. Clinical trials testing Tan IIA in its purified or crude form (dried *Salvia miltiorhiza* root) has led to mixed efficacy results with studies showing significant to no improvements in clinical outcomes (e.g. cerebral blood flow, neurological symptoms, and muscle strength) of ischemic stroke patients ^{246, 257}. Conflicting results between rodent and human outcomes suggest Tan IIA may be a potentially effective treatment, yet further optimization is needed to achieve improved consistency in post-stroke outcomes.

In its purified form, Tan IIA has a short circulation half-life and poor solubility, which limits systemic drug concentrations and consequent pharmacological responses ^{258, 259}. Furthermore, the hydrophobic properties of Tan IIA reduces permeability and bioavailability, thus requiring higher administration doses ²⁵⁹. Polylactic-*co*-glycolic acid (PLGA) NPs are an FDA-approved copolymer made of lactic acid and glycolic acid. PLGA or the PEGylated derivative, polyethyleneglycol–polylactic-*co*-glycolic acid (PEG–PLGA), can encapsulate large amounts of hydrophobic molecules, like Tan IIA, and release them at a controlled rate ²⁶⁰. A sustained drug release improves drug bioavailability and reduces the frequency of drug administration. The controlled release, low toxicity, high biodegradability, low immunogenicity, and significant clinical experience makes PLGA a favorable nanoplatform for drug delivery ²⁶¹. Extensive preclinical and clinical studies confirm PLGA NPs are a safe and efficient delivery system ^{247, 260}. A PLGA NP delivery system could significantly improve the bioavailability, solubility, and pharmacological efficacy of Tan IIA in ischemic stroke patients. NP treatments are commonly delivered intravenously (IV), however this limits the therapeutic effects of NP delivered drugs for ischemic stroke as NPs cannot freely transverse the blood brain barrier (BBB). Intracisternal delivery of NPs may overcome this challenge as NPs do not need to cross the BBB due to direct

administration into the cerebral spinal fluid (CSF) of the central nervous system (CNS). Additionally, intracisternal NP treatments are not diluted in the circulatory system, removed by filtering organs such as the liver, thus lower NP concentrations are required, and the potential of off target effects in other organ systems is reduced.

The Stroke Therapy Academic and Industry Roundtable (STAIR) recommended preclinical testing of potential therapeutics in gyrencephalic species to increase the possibility of translating therapies to the clinic ²⁵⁰. The use of large animal models is an important step in the translational framework as most therapies that have reached and failed in clinical trials have been successfully tested in rodent models, indicating a need for a more predictive model. The pig has anatomical and physiological similarities to humans making it a robust model for studying novel therapeutics for ischemic stroke ²⁶². While rodent brains are lissencephalic and composed of <12% white matter (WM), both human and pig brains are gyrencephalic and composed of >60% WM ²⁶³. These differences have proven critically important in ischemic stroke pathology as WM and gray matter (GM) exhibit differing sensitivities to hypoxia, with WM more consistently injured in most stroke cases ^{264, 265}. The pathology of GM is believed to differ from WM in terms of lymphocyte infiltration, macrophage activity, and BBB alterations in response to injury ²⁶⁶. WM also has a greater dependence on Na⁺ and Ca²⁺ exchange, γ -aminobutyric acid (GABA), and adenosine with an autoprotective feed-back loop ²⁶⁷. These anatomical similarities support that stroke pathophysiology in the pig model is likely more representative of the human condition and therefore more predictive of human outcomes compared to traditional rodent models.

In this proof of concept study, Tan IIA PLGA NPs (Tan IIA-NPs) were characterized and demonstrated antioxidative and anti-inflammatory capabilities *in vitro*. Acute testing of Tan IIA-NPs in a pig model of ischemic stroke showed Tan IIA-NPs have a neuroprotective effect leading

to reduced cerebral swelling, lesion volume, and improved WM integrity. These tissue level improvements corresponded with improved motor function suggesting Tan IIA-NPs may be an effective treatment for ischemic stroke.

Results

Tan IIA and Baicalin drug characteristics enable NP drug delivery

Six neuroprotective drugs with antioxidative and/or anti-inflammatory properties were identified, Baicalin (Baic), Pioglitazone (Piog), Tan IIA, Puerarin (Puer), Edaravone (Edar), and Resveratrol (Resv), and were selected for testing as a NP based ischemic stroke therapy. These drugs were selected based on preclinical success in treating ischemic stroke, with some advancing and proving unsuccessful in human clinical trials, while also having biological characteristics that could benefit from the use of a NP delivery system such as a short half-life^{243, 244, 246, 268-276}. Puer, Edar, and Resv showed very low NP encapsulation efficiency (0.00, 0.125, and 0.132 %, respectively), due to their relatively high hydrophilicity, and therefore these drugs were eliminated from the study. Baic, Piog, and Tan IIA showed higher encapsulation efficiencies of 17.01, 4.90, and 15.90 %, respectively. Baic, Piog, and Tan IIA loaded NPs (henceforth referred to as Baic-NPs, Piog-NPs, and Tan IIA-NPs) were imaged using TEM and had an average size of 60.80, 74.20, and 52.20 nm, respectively (**Figure 4.1A**). Baic-NPs, Piog-NPs, and Tan IIA-NPs size was also assessed by dynamic light scattering (DLS), which found the hydrodynamic sizes to be 89.28 ± 1.8 , 122.40 ± 2.3 , and 91.34 ± 1.3 nm, respectively (**Figure 4.1B**). The relative increase of hydrodynamic sizes is attributed to surface PEGylation and hydration. Assessment of zeta potential showed that all three NPs have a negatively charged surface, 31.91, -27.39, -28.98 mV, respectively, which is due to the hydroxyl termini of the PEG chains (**Figure 4.1C**). For all three

formulations, the drug molecules were slowly released from NPs at acidic and more neutral pH levels (pH 5.5, 6.5, and 7.4; **Figure 4.1D**), which is beneficial from a sustained delivery perspective. However, while Tan IIA-NPs and Baic-NPs afford good colloidal stability, Piog-NPs showed a relatively high degree of aggregation after dispersing in phosphate buffered saline (PBS) for 2-3 hours. Hence, subsequent cellular tests focused on Baic-NPs and Tan IIA-NPs.

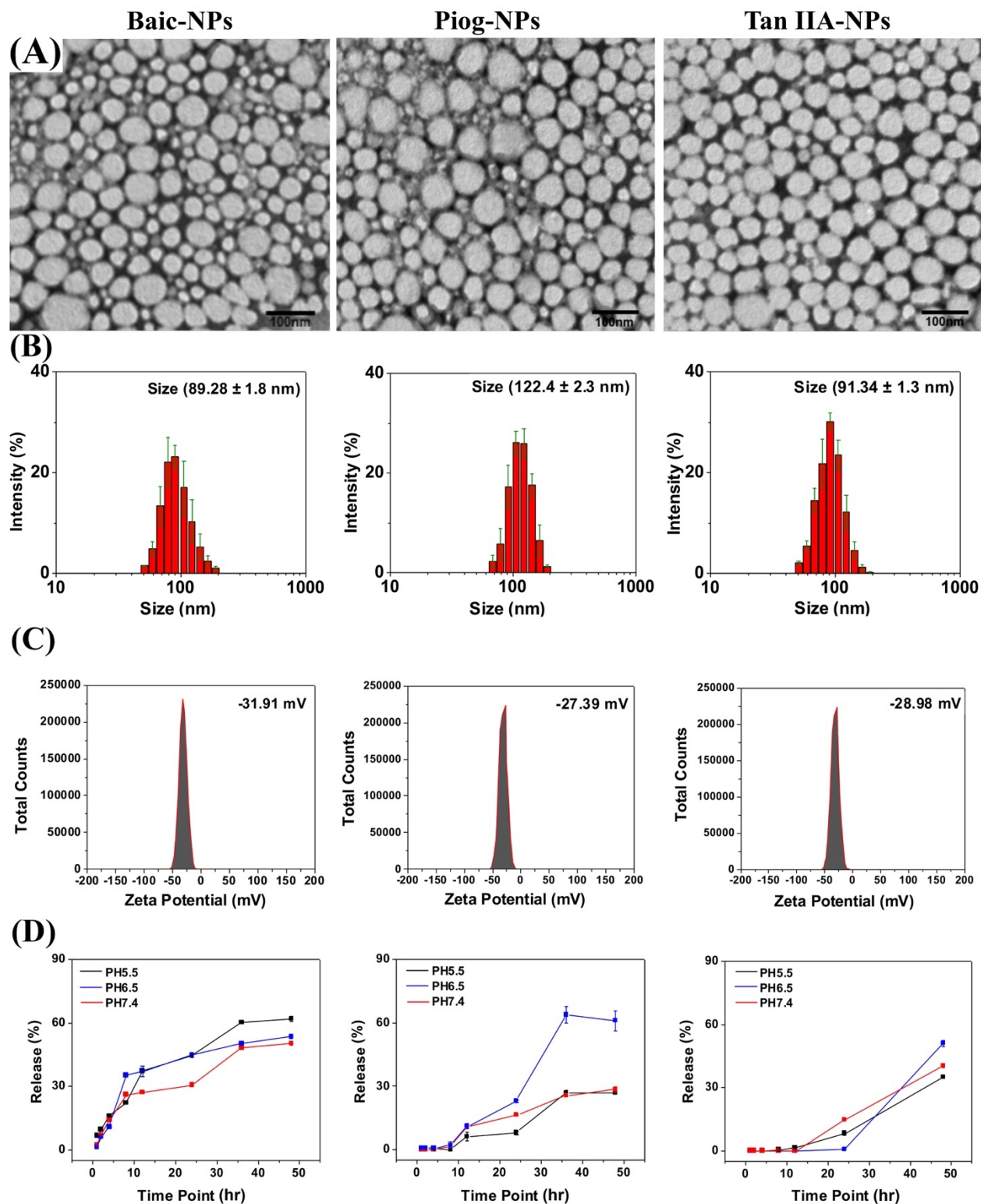


Figure 4.1. Baic, Piog, and Tan IIA are capable of undergoing NP packaging. TEM images of drug loaded PLGA NPs (A). The average NP sizes were 60.8, 74.2, and 52.2 nm for Baic-NPs,

Piog-NPs, Tan IIA-NPs, respectively. Hydrodynamic sizes of NPs were 89.3 ± 1.8 , 122.4 ± 2.3 , and 91.3 ± 1.3 nm for Baic-NPs, Piog-NPs, and Tan IIA-NPs, respectively (B). NPs zeta potentials were -31.91 mV, -27.39 mV, and -28.98 mV for Baic-NPs, Piog-NPs, and Tan IIA-NPs, respectively (C). Drug release profiles for Baic-NPs, Piog-NPs, and Tan IIA-NPs (D).

Tan IIA-NPs and Baic-NPs suppress oxidative stress in NSCs and inflammation in microglia

Tan IIA and Baic have been previously shown to be effective in ischemic stroke animal models at a dose range of 15 mg/kg and 90 mg/kg, respectively ^{277, 278}. Therefore, Tan IIA-NPs, Baic-NPs and corresponding free drugs were tested for cytotoxicity and efficacy in a comparable dose range. MTT assays were performed to determine the relative cytotoxicity of Tan IIA-NPs, Baic-NPs and corresponding free drugs on neural stem cells (NSCs). MTT assays at 24 hours showed reduced viability of the cells at 33 μ M of Tan IIA-NPs and 672 μ M of Baic-NPs (**Figure 4.2A-B**). Notably, while Baic-NPs showed very similar profiles to the Baic free molecules, Tan IIA-NPs showed significantly ($p < 0.05$) less toxicity compared to free Tan IIA 6.6 μ M. This may be attributed to NP-mediated, slow release of Tan IIA at early timepoints.

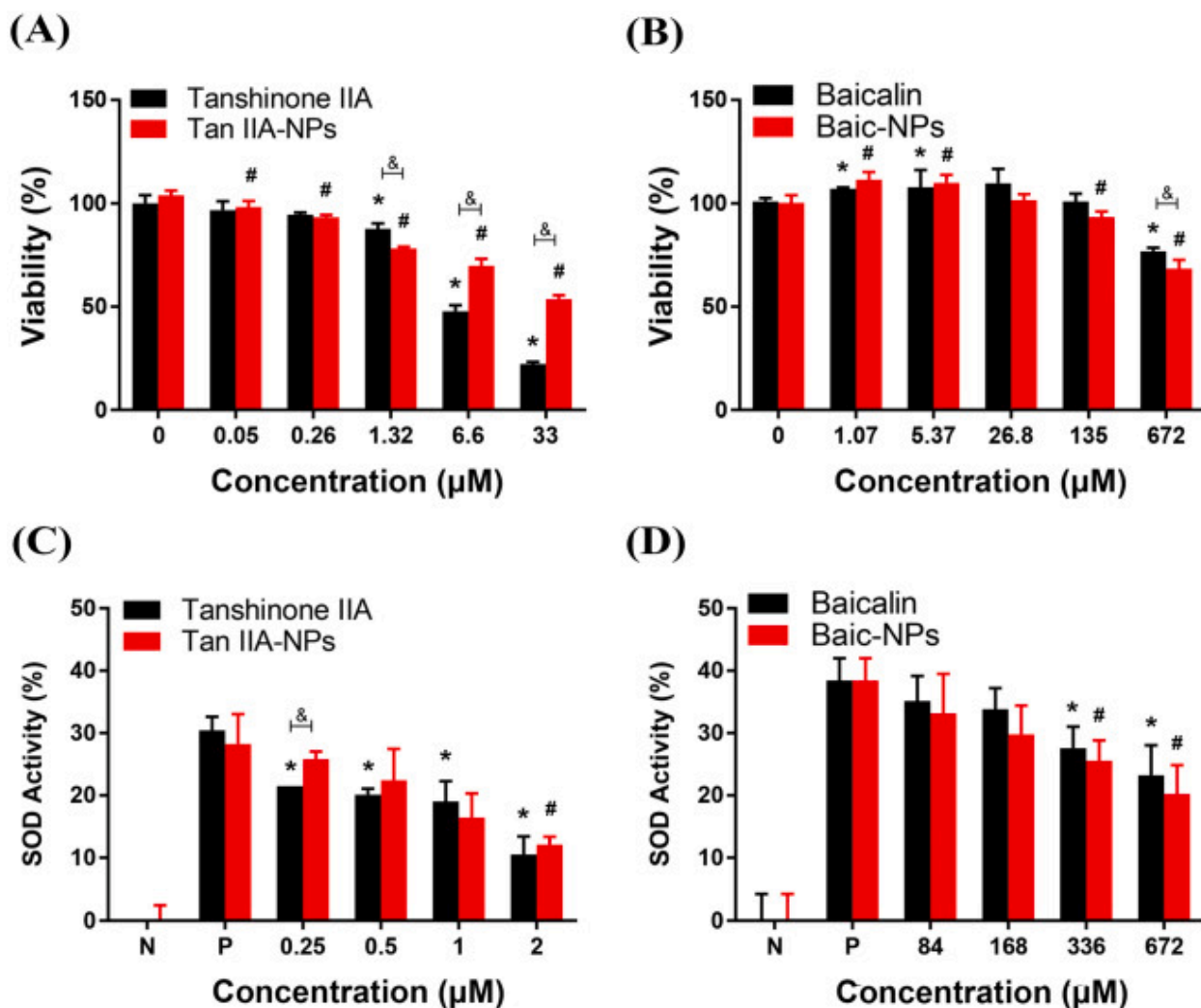


Figure 4.2. Tan IIA-NPs show significantly reduced toxicity in NSCs than freeform drug and Tan IIA-NPs and Baic-NPs reduce oxidative stress in NSCs. MTT assays at 24 h showed reduced viability of the cells at 33 μ M of Tan IIA-NPs and 672 μ M of Baic-NPs (Fig. 2A–B). * or # indicates a significant difference between vehicle only control and treatment. & indicates a significant difference between drug only and drug loaded NP. SOD assay results showed a significant reduction in SOD at 2 μ M and 336 μ M for Tan IIA-NPs (C) and Baic-NPs (D), respectively. * or # indicates a significant difference between positive control and treatment. & indicates a significant difference between drug only and drug loaded NP. (N = negative control, P = positive control).

To study the antioxidative efficacy of Tan IIA-NPs and Baic-NPs, NSCs were treated with H₂O₂ (250 µM) and incubated with drug-loaded NPs and corresponding free drugs. A series of dilutions (determined from respective inhibitory concentration (IC)₂₀ doses) were tested. Oxidative stress was tested by measuring superoxide dismutase (SOD) activity at 24 hours (**Figure 4.2**). Both Tan IIA-NPs and Baic-NPs showed a concentration-dependent reduction of SOD activity, indicating an antioxidative effect (**Figure 4.2C-D**). Tan IIA-NPs resulted in a greater reduction in SOD levels than Baic-NPs at their respective IC₂₀ (2 vs. 672 µM, respectively) and IC_{2.5} (0.25 vs. 84 µM, respectively) doses.

To assess the potential anti-inflammatory effect of Tan IIA-NPs and Baic-NPs, microglia cells were treated with lipopolysaccharide (LPS) and then incubated with drug-loaded NPs and free drugs. The inflammatory response was assessed by measuring TNF-α and IFN-γ. Positive controls treated with LPS showed a significant ($p < 0.05$) increase in TNF-α and IFN-γ levels (128.03±26.21 and 45.92±1.02 pg/ml, respectively). Treatment of microglia with Tan IIA-NPs and Baic-NPs at IC₂₀ and IC_{2.5} doses resulted in undetectable levels of TNF-α and IFN-γ. The absence of TNF-α and IFN-γ after treatment with Tan IIA-NPs and Baic-NPs demonstrates these NPs have an anti-inflammatory response *in vitro* (data not shown). Based on these combined cytotoxicity, oxidative stress, and inflammatory test results, Tan IIA-NPs were selected for further testing in an ischemic stroke pig model.

Tan IIA-NPs reduce hemispheric swelling, consequent MLS, and ischemic lesion volumes post-ischemic stroke

T2Weighted (T2W) sequences collected 24 hours post-stroke revealed Tan IIA-NP treated pigs (**Figure 4.3B**) exhibited a reduced percent change in ipsilateral hemispheric swelling when

compared to PBS controls (**Figure 4.3A**) (7.85 ± 1.41 vs. $16.83 \pm 0.62\%$, respectively; **Figure 4.3C**). This mitigation of hemispheric swelling resulted in a decreased MLS (1.72 ± 0.07 vs. 2.91 ± 0.36 mm; red lines; **Figure 4.3D**). Acute ischemic lesion volumes were also reduced in Tan IIA-NP treated pigs 24 hours post-stroke (9.54 ± 5.06 vs. $12.01 \pm 0.17 \text{ cm}^3$; **Figure 4.3E**), which suggests a reduction in acute tissue injury.

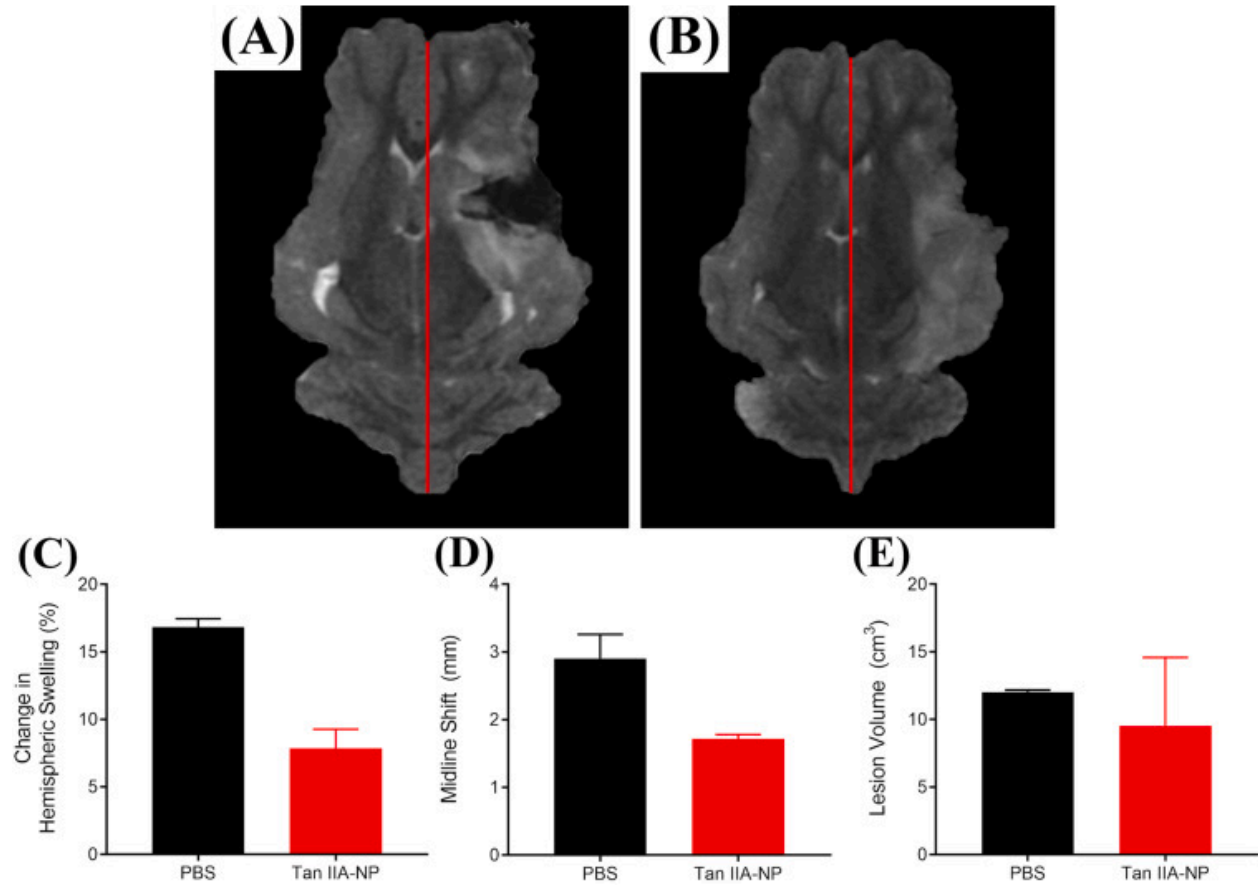


Figure 4.3. Tan IIA-NPs reduce hemispheric swelling, MLS, and ischemic lesion volumes. Compared to PBS pigs ($n = 2$) (A), Tan IIA-NP treated pigs ($n = 2$) (B) exhibited a reduction in ipsilateral hemispheric swelling (7.85 ± 1.41 vs. $16.83 \pm 0.62\%$, respectively; C), MLS (1.72 ± 0.07 vs. 2.91 ± 0.36 mm mm, respectively, red lines; D), and lesion volumes (9.54 ± 5.06 vs. $12.01 \pm 0.17 \text{ cm}^3$, respectively; E) at 24 h post-stroke.

Tan IIA-NP treatment leads to reduced cytotoxic edema, WM damage, and ICH post-ischemic stroke

Hypointense lesioned areas were observed on Apparent Diffusion Coefficient (ADC) maps, which are indicative of restricted diffusion and cytotoxic edema (**Figure 4.4A-B**, white arrows). Tan IIA-NP treated pigs (**Figure 4.4B**) had a reduced percent change in mean ADC values when compared PBS control pigs (**Figure 4.4A**) (-37.30 ± 3.67 vs. $-46.33 \pm 0.73\%$; **Figure 4.4C**). To determine the neuroprotective effect of Tan IIA-NPs on cerebral WM, internal capsule fractional anisotropy (FA) values were evaluated in Tan IIA-NP and PBS treated animals at 24 hours post-stroke. Tan IIA-NP treated animals showed a decreased reduction in FA value relative to PBS treated animals (-19.66 ± 5.58 vs. $-30.11 \pm 1.19\%$; **Figure 4.4D**). T2Star (T2*) sequences showed hypointense acute ICH in PBS and Tan IIA-NP treated pigs 24 hours post-stroke (**Figure 4.5A-B**, respectively). However, Tan IIA-NP treated pigs had smaller hemorrhage volumes compared to PBS treated pigs (0.85 ± 0.15 vs $2.91 \pm 0.84 \text{cm}^3$; **Figure 4.5C**). This data supports that Tan IIA-NPs lead to a reduction in restricted diffusion, cytotoxic edema, WM damage, and ICH in ischemic stroke animals.

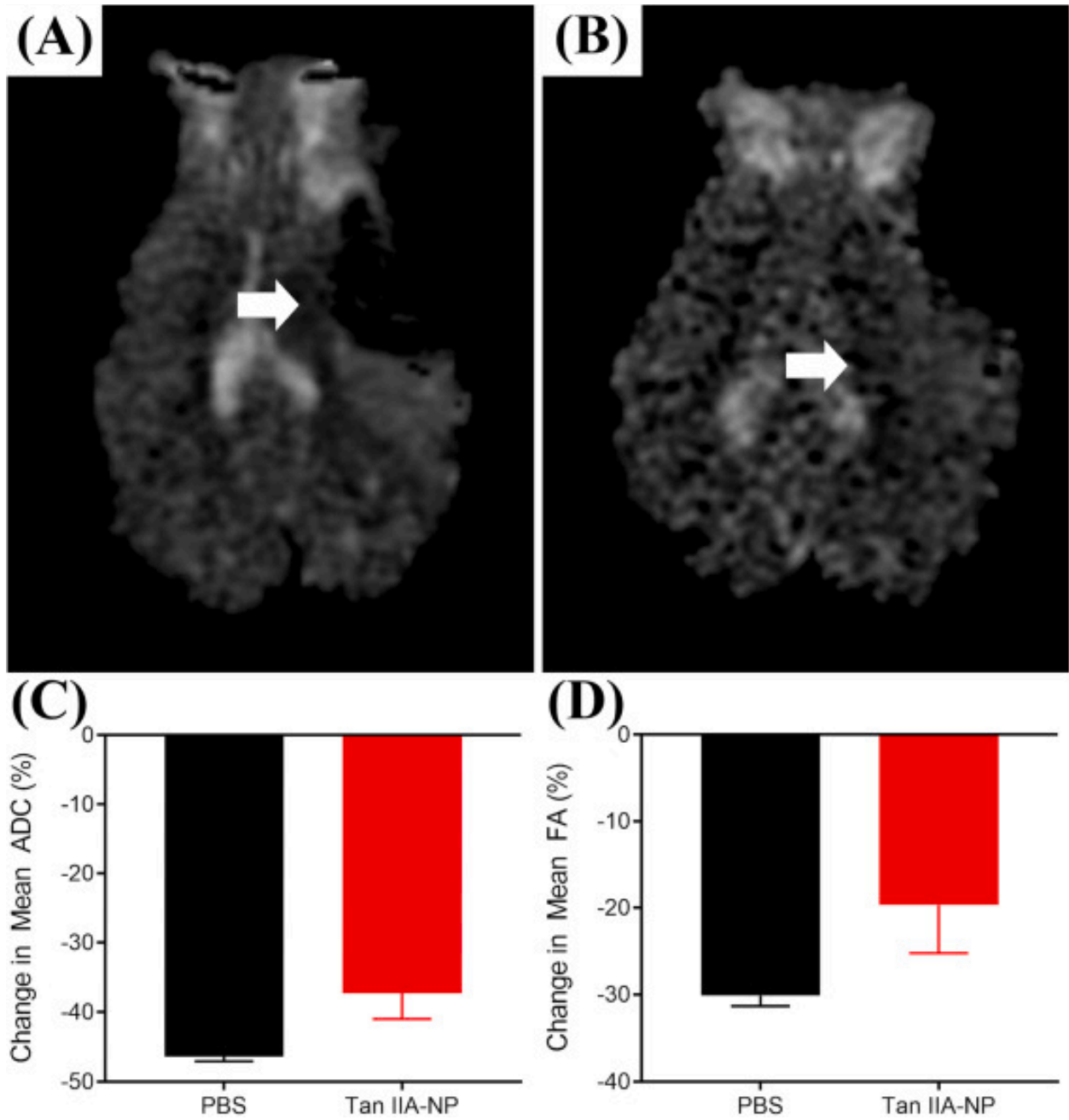


Figure 4.4. Tan IIA-NPs lead to reduced cytotoxic edema and WM damage post-ischemic stroke. Hypointense lesioned areas were observed on ADC maps in PBS (n = 2) (A) and Tan IIA-NP (n = 2) (B) treated pigs. Tan IIA-NP treated pigs had a smaller percent change in mean ADC relative to PBS treated pigs (-37.30 ± 3.67 vs. $-46.33 \pm 0.73\%$, respectively; C). Treated pigs showed a

decreased reduction in FA values relative to PBS treated pigs (-19.66 ± 5.58 vs. $-30.11 \pm 1.19\%$, respectively; D).

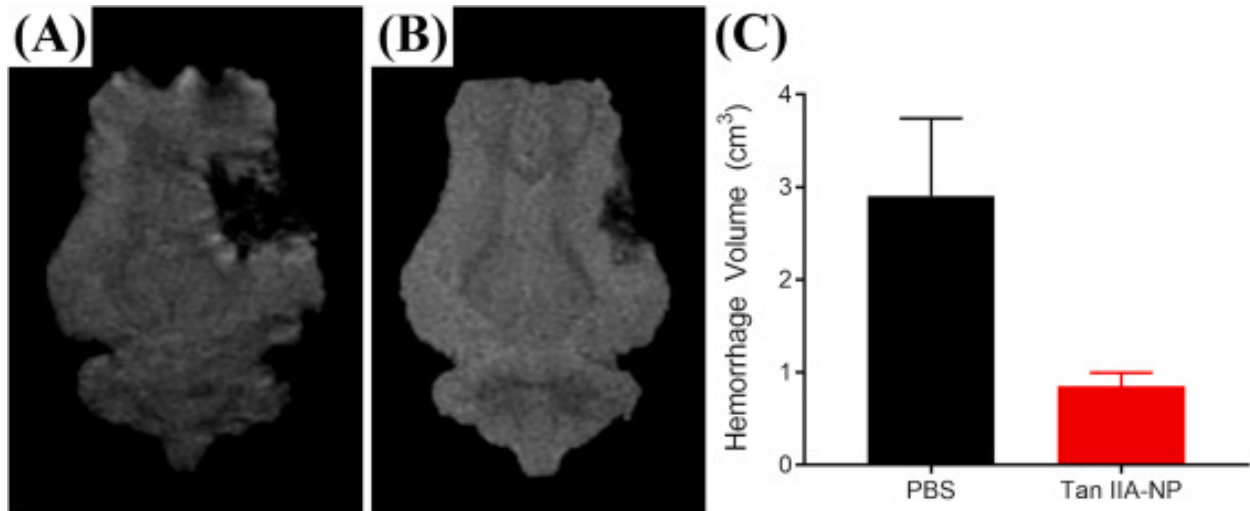


Figure 4.5. Tan IIA-NPs lead to reduced hemorrhage post-ischemic stroke. T2* sequences showed acute ICH in PBS (n = 2) (A) and Tan IIA-NP (n = 2) (B) treated pigs 24 h post-stroke. Tan IIA-NP treated pigs had smaller hemorrhage volumes compared to PBS treated pigs (0.85 ± 0.15 vs 2.91 ± 0.84 cm³, respectively; C).

Tan IIA-NPs reduce circulating band neutrophils in post-stroke pigs

To assess changes in the stroke immune response, band neutrophil and lymphocyte populations were measured in blood samples collected pre-stroke, 4, 12, and 24 hours post-stroke. At 12 hours post-stroke, the percentage of circulating band neutrophils was lower in Tan IIA-NP treated animals than in the PBS control animals at 12 (7.75 ± 1.93 vs. $14.00 \pm 1.73\%$) and 24 (4.25 ± 0.48 vs $5.75 \pm 0.85\%$) post-stroke (**Supplemental Figure 4.1-B**). Conversely, the percentage of circulating lymphocytes was similar in both treatment groups at all assessed time points (**Supplemental Figure 4.1C-D**).

Spatiotemporal and kinetic gait deficits are less severe post-stroke in Tan IIA-NP treated pigs

Changes in key spatiotemporal and kinetic gait parameters were measured to detect differences in functional outcomes post-Tan IIA-NP treatment. A decrease was noted for both treatment groups in the average cadence of the pigs from pre-stroke to post-stroke indicating a decrease in speed. However, the decrease in cadence was more severe for the PBS treated pigs compared to Tan IIA-NP treated pigs (133.9 ± 2.71 to 64.8 ± 5.86 steps/min vs. 135.7 ± 7.08 to 109.98 ± 0.00 steps/min, respectively, **Figure 4.6A**). The limb contralateral to the stroke lesion is often more affected as compared to the ipsilateral limb, which in this study are the limbs of the left side. In addition, pigs typically carry more weight on the forehand, typically making deficits more severe in the left forelimb. Deficits were noted for the left forelimb in both treatment groups for multiple gait parameters. The cycle time of the left front limb increased post-stroke for both treatment groups, with a more drastic increase in cycle time noted for the PBS treatment group as compared to the Tan IIA-NP treated pigs (0.46 ± 0.02 to 0.94 ± 0.08 vs. 0.44 ± 0.02 to 0.55 ± 0.00 sec, respectively, **Figure 4.6B**). Similarly, the left front step time increased post-stroke in both groups, with a greater increased step time in PBS pigs compared to Tan IIA-NP pigs (0.24 ± 0.01 to 0.49 ± 0.07 vs. 0.22 ± 0.01 to 0.27 ± 0.00 sec, respectively, **Figure 4.6C**). Decreases in cycle time and step time indicated an overall slower gait post-stroke, opposed to pre-stroke performance. The swing percent of cycle decreased for the left front limb of all pigs, with PBS pigs decreasing further than Tan IIA-NP pigs (49.4 ± 0.26 to 33.3 ± 1.77 vs. 49.1 ± 1.90 to $43.2 \pm 0.00\%$, respectively, **Figure 4.6D**). A reduction was noted in the left front stride length of all animals, with PBS pigs displaying a greater reduction in stride length relative to Tan IIA-NP pigs (78.38 ± 2.37 to 63.19 ± 3.94 vs. 84.87 ± 1.78 to 77.44 ± 0.00 cm, respectively, **Figure 4.6E**). Finally, the mean pressure of the left front limb decreased in both treatment groups with a larger decrease in pressure noted for the PBS

pigs opposed to the Tan IIA-NP pigs (2.93 ± 0.03 to 2.67 ± 0.03 vs. 2.87 ± 0.03 to 2.88 ± 0.00 arbitrary units (AU), respectively, **Figure 4.6F**). Post-stroke deficits were noted for all parameters in both treatment groups, however more pronounced deficits were seen in the gait of PBS pigs, thus indicating administration of Tan IIA-NP in the acute phase post-stroke leads to less severe gait deficits.

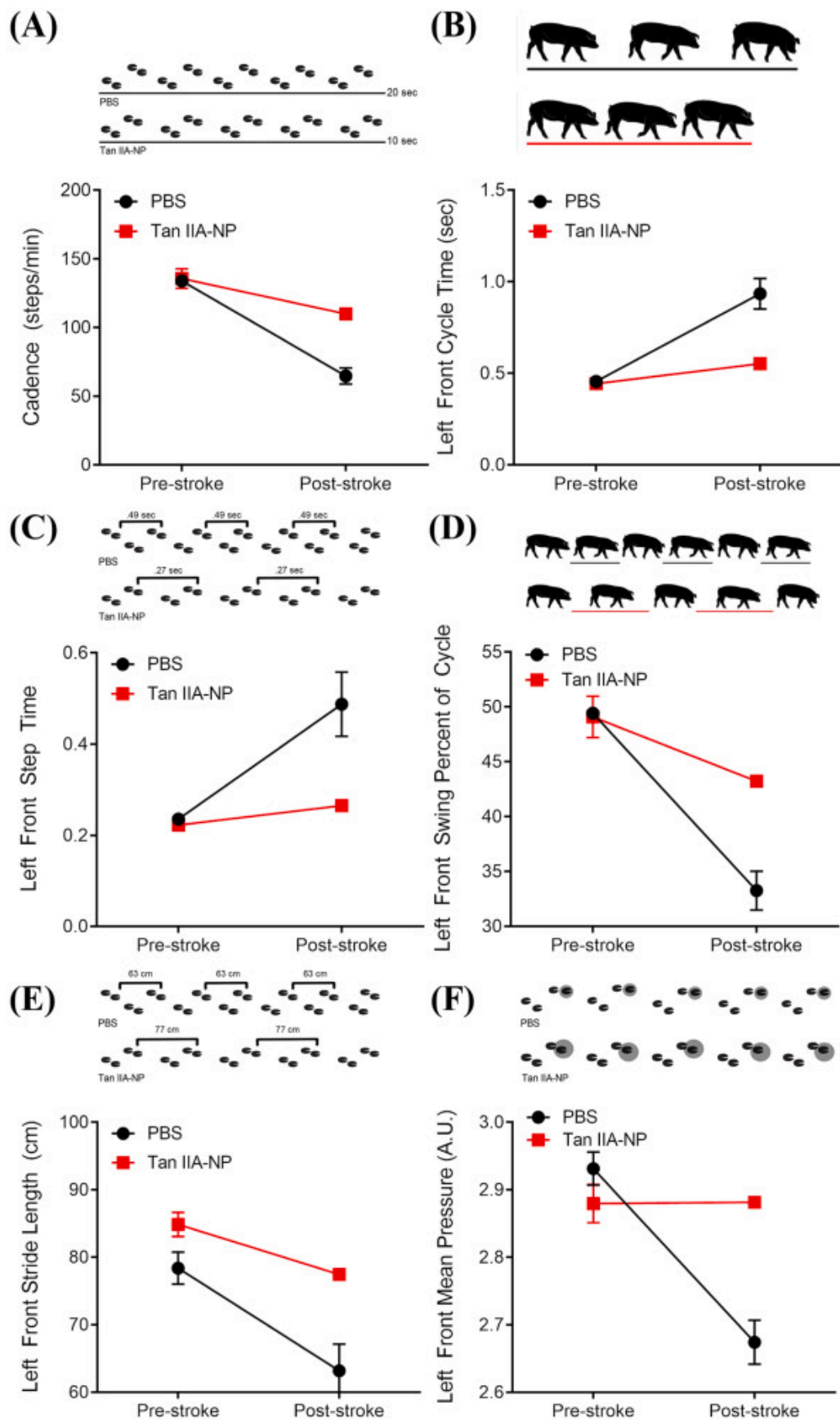


Figure 4.6. Spatiotemporal and kinetic gait deficits are less severe post-stroke in Tan IIA-NP treated pigs. A decrease in the average cadence of the pigs from pre-stroke to post-stroke was more severe in PBS control pigs opposed to Tan IIA-NP treated pigs (133.9 ± 2.71 – 64.8 ± 5.86 steps/min vs. 135.7 ± 7.08 – 109.98 ± 0.00 steps/min, respectively; A). The cycle time of the left front limb increased more drastically in PBS control pigs as compared to Tan IIA-NP treated pigs (0.46 ± 0.02 – 0.94 ± 0.08 vs. 0.44 ± 0.02 – 0.55 ± 0.00 s, respectively; B). The left front step time increased post-stroke in PBS pigs more so than Tan IIA-NP pigs (0.24 ± 0.01 – 0.49 ± 0.07 vs. 0.22 ± 0.01 – 0.27 ± 0.00 s, respectively; C). The swing percent of cycle decreased more for the left front limb of PBS control pigs than Tan IIA-NP pigs (49.4 ± 0.26 – 33.3 ± 1.77 vs. 49.1 ± 1.90 – 43.2 ± 0.00 %, respectively; D). The left front stride length of pigs treated with PBS displaying a greater reduction in stride length relative to Tan IIA-NP pigs (78.38 ± 2.37 – 63.19 ± 3.94 vs. 84.87 ± 1.78 – 77.44 ± 0.00 cm, respectively; E). A larger decrease in mean pressure of the left front limb was noted for PBS control pigs but not Tan IIA-NP treated pigs (2.93 ± 0.03 – 2.67 ± 0.03 vs. 2.87 ± 0.03 – 2.88 ± 0.00 AU, respectively; F).

Discussion

In this study, we demonstrate for the first time Tan IIA-NP treatment leads to improvements in clinically relevant MRI-based stroke tissue injury parameters and functional deficits in a translational ischemic stroke pig model. Tan IIA-NP therapy was selected from a number of drug candidates based on in vitro assessment of biochemical properties that augment NP delivery of a drug and efficacy in antioxidative and anti-inflammatory studies. Tan IIA-NP therapy resulted in considerable reductions in MLS, lesion volumes, WM damage, and ICH in the pig stroke model; parameters that closely correlate with functional deficits and mortality in human

patients²⁷⁹⁻²⁸¹. Tan IIA-NP treatment and associated reduction in overall brain injury corresponded with less severe spatiotemporal and relative pressure gait deficits including parameters that are often affected in human patients including stride length and cadence^{282, 283}. These promising preclinical results in the pig model suggest that Tan IIA-NP therapy is ready for the next step in the STAIR criteria for translating pre-clinical studies into human clinical trials including expanded studies with additional animals of both genders and therapeutic window and dose finding studies.

To improve drug bioavailability, Tan IIA was encapsulated into PLGA-PEG NPs. The nanoplatform allows for controlled release of Tan IIA, potentially leading to prolonged anti-inflammatory and oxidative effects. In addition, Tan IIA-NPs were injected intracisternal into the subarachnoid space rather than IV. This injection route bypasses the BBB that would otherwise prevent the delivery of therapeutics to the ischemic areas. Combining NP delivery and intracisternal administration represents a novel approach in drug delivery. A recent study performed in mice also observed efficient distribution and good tolerance of NPs after intracisternal injection²⁸⁴. Because the entire CNS can be accessed through the CSF, this approach may be extended for the treatment of other CNS diseases.

Infarct volume, cerebral swelling, and consequent MLS have been shown to play a key role in the development of neurological deficits and high patient mortality rates^{244, 280, 281, 285}. In the present study, the acute treatment window of Tan IIA-NPs demonstrated potential in mitigating these clinical presentations by decreasing hemisphere and lesion volumes. In a study of free form Tan IIA, Tang et al. provided evidence that lesion volumes were significantly reduced in 1 and 4 hour post-stroke Tan IIA treatment groups versus 6 and 12 hour Tan IIA treatment groups in their rat study of ischemic stroke²⁵⁶. Additional studies have indicated Tan IIA possesses a neuroprotective effect in cerebral ischemia-reperfusion rodent models, whereby encephaledema

and hemispheric swelling were relieved, infarction volumes decreased, and neurobehavior scores were significantly improved ^{286, 287}.

Measures of ICH and ADC and are also strong predictors of clinical outcomes with increased hemorrhage and decreased ADC values being closely associated with poor clinical outcomes and higher mortality rates ^{288, 289}. In the current study, Tan IIA-NP treated animals showed a decreased hemorrhage volume and a decreased percent change in ADC values relative to PBS treated animals. A recent study in a middle cerebral artery occlusion (MCAO) ischemic stroke mouse model showed that free form Tan IIA has a protective effect on the BBB, which would result in reduced hemorrhage ²⁸⁷. This study demonstrated increased presence of the tight junction protein claudin-5 and reduced BBB leakage in Tan IIA treated animals. In a study assessing the ability of Tan IIA to maintain vascular integrity in a rat aneurysm model, researchers demonstrated Tan IIA reduced aneurysm size and increased vascular wall thickness improving vascular integrity relative to control animals ²⁹⁰. Zhou et al. showed in an ICH zebrafish model, Tan IIA reduced ICH area and incidence ²⁹¹. In a follow-up in vitro study with human umbilical vein endothelial cells, they demonstrated that Tan IIA inhibits actin depolymerization near cell borders and cell contraction, which would result in destabilization of cell-cell adheren junctions critical to maintaining the BBB. These results in multiple unique disease models across three different species demonstrates Tan IIA leads to increased stability in intracerebral vasculature that would result in reduced ICH as observed in this study. Preservation of diffusivity observed in this study is likely a direct result of decreased injury due to acute Tan IIA-NP treatment. This corresponds with previous Tan IIA studies in rodent models showing improved cerebral blood flow, reduced free radical formation, inflammation, and a decrease in infarcted brain tissue ^{243, 256}.

Gait deficits constitute a significant portion of disabilities related to stroke. Unsurprisingly, many patients report improvement in mobility as a main goal for post-stroke recovery, making this an important benchmark for stroke therapeutic treatment potential ²⁹². Human stroke patients are often left with hemiparesis resulting in gait deficits including decreased cadence and stride length with associated increased swing percent of cycle and cycle time ²⁸³. Similarly, pigs in the current study exhibited a post-stroke decrease in stride length and cadence with an associated increase in cycle time and step time in the left forelimb. These alterations in gait patterns mirror what is seen in humans and are likely reflective of the decreased velocity that typically accompanies postural instability following stroke. Further, pigs in the current study showed decreased swing percent of cycle of the affected contralateral forelimb post-stroke. While this is opposite of what is often seen in human stroke patients, a decrease in relative swing and increase in relative stance has been reported as a hallmark gait change in pig models for both stroke and traumatic brain injury and is likely due to an increased need for ground contact to stabilize the gait along with decreased propulsion ²⁹³⁻²⁹⁵. In the present study, changes in spatiotemporal gait properties were noted in all pigs in the acute time frame following stroke, however a more pronounced deficit was noted in the gait of PBS pigs as compared to Tan IIA-NP pigs post-stroke. Additionally, PBS pigs in this study also showed a reduction in mean hoof pressure of the contralateral forelimb, indicating compensatory balance mechanisms to distribute weight away from the affected contralateral side, while Tan IIA-NP pigs showed no kinetic changes. Several studies have demonstrated Tan IIA administration in rodent stroke models led to a reduction in severity of functional neurologic deficits (determined by factors such as failure to extend the forepaw of the contralateral limb, circling, lack of balance, or inability to walk) as compared to control animals ^{243, 296}. The results of the present study are in agreement with these rodent models and suggest the administration of

Tan IIA-NPs in the acute phase post-stroke mitigates cerebral injury and thereby results in less severe functional deficits.

Conclusion

This proof of concept study demonstrated Tan IIA-NPs have notable potential to be a novel treatment for ischemic stroke. Utilizing a highly translatable pig model of ischemic stroke, Tan IIA-NP treatment leads to reduced hemispheric swelling, MLS, lesion volumes, cytotoxic edema, WM damage, and ICH 24 hours post-stroke. These manifested improvements in acute ischemic stroke pathophysiology led to marked improvements in a number of spatiotemporal and kinetic gait parameters. These promising results support the idea Tan IIA-NPs are ready for further preclinical studies assessing safety and efficacy in a larger cohort of animals in both sexes in order to evaluate dosing and administration windows in accordance with the STAIR criteria for therapeutic translation to clinical trials.

Materials and methods

The overarching aim of this study was to characterize and evaluate Tan IIA-NPs and their efficacy as a potential acute stroke therapy in a clinically relevant pig model of ischemic stroke. Tan IIA-NPs were synthesized and characterized. Ischemic stroke was induced, and Tan IIA-NPs were delivered intracisternally as single dose 1 hour post-stroke induction. MRI was performed 24 hours post-stroke. Venous blood was collected pre-stroke, 4, 12, and 24 hours post-stroke. Gait analysis was performed pre and 48 hours post-stroke. Only two animals were included in each treatment group for a total of 4 animals for in vivo studies, therefore statistical analysis was limited to in vitro studies.

Synthesis of PLGA-b-PEG-OH

PLGA acid (PLGA-COOH; 1.0 g, 0.170 mmol, Mn = 7,000; Lactel), polyethylene glycol (HO-PEG-OH; 2.29 g, 0.684 mmol, Mn = 2,000; Sigma Aldrich), and deoxyadenosine monophosphate (dMAP; 0.023 g, 0.187 mmol; Alfa Aesar) were dissolved in 30 mL of anhydrous dichloromethane (CH_2Cl_2 ; Sigma Aldrich). Next, a 10 mL CH_2Cl_2 solution of dicyclohexylmethanediimine (DCC; 0.141 g or 0.684 mmol; Sigma Aldrich) was added dropwise to the reaction mixture at 0 °C with magnetic stirring. The mixture was warmed up to room temperature and stirred overnight. Insoluble dicyclohexylurea ($\text{C}_{13}\text{H}_{24}\text{N}_2\text{O}$) was filtered out. The raw product was precipitated out by adding 50 mL of 50:50 diethyl ether ($(\text{C}_2\text{H}_5)_2\text{O}$; Sigma Aldrich) and methanol (CH_3OH ; Sigma Aldrich) to the mixture. The mixture was centrifuged for 15 minutes at 4 °C. The purification step was repeated 4-5 times, followed by ^1H NMR analysis that was performed on a Varian Mercury Plus 400 system.

NP synthesis

PLGA NPs were synthesized through a nanoprecipitation method. Briefly, poly (lactide-co-glycolide)-b-poly (ethylene glycol)-maleimide (PLGA-b-PEG-OH) was first dissolved in dimethylformamide (DMF) at a concentration of 50 mg/mL. 100 μL of the polymer solution was mixed with drug-to-be-loaded (150 μL , 0.15 mg; Tan IIA, TCI America; Piog, Sigma Aldrich; Baic, Sigma Aldrich; Puer, Sigma Aldrich; Edar, Sigma Aldrich; Resv, Sigma Aldrich) for 30 % feeding and diluted with DMF (Fisher Scientific) to a final polymer concentration of 5 mg/mL. The mixture was added dropwise to sterile nanopure water with constant stirring, and the resulting solution was agitated in a fume hood for 2 hours. Drug loaded NPs were collected on an amicon ultracentrifugation unit (100 kDa cut-off) and were washed 3-4 times with water. Finally, the NPs were resuspended in sterilized nanopure water.

NP characterizations

A drop of diluted NP solution was deposited onto a transmission electron microscopy (TEM) grid, followed by staining with 2% uranyl acetate. TEM images were taken on a FEI Tecnai 20 transmission electron microscope operating at an accelerating voltage of 200 kV. Hydrodynamic size and surface charge of NPs were analyzed on a Malvern Zetasizer Nano ZS system.

Drug loading and release

For drug loading analysis, a 50 μ L aqueous solution of NPs was diluted to 900 μ L and 100 μ L 0.1 mM sodium hydroxide (NaOH; Sigma Adrich) was added to the solution. The mixture was incubated at room temperature overnight. Next, the solution was sonicated for 30 minutes and centrifugated at 5000 rpm for 10 minutes. 100 μ L supernatant was transferred into a 96-well UV transparent plate and its absorbance at the relevant wavelength was measured (Tan IIA: 258 nm; Baic: 320 nm; Piog: 270 nm). To test drug release, 100 μ L NP solution was loaded onto a dialysis unit and allowed to float on a 1.1 mL PBS solution (pH: 5.5, 6.5, or 7.4; Gibco). The system was put on an Eppendorf shaker set at 37 °C. At each time point (0.5, 1, 2, 4, 8, 12, 24, 36, and 48 hours), 100 μ L PBS solution was transferred to a 96-well UV transparent plate. The drug content was assessed by measuring the relevant absorbance (Tan IIA: 258 nm; Baic: 320 nm; Piog: 270 nm) and compared to a standard curve. 100 μ L of fresh PBS solution was added back to the dialysis system.

Cell culture

Neural stem cells (NSCs; HIP™ hNSC BC1, GlobalStem) were maintained on Matrigel-coated (Corning) tissue culture treated plates in NSC media composed of Neurobasal medium (Gibco), 2% B-27 Supplement (Gibco), 1% non-essential amino acids (Gibco) 2 mM L-glutamine

(Gibco), 1% penicillin/streptomycin (Gibco), 20 ng/mL basic fibroblast growth factor (bFGF; R&D Systems). NSCs were incubated at 37 °C with 5% CO₂ and a complete media change was performed every other day. When NSCs reached confluence, cells were enzymatically passaged using Accutase (Gibco).

Microglia cells (ATCC) were maintained on tissue culture treated plates in microglia media composed of Eagle's Minimum Essential Medium (ATCC), 11% fetal bovine serum (ATCC) 1% penicillin/streptomycin (Gibco). Microglia were incubated at 37 °C with 5% CO₂ and a complete media change was performed every other day. When microglia reached confluence, cells were enzymatically passaged using 0.05% trypsin (Gibco).

MTT assay

The MTT assay was performed according to the manufacturer's protocol (Sigma Aldrich). Briefly, 8x10³ NSCs were seeded into each well of a 96 well plate. After 8 hours of incubation at 37 °C in a humidified atmosphere with 5% CO₂, a gradient of the tested drugs or NPs were added into the wells. After 24 hours of incubation, the medium was removed, and cells were washed. 10 µL MTT solution (10 mg/mL) was added into each well and incubated with cells for 4 hours. The absorbance at 570 nm was measured on a plate reader. Viability was calculated by computing relative absorbance with regard to PBS treated cells.

SOD activity assay

The SOD activity assay was performed according to the manufacturer's protocol (Cayman). Briefly, 1×10⁶ NSCs were seeded into each well of a 6-well plate. After 24 hours, the cells were incubated with 250 µM hydrogen peroxide (H₂O₂) to induce oxidative stress. After 30 minutes, the cells were washed with PBS and then incubated with drugs or drug-containing NPs at different concentrations for 24 hours. The cells were then detached from plate using a cell scraper, collected

by centrifugation, and washed 3 times with PBS. The resultant cells were homogenized by sonication and then centrifuged at 3600 rpm at 4 °C for 10 minutes. The supernatant was immediately collected and diluted with assay buffers by 4 times the supernatant amount. The diluted solutions were transferred into a 96-well plate at a volume of 200 μ L per well. 20 μ L of diluted xanthine oxidase was added into the solution and the plate was covered with foil and shaken at room temperature for 30 minutes. The absorbance at 450 nm was then read on a plate reader. The SOD activity was calculated as μ /mL of protein by comparing to SOD standards.

ELISA assays

Anti-inflammatory efficacy was tested by TNF- α and IFN- γ enzyme-linked immunosorbent assay (ELISA) assays according to the manufacturer's protocol (Invitrogen). Briefly, 2×10^4 microglia cells in microglia media were seeded in 12 well plates overnight. To induce an inflammatory response in microglia cells, 150 ng/mL LPS was added in each well and incubated at 37 °C with 5% CO₂. After 24 hours, cells were washed with PBS 2 times and then incubated with either drugs or at each respective drugs IC 20, IC 6.7, IC 2.2, IC 0.74, IC 0.25 or 0 based on the previously performed MTT assay and 150 ng/mL LP S. Negative control samples were not treated with LPS or drug. After 24 hours, supernatant was collected from each well, processed and absorbance was read at 450nm. Cytokine values were calculated as pg/mL.

Animals and housing

All work performed in this study was approved by the University of Georgia (UGA) Institutional Animal Care and Use Committee (IACUC; Protocol Number: 2017-07-019Y1A0) and in accordance with the National Institutes of Health Guide for the Care and Use of Laboratory Animals guidelines to ensure appropriate and humane use of animals. Sexually mature, castrated male Landrace pigs, 5-6 months old and 48-56 kg were enrolled in this study. Male pigs were used

in accordance with the STAIR guidelines that suggests initial therapeutic evaluations should be performed with young, healthy male animals ²⁹⁷. Pigs were individually housed at a room temperature approximately 27 °C with a 12-hour light/dark cycle. All pigs were fed standard grower diets.

MCAO and NP delivery

One day prior to surgery, antibiotics and pain medication were administered (Excede; 5 mg/kg intramuscular (IM) and fentanyl patch; 100 mg/kg/hr transdermal (TD)). Pre-induction analgesia and sedation were achieved using xylazine (2 mg/kg IM) and midazolam (0.2 mg/kg IM). Anesthesia was induced with IV propofol to effect and prophylactic lidocaine (1.0 mL 2% lidocaine) topically to the laryngeal folds to facilitate intubation. Anesthesia was maintained with isoflurane (Abbott Laboratories) in oxygen.

As previously described, a curvilinear skin incision extended from the right orbit to an area rostral to the auricle ²⁹⁸. A segment of the zygomatic arch was resected while the temporal fascia and muscle were elevated and a craniectomy was performed exposing the local dura mater. Following a local durectomy, the distal middle cerebral artery (MCA) and associated branches were permanently occluded using bipolar cautery forceps resulting in ischemic infarction. The temporalis muscle and epidermis were routinely re-apposed.

At 1 hour post-stroke, PBS (n=2) or Tan IIA-NPs (n=2) (total animals =4) were intracisternally delivered via a 20 gauge, 3.5 or 6” spinal needle inserted through the skin on the midline of the dorsal neck, at an anatomical intersection of a vertical line created by the rostral aspect of the wings of the first vertebral body and a horizontal line connecting the dorsal arch of C2 with the occipital protuberance. Once the needle was through the cutaneous tissues, the stylet was removed and advanced until CSF appeared in the needle hub confirming entry into the cistern.

A small volume (3-5 mLs) of CSF was removed while the spinal needle was in place and the volume removed was replaced with PBS or Tan IIA-NPs. The volume of NPs delivered was determined by the NP encapsulation efficiency and each animal received a dose of 133 μ g/kg Tan IIA.

Anesthesia was discontinued, pigs were returned to their pens upon extubation, and monitored every 15 minutes until vitals including temperature, heart rate, and respiratory rate returned to normal. Monitoring was reduced to every 4 hours for 24 hours, and then twice a day thereafter until post-transplantation sutures were removed. Banamine (2.2 mg/kg IM) was administered for post-operative pain and fever management every 12 hours for the first 24 hours post-stroke and then every 24 hours for 3 days.

MRI acquisition and analysis

MRI was performed 24 hours post-stroke on a General Electric 3.0 Tesla MRI system. Pigs were sedated and maintained under anesthesia as previously described for MCA occlusion surgery. MRI of the cranium was performed using an 8-channel torso coil with pigs positioned in supine recumbency. Multiplanar MRI sequences were acquired including T2 Fluid Attenuated Inversion Recovery (T2FLAIR), T2W, T2*, Diffusion Weighted Imaging (DWI), and Diffusion Tensor Imaging (DTI). Sequences were analyzed using Osirix software (Version 5.6). Cytotoxic edema consistent with ischemic stroke was confirmed 24 hours post-stroke by comparing hyperintense regions in T2FLAIR and DWI sequences to corresponding hypointense regions in DWI generated ADC maps.

Hemisphere volume was calculated using T2W sequences for each axial slice by manually outlining the ipsilateral and contralateral hemispheres, while excluding the ventricles. The hemisphere areas were multiplied by the T2W slice thickness (3 mm) to obtain total hemisphere

volumes. Lesion volume was calculated using DWI sequences for each axial slice by manually outlining hyperintense regions of interest (ROI). The area of each ROI was multiplied by the DWI slice thickness (2 mm) to obtain the total lesion volume. ADC values were calculated for each axial slice based on hypointense ROI and directly compared to identical ROI in the contralateral hemisphere. DTI was utilized to generate FA maps. FA values of the internal capsules were manually calculated on the slice where the internal capsules and the splenium of the corpus callosum were visualized. FA values were expressed as a percent change in the ipsilateral hemisphere relative to the contralateral hemisphere. ICH volume was calculated based on hypointense ROIs in T2* sequences and multiplied by the slice thickness (2 mm).

Blood collection and analysis

Venous blood samples were collected pre-stroke, 4 hours, 12 hours, and 24 hours post-stroke into K2EDTA spray coated tubes (Patterson Veterinary). Samples were stored at room temperature for 30 minutes. 4 μ L of blood was then pipetted onto a ColorFrost microscope slide (ThermoScientific) approximately 1 cm from the bottom. A spreader slide was placed in front of the blood at a 45° angle and retracted while maintaining even pressure until the blood sample spread evenly along the width of the slide. Care was taken to ensure each blood smear covered approximately two-thirds of the slide and exhibited an oval feathered end. Each slide was air-dried for 10 minutes and fixed with methanol for 2 minutes. Once dry, the slide was stained with Rowmanosky stain for 5 minutes. The stained slide was then submerged in double-distilled water (ddH₂O) for 10 minutes. Finally, the slide was rinsed and allowed to air dry prior to applying a cover slip. Trained, blinded personnel completed manual cell counts of lymphocytes and band neutrophils at the monolayer, beginning approximately 1 mm away from the body of the smear. The first 100 cells visualized were identified and cell counts were expressed as a percentage.

Gait Analysis

Pre- and post-stroke, all pigs underwent gait analysis to measure differences in spatiotemporal and relative pressure gait parameters between treatment groups. 2 weeks prior to stroke induction, all pigs were trained to travel across a gait mat at a consistent, two-beat pace. Pigs received food rewards at each end of the mat for each successful run in which the pig was not distracted and moved at a consistent pace. For each pig, pre-stroke data was collected on 3 separate days. At each time point, pigs moved across the mat until 5 consistent repetitions were achieved, with no more than 15 total repetitions collected.

All data was automatically captured using a GAITFour[®] electronic, pressure-sensitive mat (CIR Systems Inc., Franklin, NJ) that is 7.01 m in length and 0.85 m in width with an active area that is 6.10 m in length and 0.61 m in width. In this arrangement, the active area is a grid, 48 sensors wide by 480 sensors long, totaling 23,040 sensors. Gait data was then semi-automatically analyzed using the GAITFour[®] Software. All resulting data was analyzed for cadence (steps/min). Further measurements were quantified for the left forelimb, contralateral to the stroke lesion. These measurements included stride length (distance between successive ground contact of the left forelimb), swing percent of cycle (percent of a full gait cycle in which the left forelimb is not in contact with the ground), cycle time (amount of time for a full stride cycle), and mean pressure (amount of pressure exerted by the left forelimb).

Statistical analysis

All quantitative data was analyzed with SAS (Version 9.3; Cary, NC) and statistical significances between groups were determined by one-way analysis of variance (ANOVA) and post-hoc Tukey-Kramer Pair-Wise comparisons. Treatments where p-values ≤ 0.05 were

considered significantly different. Only two animals were included in each treatment group for a total of 4 animals for in vivo studies, therefore statistical analysis was limited to in vitro studies.

CHAPTER 5

CONCLUSTIONS AND FUTURE WORK

PDT is an effective modality against tumor, by direct destruction on cancer cells, tumor vascular damage, and activation of immune system. ICD induced by PDT involves in the recruitment of innate immune cells and consequently adaptive immune system, stimulating specific antitumor immune responses. However, tumors have the capability to develop immunosuppressive TME via several mechanisms, such as PD-1/PD-L1, CTLA-4, IDO, etc., which cannot be overcome solely by the PDT-induced immune responses. Cancer immunotherapy is a recently discovered anti-cancer treatment, which aims to train immune cells to thwart immunosuppressive TME and consequently achieve great tumor eliminating effect. IDO is an immunosuppressive enzyme that catabolizes tryptophan to kynurenine and also assists to recruit immunosuppressive immune cells into tumor to build up its unique regulatory mechanisms.

Therefore, with the assistance of IDO inhibition, therapeutic effect of PDT can be largely boosted, owing to the augmented immune response toward tumor. For example, we developed nanoconjugate, PPF NP, that consists of two nanocomponents to achieve synergized therapeutic effect, PLGA-PEG nanoparticles as the core to deliver NLG919, while ZnF₁₆Pc loaded ferritin as satellites for PDT. Compared to PDT monotherapy, PPF NPs enabled improved tumor management, showing prolonged tumor inhibition control in all treated mice, complete tumor elimination effect in 30 % treated mice, and also success in against live cancer cells challenge.

Except the involvement in cancer treatments, nanomedicines can also be applied in anti-inflammatory therapies, either as carrier to deliver anti-inflammatory agents to lesion or itself to

against inflammation. For instance, we developed dopamine melanin nanoparticles (DM NPs) to scavenge ROS and RNS for osteoarthritis treatment. Unlike small molecules, DM NPs, with the size of ~110 nm, offers longer retention time in the joint, which can benefit to scavenge radicals for sustained radical suppression. Also, owing to the remarkable properties of nanocarrier, hydrophobic anti-inflammatory agents have the chance to effectively reach to the lesion and receive improved clinical evaluation by encapsulating into nanocarriers. Tanshinone IIA, an effective anti-inflammatory drug, tends to aggregate together under aqueous solution, which lower its administration effectiveness, bioavailability, and may cause side effects. Owing to the hydrophilicity bestowed by PLGA-PEG nanoparticles, Tanshinone IIA became more stable under bioenvironment with enhanced bioavailability and achieved great anti-inflammatory effect in pigs with ischemic stroke.

In the future, I will continue to explore the potential of nanoparticles in combination therapies for augmented PDT therapeutic effect against tumor. In current study, PPF NPs were intratumorally administrated to evaluate their anti-tumor capability. In the future, I will explore how PPF NPs performs in tumor management via systemically administration for not only melanoma, but also prostate cancer, non-small-lung cancer, and other cancer types. Also, I will investigate whether the employment of PD-1/PD-L1, CTLA-4 or other immunosuppressive pathways can improve PDT outcome, which will also be evaluated by intravenous injection.

REFERENCE

1. Daniell, M. D.; Hill, J. S., A history of photodynamic therapy. *Aust N Z J Surg* **1991**, *61* (5), 340-348.
2. Kessel, D., Photodynamic Therapy: A Brief History. *J Clin Med* **2019**, *8* (10), 1581.
3. Dolmans, D. E.; Fukumura, D.; Jain, R. K., Photodynamic therapy for cancer. *Nat Rev Cancer* **2003**, *3* (5), 380-387.
4. Lucky, S. S.; Soo, K. C.; Zhang, Y., Nanoparticles in Photodynamic Therapy. *Chem Rev* **2015**, *115* (4), 1990-2042.
5. Castano, A. P.; Demidova, T. N.; Hamblin, M. R., Mechanisms in photodynamic therapy: part one-photosensitizers, photochemistry and cellular localization. *Photodiagnosis Photodyn Ther* **2004**, *1* (4), 279-293.
6. Kwiatkowski, S.; Knap, B.; Przystupski, D.; Saczko, J.; Kedzierska, E.; Knap-Czop, K.; Kotlinska, J.; Michel, O.; Kotowski, K.; Kulbacka, J., Photodynamic therapy - mechanisms, photosensitizers and combinations. *Biomed Pharmacother* **2018**, *106*, 1098-1107.
7. Castano, A. P.; Mroz, P.; Hamblin, M. R., Photodynamic therapy and anti-tumour immunity. *Nat Rev Cancer* **2006**, *6* (7), 535-545.
8. Van Straten, D.; Mashayekhi, V.; De Bruijn, H.S.; Oliveira, S.; Robinson, D.J. Oncologic photodynamic therapy: basic principles, current clinical status and future directions. *Cancers* **2017**, *9* (2), 19.
9. Kou, J.; Dou, D.; Yang, L., Porphyrin photosensitizers in photodynamic therapy and its applications. *Oncotarget* **2017**, *8* (46), 81591-81603.

10. Baskaran, R.; Lee, J.; Yang, S. G., Clinical development of photodynamic agents and therapeutic applications. *Biomater Res* **2018**, 22, 25.
11. O'Connor, A. E.; Gallagher, W. M.; Byrne, A. T., Porphyrin and nonporphyrin photosensitizers in oncology: preclinical and clinical advances in photodynamic therapy. *Photochem Photobiol* **2009**, 85 (5), 1053-1074.
12. Ormond, A. B.; Freeman, H. S., Dye Sensitizers for Photodynamic Therapy. *Materials (Basel)* **2013**, 6 (3), 817-840.
13. Josefsen, L. B.; Boyle, R. W., Photodynamic therapy: novel third-generation photosensitizers one step closer? *Br J Pharmacol* **2008**, 154 (1), 1-3.
14. Runnels, J. M.; Chen, N.; Ortel, B.; Kato, D.; Hasan, T., BPD-MA-mediated photosensitization in vitro and in vivo: cellular adhesion and beta1 integrin expression in ovarian cancer cells. *Br J Cancer* **1999**, 80 (7), 946-953.
15. Song, L. M. W. K.; Wang, K. K.; Zinsmeister, A. R., Mono-L-aspartyl chlorin e6 (NPe6) and hematoporphyrin derivative (HpD) in photodynamic therapy administered to a human cholangiocarcinoma model. *Cancer* **1998**, 82 (2), 421-427.
16. Wolf, P.; Rieger, E.; Kerl, H., Topical Photodynamic Therapy with Endogenous Porphyrins after Application of 5-Aminolevulinic Acid: An alternative treatment modality for solar keratoses, superficial squamous cell carcinomas, and basal carcinomas? *J Am Acad Dermatol* **1993**, 28 (1), 17-21.
17. Lo, P. C.; Rodriguez-Morgade, M. S.; Pandey, R. K.; Ng, D. K. P.; Torres, T.; Dumoulin, F., The unique features and promises of phthalocyanines as advanced photosensitisers for photodynamic therapy of cancer. *Chem Soc Rev* **2020**, 49 (4), 1041-1056.
18. Chang, J. E.; Liu, Y.; Lee, T. H.; Lee, W. K.; Yoon, I.; Kim, K., Tumor Size-Dependent

- Anticancer Efficacy of Chlorin Derivatives for Photodynamic Therapy. *Int J Mol Sci* **2018**, *19* (6), 1596.
19. Huang, L.; Huang, Y. Y.; Mroz, P.; Tegos, G. P.; Zhiyentayev, T.; Sharma, S. K.; Lu, Z.; Balasubramanian, T.; Krayner, M.; Ruzie, C.; Yang, E.; Kee, H. L.; Kirmaier, C.; Diers, J. R.; Bocian, D. F.; Holten, D.; Lindsey, J. S.; Hamblin, M. R., Stable Synthetic Cationic Bacteriochlorins as Selective Antimicrobial Photosensitizers. *Antimicrob Agents Ch* **2010**, *54* (9), 3834-3841.
 20. Kofler, B.; Romani, A.; Pritz, C.; Steinbichler, T. B.; Schartinger, V. H.; Riechelmann, H.; Dudas, J., Photodynamic Effect of Methylene Blue and Low Level Laser Radiation in Head and Neck Squamous Cell Carcinoma Cell Lines. *Int J Mol Sci* **2018**, *19* (4), 1107.
 21. Sharma, M.; Visai, L.; Bragheri, F.; Cristiani, I.; Gupta, P. K.; Speziale, P., Toluidine blue-mediated photodynamic effects on staphylococcal biofilms. *Antimicrob Agents Ch* **2008**, *52* (1), 299-305.
 22. Fabbrini, M.; Trachsel, E.; Soldani, P.; Bindi, S.; Alessi, P.; Bracci, L.; Kosmehl, H.; Zardi, L.; Neri, D.; Neri, P., Selective occlusion of tumor blood vessels by targeted delivery of an antibody-photosensitizer conjugate. *Int J Cancer* **2006**, *118* (7), 1805-1813.
 23. Hirohara, S.; Obata, M.; Saito, A.; Ogata, S.; Ohtsuki, C.; Higashida, S.; Ogura, S.; Okura, I.; Sugai, Y.; Mikata, Y.; Tanihara, M.; Yano, S., Cellular uptake and photocytotoxicity of glycoconjugated porphyrins in HeLa cells. *Photochem Photobiol* **2004**, *80* (2), 301-308.
 24. Lee, P. P. S.; Lo, P. C.; Chan, E. Y. M.; Fong, W. P.; Ko, W. H.; Ng, D. K. P., Synthesis and in vitro photodynamic activity of novel galactose-containing phthalocyanines. *Tetrahedron Lett* **2005**, *46* (9), 1551-1554.
 25. Chen, X.; Hui, L.; Foster, D. A.; Drain, C. M., Efficient synthesis and photodynamic activity

- of porphyrin-saccharide conjugates: Targeting and incapacitating cancer cells. *Biochemistry* **2004**, *43* (34), 10918-10929.
26. Frochot, C.; Di Stasio, B.; Vanderesse, R.; Belgy, M. J.; Dodeller, M.; Guillemin, F.; Viriot, M. L.; Barberi-Heyob, M., Interest of RGD-containing linear or cyclic peptide targeted tetraphenylchlorin as novel photosensitizers for selective photodynamic activity. *Bioorg Chem* **2007**, *35* (3), 205-220.
27. Choi, Y.; McCarthy, J. R.; Weissleder, R.; Tung, C. H., Conjugation of a photosensitizer to an oligoarginine-based cell-penetrating peptide increases the efficacy of photodynamic therapy. *Chemmedchem* **2006**, *1* (4), 458-463.
28. Cho, Y.; Choi, Y., Graphene oxide-photosensitizer conjugate as a redox-responsive theranostic agent. *Chem Commun* **2012**, *48* (79), 9912-9914.
29. Wang, N. N.; Zhao, Z. L.; Lv, Y. F.; Fan, H. H.; Bai, H. R.; Meng, H. M.; Long, Y. Q.; Fu, T.; Zhang, X. B.; Tan, W. H., Gold nanorod-photosensitizer conjugate with extracellular pH-driven tumor targeting ability for photothermal/photodynamic therapy. *Nano Res* **2014**, *7* (9), 1291-1301.
30. Zhen, Z.; Tang, W.; Guo, C.; Chen, H.; Lin, X.; Liu, G.; Fei, B.; Chen, X.; Xu, B.; Xie, J., Ferritin nanocages to encapsulate and deliver photosensitizers for efficient photodynamic therapy against cancer. *ACS Nano* **2013**, *7* (8), 6988-6996.
31. Zhen, Z.; Tang, W.; Wang, M.; Zhou, S.; Wang, H.; Wu, Z.; Hao, Z.; Li, Z.; Liu, L.; Xie, J., Protein Nanocage Mediated Fibroblast-Activation Protein Targeted Photoimmunotherapy To Enhance Cytotoxic T Cell Infiltration and Tumor Control. *Nano Lett* **2017**, *17* (2), 862-869.
32. Zhou, Y.; Ren, X.; Hou, Z.; Wang, N.; Jiang, Y.; Luan, Y., Engineering a photosensitizer nanoplatfrom for amplified photodynamic immunotherapy via tumor microenvironment

- modulation. *Nanoscale Horiz* **2021**, 6 (2), 120-131.
33. Moan, J.; Berg, K., The photodegradation of porphyrins in cells can be used to estimate the lifetime of singlet oxygen. *Photochem Photobiol* **1991**, 53 (4), 549-553.
 34. Kessel, D.; Reiners, J. J., Jr., Apoptosis and autophagy after mitochondrial or endoplasmic reticulum photodamage. *Photochem Photobiol* **2007**, 83 (5), 1024-1028.
 35. Wu, S.; Xing, D., Mechanism of mitochondrial membrane permeabilization during apoptosis under photofrin-mediated photodynamic therapy. *J Xray Sci Technol* **2012**, 20 (3), 363-272.
 36. Juzeniene, A.; Nielsen, K. P.; Moan, J., Biophysical aspects of photodynamic therapy. *J Environ Pathol Toxicol Oncol* **2006**, 25 (1-2), 7-28.
 37. Agostinis, P.; Berg, K.; Cengel, K. A.; Foster, T. H.; Girotti, A. W.; Gollnick, S. O.; Hahn, S. M.; Hamblin, M. R.; Juzeniene, A.; Kessel, D.; Korbelik, M.; Moan, J.; Mroz, P.; Nowis, D.; Piette, J.; Wilson, B. C.; Golab, J., Photodynamic therapy of cancer: an update. *CA Cancer J Clin* **2011**, 61 (4), 250-281.
 38. Tromberg, B. J.; Orenstein, A.; Kimel, S.; Barker, S. J.; Hyatt, J.; Nelson, J. S.; Berns, M. W., In vivo tumor oxygen tension measurements for the evaluation of the efficiency of photodynamic therapy. *Photochem Photobiol* **1990**, 52 (2), 375-385.
 39. Pogue, B. W.; Braun, R. D.; Lanzen, J. L.; Erickson, C.; Dewhirst, M. W., Analysis of the heterogeneity of pO₂ dynamics during photodynamic therapy with verteporfin. *Photochem Photobiol* **2001**, 74 (5), 700-706.
 40. Dolmans, D. E.; Kadambi, A.; Hill, J. S.; Waters, C. A.; Robinson, B. C.; Walker, J. P.; Fukumura, D.; Jain, R. K., Vascular accumulation of a novel photosensitizer, MV6401, causes selective thrombosis in tumor vessels after photodynamic therapy. *Cancer Res* **2002**, 62 (7), 2151-2156.

41. Star, W. M.; Marijnissen, H. P.; van den Berg-Blok, A. E.; Versteeg, J. A.; Franken, K. A.; Reinhold, H. S., Destruction of rat mammary tumor and normal tissue microcirculation by hematoporphyrin derivative photoradiation observed in vivo in sandwich observation chambers. *Cancer Res* **1986**, *46* (5), 2532-2540.
42. Fingar, V. H.; Wieman, T. J.; Haydon, P. S., The effects of thrombocytopenia on vessel stasis and macromolecular leakage after photodynamic therapy using photofrin. *Photochem Photobiol* **1997**, *66* (4), 513-517.
43. Fingar, V. H.; Kik, P. K.; Haydon, P. S.; Cerrito, P. B.; Tseng, M.; Abang, E.; Wieman, T. J., Analysis of acute vascular damage after photodynamic therapy using benzoporphyrin derivative (BPD). *Brit J Cancer* **1999**, *79* (11-12), 1702-1708.
44. Wachowska, M.; Stachura, J.; Tonecka, K.; Fidy, K.; Braniewska, A.; Sas, Z.; Kotula, I.; Rygiel, T. P.; Boon, L.; Golab, J.; Muchowicz, A., Inhibition of IDO leads to IL-6-dependent systemic inflammation in mice when combined with photodynamic therapy. *Cancer Immunol Immun* **2020**, *69* (6), 1101-1112.
45. Henderson, B. W.; Dougherty, T. J., How Does Photodynamic Therapy Work. *Photochem Photobiol* **1992**, *55* (1), 145-157.
46. Gollnick, S. O.; Liu, X. N.; Owczarczak, B.; Musser, D. A.; Henderson, B. W., Altered expression of interleukin 6 and interleukin 10 as a result of photodynamic therapy in vivo. *Cancer Research* **1997**, *57* (18), 3904-3909.
47. Shumaker, B. P.; Hetzel, F. W., Clinical laser photodynamic therapy in the treatment of bladder carcinoma. *Photochem Photobiol* **1987**, *46* (5), 899-901.
48. Yang, Y.; Hu, Y.; Wang, H., Targeting Antitumor Immune Response for Enhancing the Efficacy of Photodynamic Therapy of Cancer: Recent Advances and Future Perspectives. *Oxid*

Med Cell Longev **2016**, 2016, 5274084.

49. Tschen, E. H.; Wong, D. S.; Pariser, D. M.; Dunlap, F. E.; Houlihan, A.; Ferdon, M. B.; Phase IV ALA-PDT Actinic Keratosis Study Group., Photodynamic therapy using aminolaevulinic acid for patients with nonhyperkeratotic actinic keratoses of the face and scalp: phase IV multicentre clinical trial with 12-month follow up. *British Journal of Dermatology* **2006**, 155 (6), 1262-1269.
50. Gollnick, S. O.; Musser, D. A.; Oseroff, A. R.; Vaughan, L.; Owczarczak, B.; Henderson, B. W., IL-10 Does not Play a Role in Cutaneous Photofrin Photodynamic Therapy-induced Suppression of the Contact Hypersensitivity Response. *Photochem Photobiol* **2001**, 74 (6), 811-816.
51. Frost, G. A.; Halliday, G. M.; Damian, D. L., Photodynamic Therapy-Induced Immunosuppression in Humans Is Prevented by Reducing the Rate of Light Delivery. *Journal of Investigative Dermatology* **2011**, 131 (4), 962-968.
52. Mroz, P.; Hamblin, M. R., The immunosuppressive side of PDT. *Photochem Photobiol Sci* **2011**, 10 (5), 751-758.
53. Griffith, T. S.; Kazama, H.; VanOosten, R. L.; Earle, J. K.; Herndon, J. M.; Green, D. R.; Ferguson, T. A., Apoptotic cells induce tolerance by generating helpless CD8(+) T cells that produce TRAIL. *J Immunol* **2007**, 178 (5), 2679-2687.
54. Kazama, H.; Ricci, J. E.; Herndon, J. M.; Hoppe, G.; Green, D. R.; Ferguson, T. A., Induction of immunological tolerance by apoptotic cells requires caspase-dependent oxidation of high-mobility group box-1 protein. *Immunity*. **2008**, 29 (1), 21-32.
55. Wan, J.; Wu, W.; Che, Y.; Kang, N. N.; Zhang, R. Q., Low dose photodynamic-therapy induce immune escape of tumor cells in a HIF-1 alpha, dependent manner through PI3K/Akt pathway.

- Int Immunopharmacol* **2015**, 28 (1), 44-51.
56. Grivennikov, S. I.; Greten, F. R.; Karin, M., Immunity, inflammation, and cancer. *Cell* **2010**, 140 (6), 883-899.
57. Gonzalez, H.; Hagerling, C.; Werb, Z., Roles of the immune system in cancer: from tumor initiation to metastatic progression. *Genes Dev* **2018**, 32 (19-20), 1267-1284.
58. Guillerey, C.; Huntington, N. D.; Smyth, M. J., Targeting natural killer cells in cancer immunotherapy. *Nature Immunology* **2016**, 17 (9), 1025-1036.
59. Liu, Y.; Guo, J.; Huang, L., Modulation of tumor microenvironment for immunotherapy: focus on nanomaterial-based strategies. *Theranostics* **2020**, 10 (7), 3099-3117.
60. Hwang, H. S.; Shin, H.; Han, J.; Na, K., Combination of photodynamic therapy (PDT) and anti-tumor immunity in cancer therapy. *J Pharm Investig* **2018**, 48 (2), 143-151.
61. Seidel, J. A.; Otsuka, A.; Kabashima, K., Anti-PD-1 and Anti-CTLA-4 Therapies in Cancer: Mechanisms of Action, Efficacy, and Limitations. *Front Oncol* **2018**, 8, 86.
62. Leach, D. R.; Krummel, M. F.; Allison, J. P., Enhancement of antitumor immunity by CTLA-4 blockade. *Science* **1996**, 271 (5256), 1734-1736.
63. Ishida, Y.; Agata, Y.; Shibahara, K.; Honjo, T., Induced Expression of Pd-1, a Novel Member of the Immunoglobulin Gene Superfamily, Upon Programmed Cell-Death. *Embo J* **1992**, 11 (11), 3887-3895.
64. Kinter, A. L.; Godbout, E. J.; McNally, J. P.; Sereti, I.; Roby, G. A.; O'Shea, M. A.; Fauci, A. S., The common gamma-chain cytokines IL-2, IL-7, IL-15, and IL-21 induce the expression of programmed death-1 and its ligands. *J Immunol* **2008**, 181 (10), 6738-6746.
65. Latchman, Y.; Wood, C. R.; Chernova, T.; Chaudhary, D.; Borde, M.; Chernova, I.; Iwai, Y.; Long, A. J.; Brown, J. A.; Nunes, R.; Greenfield, E. A.; Bourque, K.; Boussiotis, V. A.; Carter,

- L. L.; Carreno, B. M.; Malenkovich, N.; Nishimura, H.; Okazaki, T.; Honjo, T.; Sharpe, A. H., Freeman, G. J., PD-L2 is a second ligand for PD-1 and inhibits T cell activation. *Nat Immunol*, **2001**, 2 (3), 261–268
66. Boussiotis, V. A.; Chatterjee, P.; Li, L., Biochemical signaling of PD-1 on T cells and its functional implications. *Cancer J* **2014**, 20 (4), 265-271.
67. Nam, J.; Son, S.; Park, K. S.; Zou, W. P.; Shea, L. D.; Moon, J. J., Cancer nanomedicine for combination cancer immunotherapy. *Nat Rev Mater* **2019**, 4 (6), 398-414.
68. Bauer, C. A.; Kim, E. Y.; Marangoni, F.; Carrizosa, E.; Claudio, N. M.; Mempel, T. R., Dynamic Treg interactions with intratumoral APCs promote local CTL dysfunction. *J Clin Invest* **2014**, 124 (6), 2425-2440.
69. Munn, D. H.; Bronte, V., Immune suppressive mechanisms in the tumor microenvironment. *Curr Opin Immunol* **2016**, 39, 1-6.
70. Dougan, M.; Dranoff, G., Immune therapy for cancer. *Annu Rev Immunol* **2009**, 27, 83-117.
71. Mellman, I.; Coukos, G.; Dranoff, G., Cancer immunotherapy comes of age. *Nature* **2011**, 480 (7378), 480-489.
72. Michot, J. M.; Bigenwald, C.; Champiat, S.; Collins, M.; Carbonnel, F.; Postel Vinay, S.; Berdelou, A.; Varga, A.; Bahleda, R.; Hollebecque, A.; Massard, C.; Fuerea, A.; Ribrag, V.; Gazzah, A.; Armand, J. P.; Amellal, N.; Angevin, E.; Noel, N.; Boutros, C.; Mateus, C.; Robert, C.; Soria, J. C.; Marabelle, A.; Lambotte, O., Immune-related adverse events with immune checkpoint blockade: a comprehensive review. *Eur J Cancer* **2016**, 54, 139-148.
73. Wei, S. C.; Duffy, C. R.; Allison, J. P., Fundamental Mechanisms of Immune Checkpoint Blockade Therapy. *Cancer Discovery* **2018**, 8 (9), 1069.
74. Prendergast, G. C.; Mondal, A.; Dey, S.; Laury-Kleintop, L. D.; Muller, A. J., Inflammatory

- Reprogramming with IDO1 Inhibitors: Turning Immunologically Unresponsive 'Cold' Tumors 'Hot'. *Trends Cancer* **2018**, 4 (1), 38-58.
75. Pardoll, D. M., The blockade of immune checkpoints in cancer immunotherapy. *Nat Rev Cancer* **2012**, 12 (4), 252-264.
 76. Sharma, P.; Allison, J. P., Immune checkpoint targeting in cancer therapy: toward combination strategies with curative potential. *Cell* **2015**, 161 (2), 205-214.
 77. Dovedi, S. J.; Adlard, A. L.; Lipowska-Bhalla, G.; McKenna, C.; Jones, S.; Cheadle, E. J.; Stratford, I. J.; Poon, E.; Morrow, M.; Stewart, R.; Jones, H.; Wilkinson, R. W.; Honeychurch, J.; Illidge, T. M., Acquired Resistance to Fractionated Radiotherapy Can Be Overcome by Concurrent PD-L1 Blockade. *Cancer Res* **2014**, 74 (19), 5458-5468.
 78. Schaeue, D.; Xie, M. W.; Ratikan, J. A.; McBride, W. H., Regulatory T cells in radiotherapeutic responses. *Front Oncol* **2012**, 2, 90.
 79. Lamberti, M. J.; Mentucci, F. M.; Roselli, E.; Araya, P.; Rivarola, V. A.; Rumie Vittar, N. B.; Maccioni, M., Photodynamic Modulation of Type 1 Interferon Pathway on Melanoma Cells Promotes Dendritic Cell Activation. *Front Immunol* **2019**, 10, 2614.
 80. Zhai, L.; Spranger, S.; Binder, D. C.; Gritsina, G.; Lauing, K. L.; Giles, F. J.; Wainwright, D. A., Molecular Pathways: Targeting IDO1 and Other Tryptophan Dioxygenases for Cancer Immunotherapy. *Clin Cancer Res* **2015**, 21 (24), 5427-5433.
 81. Hornyak, L.; Dobos, N.; Koncz, G.; Karanyi, Z.; Pall, D.; Szabo, Z.; Halmos, G.; Szekvolgyi, L., The Role of Indoleamine-2,3-Dioxygenase in Cancer Development, Diagnostics, and Therapy. *Front Immunol* **2018**, 9, 151.
 82. Dai, X.; Zhu, B. T., Indoleamine 2,3-dioxygenase tissue distribution and cellular localization in mice: implications for its biological functions. *J Histochem Cytochem* **2010**, 58 (1), 17-28.

83. Bilir, C.; Sarisozen, C., Indoleamine 2,3-dioxygenase (IDO): Only an enzyme or a checkpoint controller? *Journal of Oncological Sciences* **2017**, 3 (2), 52-56.
84. Munn, D. H.; Mellor, A. L., Indoleamine 2,3 dioxygenase and metabolic control of immune responses. *Trends Immunol* **2013**, 34 (3), 137-143.
85. Holmgaard, R. B.; Zamarin, D.; Li, Y.; Gasmi, B.; Munn, D. H.; Allison, J. P.; Merghoub, T.; Wolchok, J. D., Tumor-Expressed IDO Recruits and Activates MDSCs in a Treg-Dependent Manner. *Cell Rep* **2015**, 13 (2), 412-424.
86. Jusof, F. F.; Bakmiwewa, S. M.; Weiser, S.; Too, L. K.; Metz, R.; Prendergast, G. C.; Fraser, S. T.; Hunt, N. H.; Ball, H. J., Investigation of the Tissue Distribution and Physiological Roles of Indoleamine 2,3-Dioxygenase-2. *Int J Tryptophan Res* **2017**, 10, 1178646917735098.
87. Metz, R.; DuHadaway, J. B.; Kamasani, U.; Laury-Kleintop, L.; Muller, A. J.; Prendergast, G. C., Novel tryptophan catabolic enzyme IDO2 is the preferred biochemical target of the antitumor indoleamine 2,3-dioxygenase inhibitory compound D-1-methyl-tryptophan. *Cancer Res* **2007**, 67 (15), 7082-7087.
88. Löb, S.; Königsrainer, A.; Zieker, D.; Brücher, B. L. D. M.; Rammensee, H.-G.; Opelz, G.; Terness, P., IDO1 and IDO2 are expressed in human tumors: levo- but not dextro-1-methyl tryptophan inhibits tryptophan catabolism. *Cancer Immunol Immunother* **2009**, 58 (1), 153-157.
89. Panozzo, C.; Nawara, M.; Suski, C.; Kucharczyka, R.; Skoneczny, M.; Becam, A. M.; Rytka, J.; Herbert, C. J., Aerobic and anaerobic NAD⁺ metabolism in *Saccharomyces cerevisiae*. *FEBS Lett* **2002**, 517 (1-3), 97-102.
90. Taylor, M. W.; Feng, G. S., Relationship between Interferon-Gamma, Indoleamine 2,3-Dioxygenase, and Tryptophan Catabolism. *Faseb J* **1991**, 5 (11), 2516-2522.

91. Opitz, C. A.; Somarribas Patterson, L. F.; Mohapatra, S. R.; Dewi, D. L.; Sadik, A.; Platten, M.; Trump, S., The therapeutic potential of targeting tryptophan catabolism in cancer. *Br J Cancer* **2020**, *122* (1), 30-44.
92. Kim, R.; Emi, M.; Tanabe, K., Cancer immunoediting from immune surveillance to immune escape. *Immunology* **2007**, *121* (1), 1-14.
93. Dunn, G. P.; Bruce, A. T.; Ikeda, H.; Old, L. J.; Schreiber, R. D., Cancer immunoediting: from immunosurveillance to tumor escape. *Nat Immunol* **2002**, *3* (11), 991-998.
94. Prendergast, G. C.; Smith, C.; Thomas, S.; Mandik-Nayak, L.; Laury-Kleintop, L.; Metz, R.; Muller, A. J., Indoleamine 2,3-dioxygenase pathways of pathogenic inflammation and immune escape in cancer. *Cancer Immunol Immunother* **2014**, *63* (7), 721-735.
95. Fallarino, F.; Grohmann, U.; You, S.; McGrath, B. C.; Cavener, D. R.; Vacca, C.; Orabona, C.; Bianchi, R.; Belladonna, M. L.; Volpi, C.; Santamaria, P.; Fioretti, M. C.; Puccetti, P., The combined effects of tryptophan starvation and tryptophan catabolites down-regulate T cell receptor zeta-chain and induce a regulatory phenotype in naive T cells. *J Immunol* **2006**, *176* (11), 6752-6761.
96. Ravishankar, B.; Liu, H. Y.; Shinde, R.; Chaudhary, K.; Xiao, W.; Bradley, J.; Koritzinsky, M.; Madaio, M. P.; McGaha, T. L., The amino acid sensor GCN2 inhibits inflammatory responses to apoptotic cells promoting tolerance and suppressing systemic autoimmunity. *P Natl Acad Sci USA* **2015**, *112* (34), 10774-10779.
97. Munn, D. H.; Sharma, M. D.; Baban, B.; Harding, H. P.; Zhang, Y.; Ron, D.; Mellor, A. L., GCN2 kinase in T cells mediates proliferative arrest and anergy induction in response to indoleamine 2,3-dioxygenase. *Immunity* **2005**, *22* (5), 633-42.
98. Brenk, M.; Scheler, M.; Koch, S.; Neumann, J.; Takikawa, O.; Hacker, G.; Bieber, T.; von

- Bubnoff, D., Tryptophan deprivation induces inhibitory receptors ILT3 and ILT4 on dendritic cells favoring the induction of human CD4⁺CD25⁺ Foxp3⁺ T regulatory cells. *J Immunol* **2009**, *183* (1), 145-154.
99. Fox, E.; Oliver, T.; Rowe, M.; Thomas, S.; Zakharia, Y.; Gilman, P. B.; Muller, A. J.; Prendergast, G. C., Indoximod: An Immunometabolic Adjuvant That Empowers T Cell Activity in Cancer. *Front Oncol* **2018**, *8*, 370.
100. Spranger, S.; Spaapen, R. M.; Zha, Y.; Williams, J.; Meng, Y.; Ha, T. T.; Gajewski, T. F., Up-Regulation of PD-L1, IDO, and T-regs in the Melanoma Tumor Microenvironment Is Driven by CD8(+) T Cells. *Sci Transl Med* **2013**, *5* (200), 200ra116.
101. Mellor, A. L.; Munn, D. H., IDO expression by dendritic cells: tolerance and tryptophan catabolism. *Nat Rev Immunol* **2004**, *4* (10), 762-774.
102. Wang, D. D.; Saga, Y.; Mizukami, H.; Sato, N.; Nonaka, H.; Fujiwara, H.; Takei, Y.; Machida, S.; Takikawa, O.; Ozawa, K.; Suzuki, M., Indoleamine-2,3-dioxygenase, an immunosuppressive enzyme that inhibits natural killer cell function, as a useful target for ovarian cancer therapy. *Int J Oncol* **2012**, *40* (4), 929-934.
103. Mellor, A. L.; Keskin, D. B.; Johnson, T.; Chandler, P.; Munn, D. H., Cells expressing indoleamine 2,3-dioxygenase inhibit T cell responses. *J Immunol* **2002**, *168* (8), 3771-3776.
104. Godin-Ethier, J.; Hanafi, L. A.; Piccirillo, C. A.; Lapointe, R., Indoleamine 2,3-dioxygenase expression in human cancers: clinical and immunologic perspectives. *Clin Cancer Res* **2011**, *17* (22), 6985-6991.
105. Li, Q.; Harden, J. L.; Anderson, C. D.; Egilmez, N. K., Tolerogenic Phenotype of IFN- γ -Induced IDO⁺ Dendritic Cells Is Maintained via an Autocrine IDO-Kynurenine/AhR-IDO Loop. *J Immunol* **2016**, *197* (3), 962-970.

- 106.DiNatale, B. C.; Murray, I. A.; Schroeder, J. C.; Flaveny, C. A.; Lahoti, T. S.; Laurenzana, E. M.; Omiecinski, C. J.; Perdew, G. H., Kynurenic Acid Is a Potent Endogenous Aryl Hydrocarbon Receptor Ligand that Synergistically Induces Interleukin-6 in the Presence of Inflammatory Signaling. *Toxicol Sci* **2010**, *115* (1), 89-97.
- 107.Nguyen, N. T.; Kimura, A.; Nakahama, T.; Chinen, I.; Masuda, K.; Nohara, K.; Fujii-Kuriyama, Y.; Kishimoto, T., Aryl hydrocarbon receptor negatively regulates dendritic cell immunogenicity via a kynurenine-dependent mechanism. *Proc Natl Acad Sci U S A* **2010**, *107* (46), 19961-19966.
- 108.Mezrich, J. D.; Fechner, J. H.; Zhang, X. J.; Johnson, B. P.; Burlingham, W. J.; Bradfield, C. A., An Interaction between Kynurenine and the Aryl Hydrocarbon Receptor Can Generate Regulatory T Cells. *J Immunol* **2010**, *185* (6), 3190-3198.
- 109.Quintana, F. J.; Murugaiyan, G.; Farez, M. F.; Mitsdoerffer, M.; Tukupah, A. M.; Burns, E. J.; Weiner, H. L., An endogenous aryl hydrocarbon receptor ligand acts on dendritic cells and T cells to suppress experimental autoimmune encephalomyelitis. *Proc Natl Acad Sci U S A* **2010**, *107* (48), 20768-20773.
- 110.Takenaka, M. C.; Gabriely, G.; Rothhammer, V.; Mascanfroni, I. D.; Wheeler, M. A.; Chao, C. C.; Gutierrez-Vazquez, C.; Kenison, J.; Tjon, E. C.; Barroso, A.; Vandeventer, T.; de Lima, K. A.; Rothweiler, S.; Mayo, L.; Ghannam, S.; Zandee, S.; Healy, L.; Sherr, D.; Farez, M. F.; Pratt, A.; Antel, J.; Reardon, D. A.; Zhang, H.; Robson, S. C.; Getz, G.; Weiner, H. L.; Quintana, F. J., Control of tumor-associated macrophages and T cells in glioblastoma via AHR and CD39. *Nat Neurosci* **2019**, *22* (5), 729-740.
- 111.Munn, D. H.; Mellor, A. L., IDO in the Tumor Microenvironment: Inflammation, Counter-Regulation, and Tolerance. *Trends Immunol* **2016**, *37* (3), 193-207.

- 112.Lu, K.; He, C.; Guo, N.; Chan, C.; Ni, K.; Weichselbaum, R. R.; Lin, W., Chlorin-Based Nanoscale Metal-Organic Framework Systemically Rejects Colorectal Cancers via Synergistic Photodynamic Therapy and Checkpoint Blockade Immunotherapy. *J Am Chem Soc* **2016**, *138* (38), 12502-12510.
- 113.Chen, Y. C.; Xia, R.; Huang, Y. X.; Zhao, W. C.; Li, J.; Zhang, X. L.; Wang, P. C.; Venkataramanan, R.; Fan, J.; Xie, W.; Ma, X. C.; Lu, B. F.; Li, S., An immunostimulatory dual-functional nanocarrier that improves cancer immunochemotherapy. *Nat Commun* **2016**, *7*, 13443.
- 114.Huang, Z. Q.; Wei, G. F.; Zeng, Z. S.; Huang, Y. J.; Huang, L. F.; Shen, Y. F.; Sun, X. Q.; Xu, C. J.; Zhao, C. S., Enhanced cancer therapy through synergetic photodynamic/immune checkpoint blockade mediated by a liposomal conjugate comprised of porphyrin and IDO inhibitor. *Theranostics* **2019**, *9* (19), 5542-5557.
- 115.Peng, J. R.; Xiao, Y.; Li, W. T.; Yang, Q.; Tan, L. W.; Jia, Y. P.; Qian, Z. Y., Photosensitizer Micelles Together with IDO Inhibitor Enhance Cancer Photothermal Therapy and Immunotherapy. *Adv Sci* **2018**, *5* (5), 1700891.
- 116.Mautino, M. R.; Jaipuri, F. A.; Waldo, J.; Kumar, S.; Adams, J.; Van Allen, C.; Marcinowicz-Flick, A.; Munn, D.; Vahanian, N.; Link, C. J., Abstract 491: NLG919, a novel indoleamine-2,3-dioxygenase (IDO)-pathway inhibitor drug candidate for cancer therapy. *Cancer Res* **2013**, *73* (8 Supplement), 491.
- 117.Peng, Y. H.; Ueng, S. H.; Tseng, C. T.; Hung, M. S.; Song, J. S.; Wu, J. S.; Liao, F. Y.; Fan, Y. S.; Wu, M. H.; Hsiao, W. C.; Hsueh, C. C.; Lin, S. Y.; Cheng, C. Y.; Tu, C. H.; Lee, L. C.; Cheng, M. F.; Shia, K. S.; Shih, C.; Wu, S. Y., Important Hydrogen Bond Networks in Indoleamine 2,3-Dioxygenase 1 (IDO1) Inhibitor Design Revealed by Crystal Structures of

- Imidazoleisoindole Derivatives with IDO1. *J Med Chem* **2016**, 59 (1), 282-293.
- 118.Cheong, J. E.; Ekkati, A.; Sun, L. J., A patent review of IDO1 inhibitors for cancer. *Expert Opin Ther Pat* **2018**, 28 (4), 317-330.
- 119.Zielinska, A.; Carreiro, F.; Oliveira, A. M.; Neves, A.; Pires, B.; Venkatesh, D. N.; Durazzo, A.; Lucarini, M.; Eder, P.; Silva, A. M.; Santini, A.; Souto, E. B., Polymeric Nanoparticles: Production, Characterization, Toxicology and Ecotoxicology. *Molecules* **2020**, 25 (16), 3731.
- 120.Zulfiqar, B.; Mahroo, A.; Nasir, K.; Farooq, R. K.; Jalal, N.; Rashid, M. U.; Asghar, K., Nanomedicine and cancer immunotherapy: focus on indoleamine 2,3-dioxygenase inhibitors. *Onco Targets Ther* **2017**, 10, 463-476.
- 121.Davis, M. E.; Chen, Z.; Shin, D. M., Nanoparticle therapeutics: an emerging treatment modality for cancer. *Nat Rev Drug Discov* **2008**, 7 (9), 771-782.
- 122.Master, A.; Livingston, M.; Sen Gupta, A., Photodynamic nanomedicine in the treatment of solid tumors: Perspectives and challenges. *J Control Release* **2013**, 168 (1), 88-102.
- 123.Peer, D.; Karp, J. M.; Hong, S.; Farokhzad, O. C.; Margalit, R.; Langer, R., Nanocarriers as an emerging platform for cancer therapy. *Nat Nanotechnol* **2007**, 2 (12), 751-760.
- 124.Bechet, D.; Couleaud, P.; Frochot, C.; Viriot, M. L.; Guillemin, F.; Barberi-Heyob, M., Nanoparticles as vehicles for delivery of photodynamic therapy agents. *Trends Biotechnol* **2008**, 26 (11), 612-621.
- 125.Prabhakar, U.; Maeda, H.; Jain, R. K.; Sevik-Muraca, E. M.; Zamboni, W.; Farokhzad, O. C.; Barry, S. T.; Gabizon, A.; Grodzinski, P.; Blakey, D. C., Challenges and key considerations of the enhanced permeability and retention effect for nanomedicine drug delivery in oncology. *Cancer Res* **2013**, 73 (8), 2412-2417.
- 126.Zhen, Z. P.; Tang, W.; Todd, T.; Xie, J., Ferritins as nanoplatfroms for imaging and drug

- delivery. *Expert Opin Drug Del* **2014**, *11* (12), 1913-1922.
- 127.Zhang, K. R.; Tang, X.; Zhang, J.; Lu, W.; Lin, X.; Zhang, Y.; Tian, B.; Yang, H.; He, H. B., PEG-PLGA copolymers: Their structure and structure-influenced drug delivery applications. *J Control Release* **2014**, *183*, 77-86.
- 128.Mirakabad, F. S. T.; Nejati-Koshki, K.; Akbarzadeh, A.; Yamchi, M. R.; Milani, M.; Zarghami, N.; Zeighamian, V.; Rahimzadeh, A.; Alimohammadi, S.; Hanifehpour, Y.; Joo, S. W., PLGA-Based Nanoparticles as Cancer Drug Delivery Systems. *Asian Pac J Cancer P* **2014**, *15* (2), 517-535.
- 129.Xing, L.; Gong, J. H.; Wang, Y.; Zhu, Y.; Huang, Z. J.; Zhao, J.; Li, F.; Wang, J. H.; Wen, H.; Jiang, H. L., Hypoxia alleviation-triggered enhanced photodynamic therapy in combination with IDO inhibitor for preferable cancer therapy. *Biomaterials* **2019**, *206*, 170-182.
- 130.Lu, J. Q.; Liu, X. S.; Liao, Y. P.; Wang, X.; Ahmed, A.; Jiang, W.; Ji, Y.; Meng, H.; Nel, A. E., Breast Cancer Chemo-immunotherapy through Liposomal Delivery of an Immunogenic Cell Death Stimulus Plus Interference in the IDO-1 Pathway. *Acs Nano* **2018**, *12* (11), 11041-11061.
- 131.Liu, Y. J.; Lu, Y.; Zhu, X. H. Li, C.; Yan, M. M.; Pan, J.; Ma, G. L., Tumor microenvironment-responsive prodrug nanoplatfrom via co-self-assembly of photothermal agent and IDO inhibitor for enhanced tumor penetration and cancer immunotherapy. *Biomaterials* **2020**, *242*, 119933.
- 132.Lu, J. Q.; Liu, X. S.; Liao, Y. P.; Salazar, F.; Sun, B. B.; Jiang, W.; Chang, C. H.; Jiang, J. H.; Wang, X.; Wu, A. M.; Meng, H.; Nel, A. E., Nano-enabled pancreas cancer immunotherapy using immunogenic cell death and reversing immunosuppression. *Nat Commun* **2017**, *8*, 1811.
- 133.Liu, D. C.; Chen, B. L.; Mo, Y. L.; Wang, Z. H.; Qi, T.; Zhang, Q.; Wang, Y. G., Redox-Activated Porphyrin-Based Liposome Remote-Loaded with Indoleamine 2,3-Dioxygenase

- (IDO) Inhibitor for Synergistic Photoimmunotherapy through Induction of Immunogenic Cell Death and Blockage of IDO Pathway. *Nano Lett* **2019**, *19* (10), 6964-6976.
134. Gupta, A.; Wang, S. Y.; Pera, P.; Rao, K. V. R.; Patel, N.; Ohulchanskyy, T. Y.; Missert, J.; Morgan, J.; Koo-Lee, Y. E.; Kopelman, R.; Pandey, R. K., Multifunctional nanoplatforms for fluorescence imaging and photodynamic therapy developed by post-loading photosensitizer and fluorophore to polyacrylamide nanoparticles. *Nanomed-Nanotechnol* **2012**, *8* (6), 941-950.
135. Derycke, A. S.; de Witte, P. A., Liposomes for photodynamic therapy. *Adv Drug Deliv Rev* **2004**, *56* (1), 17-30.
136. Brevet, D.; Gary-Bobo, M.; Raehm, L.; Richeter, S.; Hocine, O.; Amro, K.; Looock, B.; Couleaud, P.; Frochot, C.; Morere, A.; Maillard, P.; Garcia, M.; Durand, J. O., Mannose-targeted mesoporous silica nanoparticles for photodynamic therapy. *Chem Commun (Camb)* **2009**, (12), 1475-1477.
137. Wolinsky, J. B.; Grinstaff, M. W., Therapeutic and diagnostic applications of dendrimers for cancer treatment. *Adv Drug Deliver Rev* **2008**, *60* (9), 1037-1055.
138. Cheng, Y.; Samia, A. C.; Li, J.; Kenney, M. E.; Resnick, A.; Burda, C., Delivery and Efficacy of a Cancer Drug as a Function of the Bond to the Gold Nanoparticle Surface. *Langmuir* **2010**, *26* (4), 2248-2255.
139. Sharma, S. K.; Chiang, L. Y.; Hamblin, M. R., Photodynamic therapy with fullerenes in vivo: reality or a dream? *Nanomedicine (Lond)* **2011**, *6* (10), 1813-1825.
140. Rozhkova, E. A.; Ulasov, I.; Lai, B.; Dimitrijevic, N. M.; Lesniak, M. S.; Rajh, T., A High-Performance Nanobio Photocatalyst for Targeted Brain Cancer Therapy. *Nano Lett* **2009**, *9* (9), 3337-3342.

141. Hackenberg, S.; Scherzed, A.; Kessler, M.; Froelich, K.; Ginzkey, C.; Koehler, C.; Burghartz, M.; Hagen, R.; Kleinsasser, N., Zinc oxide nanoparticles induce photocatalytic cell death in human head and neck squamous cell carcinoma cell lines in vitro. *Int J Oncol* **2010**, *37* (6), 1583-1590.
142. Theil, E. C., Ferritin - Structure, Gene-Regulation, and Cellular Function in Animals, Plants, and Microorganisms. *Annu Rev Biochem* **1987**, *56*, 289-315.
143. Ensign, D.; Young, M.; Douglas, T., Photocatalytic synthesis of copper colloids from CuII by the ferrihydrite core of ferritin. *Inorg Chem* **2004**, *43* (11), 3441-3446.
144. Hosein, H. A.; Strongin, D. R.; Allen, M.; Douglas, T., Iron and Cobalt oxide and metallic nanoparticles prepared from ferritin. *Langmuir* **2004**, *20* (23), 10283-10287.
145. Wang, J. J.; Zhang, L. W.; Chen, M. L.; Gao, S.; Zhu, L., Activatable Ferritin Nanocomplex for Real-Time Monitoring of Caspase-3 Activation during Photodynamic Therapy. *Acs Appl Mater Inter* **2015**, *7* (41), 23248-23256.
146. Zhen, Z. P.; Tang, W.; Chen, H. M.; Lin, X.; Todd, T.; Wang, G.; Cowger, T.; Chen, X. Y.; Xie, J., RGD-Modified Apoferritin Nanoparticles for Efficient Drug Delivery to Tumors. *Acs Nano* **2013**, *7* (6), 4830-4837.
147. Hainfeld, J. F., Uranium-Loaded Apoferritin with Antibodies Attached - Molecular Design for Uranium Neutron-Capture Therapy. *Proc Natl Acad Sci U S A* **1992**, *89* (22), 11064-11068.
148. Maham, A.; Tang, Z.; Wu, H.; Wang, J.; Lin, Y., Protein-based nanomedicine platforms for drug delivery. *Small* **2009**, *5* (15), 1706-1721.
149. Zhou, S. Y.; Zhen, Z. P.; Paschall, A. V.; Xue, L. J.; Yang, X. Y.; Blackwell, A. G. B.; Cao, Z. W.; Zhang, W. Z.; Wang, M. Z.; Teng, Y.; Zhou, G.; Li, Z. B.; Avci, F. Y.; Tang, W.; Xie, J., FAP-Targeted Photodynamic Therapy Mediated by Ferritin Nanoparticles Elicits an Immune

- Response against Cancer Cells and Cancer Associated Fibroblasts. *Adv Funct Mater* **2020**, *31* (7), 2007017.
- 150.Zhen, Z. P.; Tang, W.; Zhang, W. Z.; Xie, J., Folic acid conjugated ferritins as photosensitizer carriers for photodynamic therapy. *Nanoscale* **2015**, *7* (23), 10330-10333.
- 151.Zhen, Z.; Tang, W.; Chuang, Y. J.; Todd, T.; Zhang, W.; Lin, X.; Niu, G.; Liu, G.; Wang, L.; Pan, Z.; Chen, X.; Xie, J., Tumor vasculature targeted photodynamic therapy for enhanced delivery of nanoparticles. *ACS Nano* **2014**, *8* (6), 6004-6013.
- 152.Huang, C.; Chu, C. C.; Wang, X. Y.; Lin, H. R.; Wang, J. Q.; Zeng, Y.; Zhu, W. Z.; Wang, Y. X. J.; Liu, G., Ultra-high loading of sinoporphyrin sodium in ferritin for single-wave motivated photothermal and photodynamic co-therapy. *Biomater Sci-Uk* **2017**, *5* (8), 1512-1516.
- 153.Li, L.; Zhou, S.; Lv, N.; Zhen, Z.; Liu, T.; Gao, S.; Xie, J.; Ma, Q., Photosensitizer-Encapsulated Ferritins Mediate Photodynamic Therapy against Cancer-Associated Fibroblasts and Improve Tumor Accumulation of Nanoparticles. *Mol Pharm* **2018**, *15* (8), 3595-3599.
- 154.Liu, M. M.; Zhu, Y.; Wu, T. T.; Cheng, J. J.; Liu, Y. Z., Nanobody-Ferritin Conjugate for Targeted Photodynamic Therapy. *Chem-Eur J* **2020**, *26* (33), 7442-7450.
- 155.Zhou, S.; Li, D.; Lee, C.; Xie, J., Nanoparticle Phototherapy in the Era of Cancer Immunotherapy. *Trends in Chemistry* **2020**, *2* (12), 1082-1095.
- 156.Gorabi, A. M.; Kiaie, N.; Reiner, Z.; Carbone, F.; Montecucco, F.; Sahebkar, A., The Therapeutic Potential of Nanoparticles to Reduce Inflammation in Atherosclerosis. *Biomolecules* **2019**, *9* (9), 416.
- 157.Malam, Y.; Loizidou, M.; Seifalian, A. M., Liposomes and nanoparticles: nanosized vehicles for drug delivery in cancer. *Trends Pharmacol Sci* **2009**, *30* (11), 592-599.

- 158.Owens, D. E., 3rd; Peppas, N. A., Opsonization, biodistribution, and pharmacokinetics of polymeric nanoparticles. *Int J Pharm* **2006**, *307* (1), 93-102.
- 159.Noble, C. O.; Kirpotin, D. B.; Hayes, M. E.; Mamot, C.; Hong, K.; Park, J. W.; Benz, C. C.; Marks, J. D.; Drummond, D. C., Development of ligand-targeted liposomes for cancer therapy. *Expert Opin Ther Targets* **2004**, *8* (4), 335-353.
- 160.Soppimath, K. S.; Aminabhavi, T. M.; Kulkarni, A. R.; Rudzinski, W. E., Biodegradable polymeric nanoparticles as drug delivery devices. *J Control Release* **2001**, *70* (1-2), 1-20.
- 161.Hirst, S. M.; Karakoti, A. S.; Tyler, R. D.; Sriranganathan, N.; Seal, S.; Reilly, C. M., Anti-inflammatory properties of cerium oxide nanoparticles. *Small* **2009**, *5* (24), 2848-2856.
- 162.Zhong, G.; Yang, X.; Jiang, X.; Kumar, A.; Long, H.; Xie, J.; Zheng, L.; Zhao, J., Dopamine-melanin nanoparticles scavenge reactive oxygen and nitrogen species and activate autophagy for osteoarthritis therapy. *Nanoscale* **2019**, *11* (24), 11605-11616.
- 163.Wong, K. K. Y.; Cheung, S. O. F.; Huang, L. M.; Niu, J.; Tao, C.; Ho, C. M.; Che, C. M.; Tam, P. K. H., Further Evidence of the Anti-inflammatory Effects of Silver Nanoparticles. *Chemmedchem* **2009**, *4* (7), 1129-1135.
- 164.Waters, E. S.; Kaiser, E. E.; Yang, X.; Fagan, M. M.; Scheulin, K. M.; Jeon, J. H.; Shin, S. K.; Kinder, H. A.; Kumar, A.; Platt, S. R.; Duberstein, K. J.; Park, H. J.; Xie, J.; West, F. D., Intracisternal administration of tanshinone IIA-loaded nanoparticles leads to reduced tissue injury and functional deficits in a porcine model of ischemic stroke. *IBRO Neuroscience Reports* **2021**, *10*, 18-30.
- 165.Tang, S. Y.; Sivakumar, M.; Ng, A. M. H.; Shridharan, P., Anti-inflammatory and analgesic activity of novel oral aspirin-loaded nanoemulsion and nano multiple emulsion formulations generated using ultrasound cavitation. *Int J Pharmaceut* **2012**, *430* (1-2), 299-306.

- 166.El-Ghazaly, M. A.; Fadel, N.; Rashed, E.; El-Batal, A.; Kenawy, S. A., Anti-inflammatory effect of selenium nanoparticles on the inflammation induced in irradiated rats. *Can J Physiol Pharmacol* **2017**, *95* (2), 101-110.
- 167.Pu, H. L.; Chiang, W. L.; Maiti, B.; Liao, Z. X.; Ho, Y. C.; Shim, M. S.; Chuang, E. Y.; Xia, Y. N.; Sung, H. W., Nanoparticles with Dual Responses to Oxidative Stress and Reduced pH for Drug Release and Anti-inflammatory Applications. *Acs Nano* **2014**, *8* (2), 1213-1221.
- 168.Nadworny, P. L.; Wang, J. F.; Tredget, E. E.; Burrell, R. E., Anti-inflammatory activity of nanocrystalline silver in a porcine contact dermatitis model. *Nanomed-Nanotechnol* **2008**, *4* (3), 241-251.
- 169.Perioli, L.; Posati, T.; Nocchetti, M.; Bellezza, F.; Costantino, U.; Cipiciani, A., Intercalation and release of antiinflammatory drug diclofenac into nanosized ZnAl hydrotalcite-like compound. *Appl Clay Sci* **2011**, *53* (3), 374-378.
- 170.Mahon, O. R.; Browe, D. C.; Gonzalez-Fernandez, T.; Pitacco, P.; Whelan, I. T.; Von Euw, S.; Hobbs, C.; Nicolosi, V.; Cunningham, K. T.; Mills, K. H. G.; Kelly, D. J.; Dunne, A., Nano-particle mediated M2 macrophage polarization enhances bone formation and MSC osteogenesis in an IL-10 dependent manner. *Biomaterials* **2020**, *239*, 119833.
- 171.Jeengar, M. K.; Rompicharla, V. K.; Shrivastava, S.; Chella, N.; Shastri, N. R.; Naidu, V. G. M.; Sistla, R., Emu oil based nano-emulgel for topical delivery of curcumin. *Int J Pharmaceut* **2016**, *506* (1-2), 222-236.
- 172.Friedman, A. J.; Phan, J.; Schairer, D. O.; Champer, J.; Qin, M.; Pirouz, A.; Blecher-Paz, K.; Oren, A.; Liu, P. T.; Modlin, R. L.; Kim, J., Antimicrobial and Anti-Inflammatory Activity of Chitosan Alginate Nanoparticles: A Targeted Therapy for Cutaneous Pathogens. *J Invest Dermatol* **2013**, *133* (5), 1231-1239.

- 173.Hosseini, S. H.; Maleki, A.; Eshraghi, H. R.; Hamidi, M., Preparation and in vitro/pharmacokinetic/pharmacodynamic evaluation of a slow-release nano-liposomal form of prednisolone. *Drug Deliv* **2016**, 23 (8), 3008-3016.
- 174.Milla Sanabria, L.; Rodriguez, M. E.; Cogno, I. S.; Rumie Vittar, N. B.; Pansa, M. F.; Lamberti, M. J.; Rivarola, V. A., Direct and indirect photodynamic therapy effects on the cellular and molecular components of the tumor microenvironment. *Biochim Biophys Acta* **2013**, 1835 (1), 36-45.
- 175.Xu, J.; Xu, L.; Wang, C.; Yang, R.; Zhuang, Q.; Han, X.; Dong, Z.; Zhu, W.; Peng, R.; Liu, Z., Near-Infrared-Triggered Photodynamic Therapy with Multitasking Upconversion Nanoparticles in Combination with Checkpoint Blockade for Immunotherapy of Colorectal Cancer. *ACS Nano* **2017**, 11 (5), 4463-4474.
- 176.Chen, S. X.; Ma, M.; Xue, F. F.; Shen, S. Z.; Chen, Q.; Kuang, Y. C.; Liang, K. C.; Wang, X. L.; Chen, H. R., Construction of microneedle-assisted co-delivery platform and its combining photodynamic/immunotherapy. *J Control Release* **2020**, 324, 218-227.
- 177.Nayak, A.; Hao, Z.; Sadek, R.; Vahanian, N.; Ramsey, W. J.; Kennedy, E.; Mautino, M.; Link, C.; Bourbo, P.; Dobbins, R.; Adams, K.; Diamond, A.; Marshall, L.; Munn, D. H.; Janik, J.; Khleif, S. N., A Phase I study of NLG919 for adult patients with recurrent advanced solid tumors. *J Immunother Cancer* **2014**, 2 (Suppl 3), P250.
- 178.Lin, X.; Xie, J.; Niu, G.; Zhang, F.; Gao, H.; Yang, M.; Quan, Q.; Aronova, M. A.; Zhang, G.; Lee, S.; Leapman, R.; Chen, X., Chimeric ferritin nanocages for multiple function loading and multimodal imaging. *Nano Lett* **2011**, 11 (2), 814-819.
- 179.Liu, X.; Shin, N.; Koblish, H. K.; Yang, G.; Wang, Q.; Wang, K.; Leffet, L.; Hansbury, M. J.; Thomas, B.; Rupar, M.; Waeltz, P.; Bowman, K. J.; Polam, P.; Sparks, R. B.; Yue, E. W.; Li,

- Y.; Wynn, R.; Fridman, J. S.; Burn, T. C.; Combs, A. P.; Newton, R. C.; Scherle, P. A., Selective inhibition of IDO1 effectively regulates mediators of antitumor immunity. *Blood* **2010**, *115* (17), 3520-3530.
- 180.Hou, D. Y.; Muller, A. J.; Sharma, M. D.; DuHadaway, J.; Banerjee, T.; Johnson, M.; Mellor, A. L.; Prendergast, G. C.; Munn, D. H., Inhibition of indoleamine 2,3-dioxygenase in dendritic cells by stereoisomers of 1-methyl-tryptophan correlates with antitumor responses. *Cancer Res* **2007**, *67* (2), 792-801.
- 181.Huang, Y. Y.; Vecchio, D.; Avci, P.; Yin, R.; Garcia-Diaz, M.; Hamblin, M. R., Melanoma resistance to photodynamic therapy: new insights. *Biol Chem* **2013**, *394* (2), 239-250.
- 182.Varela-Eirin, M.; Loureiro, J.; Fonseca, E.; Corrochano, S.; Caeiro, J. R.; Collado, M.; Mayan, M. D., Cartilage regeneration and ageing: Targeting cellular plasticity in osteoarthritis. *Ageing Res Rev* **2018**, *42*, 56-71.
- 183.Roman-Blas, J. A.; Bizzi, E.; Largo, R.; Migliore, A.; Herrero-Beaumont, G., An update on the up and coming therapies to treat osteoarthritis, a multifaceted disease. *Expert Opin Pharmacother* **2016**, *17* (13), 1745-1756.
- 184.Mazzetti, I.; Grigolo, B.; Pulsatelli, L.; Dolzani, P.; Silvestri, T.; Roseti, L.; Meliconi, R.; Facchini, A., Differential roles of nitric oxide and oxygen radicals in chondrocytes affected by osteoarthritis and rheumatoid arthritis. *Clin Sci (Lond)* **2001**, *101* (6), 593-599.
- 185.Lepetsos, P.; Papavassiliou, A. G., ROS/oxidative stress signaling in osteoarthritis. *Biochim Biophys Acta* **2016**, *1862* (4), 576-591.
- 186.Erturk, C.; Altay, M. A.; Selek, S.; Kocyigit, A., Paraoxonase-1 activity and oxidative status in patients with knee osteoarthritis and their relationship with radiological and clinical parameters. *Scand J Clin Lab Invest* **2012**, *72* (5), 433-439.

187. Altindag, O.; Erel, O.; Aksoy, N.; Selek, S.; Celik, H.; Karaoglanoglu, M., Increased oxidative stress and its relation with collagen metabolism in knee osteoarthritis. *Rheumatol Int* **2007**, *27* (4), 339-344.
188. Lim, H. D.; Kim, Y. S.; Ko, S. H.; Yoon, I. J.; Cho, S. G.; Chun, Y. H.; Choi, B. J.; Kim, E. C., Cytoprotective and anti-inflammatory effects of melatonin in hydrogen peroxide-stimulated CHON-001 human chondrocyte cell line and rabbit model of osteoarthritis via the SIRT1 pathway. *J Pineal Res* **2012**, *53* (3), 225-237.
189. Schreck, R.; Rieber, P.; Baeuerle, P. A., Reactive oxygen intermediates as apparently widely used messengers in the activation of the NF-kappa B transcription factor and HIV-1. *EMBO J* **1991**, *10* (8), 2247-2258.
190. Kim, M. J.; Lee, Y.; Jon, S.; Lee, D. Y., PEGylated bilirubin nanoparticle as an anti-oxidative and anti-inflammatory demulcent in pancreatic islet xenotransplantation. *Biomaterials* **2017**, *133*, 242-252.
191. Yin, T.; Yang, L.; Liu, Y.; Zhou, X.; Sun, J.; Liu, J., Sialic acid (SA)-modified selenium nanoparticles coated with a high blood-brain barrier permeability peptide-B6 peptide for potential use in Alzheimer's disease. *Acta Biomater* **2015**, *25*, 172-183.
192. Li, J.; Zhang, J.; Chen, Y.; Kawazoe, N.; Chen, G., TEMPO-Conjugated Gold Nanoparticles for Reactive Oxygen Species Scavenging and Regulation of Stem Cell Differentiation. *ACS Appl Mater Interfaces* **2017**, *9* (41), 35683-35692.
193. Liu, Y.; Ai, K.; Liu, J.; Deng, M.; He, Y.; Lu, L., Dopamine-melanin colloidal nanospheres: an efficient near-infrared photothermal therapeutic agent for in vivo cancer therapy. *Adv Mater* **2013**, *25* (9), 1353-1359.
194. Liu, Y.; Ai, K.; Ji, X.; Askhatova, D.; Du, R.; Lu, L.; Shi, J., Comprehensive Insights into the

- Multi-Antioxidative Mechanisms of Melanin Nanoparticles and Their Application To Protect Brain from Injury in Ischemic Stroke. *J Am Chem Soc* **2017**, *139* (2), 856-862.
- 195.Rageh, M. M.; El-Gebaly, R. H.; Abou-Shady, H.; Amin, D. G., Melanin nanoparticles (MNPs) provide protection against whole-body -irradiation in mice via restoration of hematopoietic tissues. *Mol Cell Biochem* **2015**, *399* (1-2), 59-69.
- 196.Adams, M. E.; Billingham, M. E.; Muir, H., The glycosaminoglycans in menisci in experimental and natural osteoarthritis. *Arthritis Rheum* **1983**, *26* (1), 69-76.
- 197.Mi, B.; Wang, J.; Liu, Y.; Liu, J.; Hu, L.; Panayi, A. C.; Liu, G.; Zhou, W., Icariin Activates Autophagy via Down-Regulation of the NF-kappaB Signaling-Mediated Apoptosis in Chondrocytes. *Front Pharmacol* **2018**, *9*, 605.
- 198.Goutas, A.; Syrrou, C.; Papathanasiou, I.; Tsezou, A.; Trachana, V., The autophagic response to oxidative stress in osteoarthritic chondrocytes is deregulated. *Free Radic Biol Med* **2018**, *126*, 122-132.
- 199.Koskenkorva-Frank, T. S.; Weiss, G.; Koppenol, W. H.; Burckhardt, S., The complex interplay of iron metabolism, reactive oxygen species, and reactive nitrogen species: insights into the potential of various iron therapies to induce oxidative and nitrosative stress. *Free Radic Biol Med* **2013**, *65*, 1174-1194.
- 200.Henrotin, Y. E.; Bruckner, P.; Pujol, J. P., The role of reactive oxygen species in homeostasis and degradation of cartilage. *Osteoarthritis Cartilage* **2003**, *11* (10), 747-755.
- 201.Nemirovskiy, O. V.; Radabaugh, M. R.; Aggarwal, P.; Funckes-Shippy, C. L.; Mnich, S. J.; Meyer, D. M.; Sunyer, T.; Rodney Mathews, W.; Misko, T. P., Plasma 3-nitrotyrosine is a biomarker in animal models of arthritis: Pharmacological dissection of iNOS' role in disease. *Nitric Oxide* **2009**, *20* (3), 150-156.

- 202.Ersoy, Y.; Ozerol, E.; Baysal, O.; Temel, I.; MacWalter, R. S.; Meral, U.; Altay, Z. E., Serum nitrate and nitrite levels in patients with rheumatoid arthritis, ankylosing spondylitis, and osteoarthritis. *Ann Rheum Dis* **2002**, *61* (1), 76-78.
- 203.Sakurai, H.; Kohsaka, H.; Liu, M. F.; Higashiyama, H.; Hirata, Y.; Kanno, K.; Saito, I.; Miyasaka, N., Nitric oxide production and inducible nitric oxide synthase expression in inflammatory arthritides. *J Clin Invest* **1995**, *96* (5), 2357-2363.
- 204.Karan, A.; Karan, M. A.; Vural, P.; Erten, N.; Tascioglu, C.; Aksoy, C.; Canbaz, M.; Oncel, A., Synovial fluid nitric oxide levels in patients with knee osteoarthritis. *Clin Rheumatol* **2003**, *22* (6), 397-399.
- 205.Jiang, T.; Kan, H. M.; Rajpura, K.; Carbone, E. J.; Li, Y.; Lo, K. W., Development of Targeted Nanoscale Drug Delivery System for Osteoarthritic Cartilage Tissue. *J Nanosci Nanotechnol* **2018**, *18* (4), 2310-2317.
- 206.Jain, A.; Mishra, S. K.; Vuddanda, P. R.; Singh, S. K.; Singh, R.; Singh, S., Targeting of diacerein loaded lipid nanoparticles to intra-articular cartilage using chondroitin sulfate as homing carrier for treatment of osteoarthritis in rats. *Nanomedicine* **2014**, *10* (5), 1031-1040.
- 207.Zhong, L.; Schivo, S.; Huang, X.; Leijten, J.; Karperien, M.; Post, J. N., Nitric Oxide Mediates Crosstalk between Interleukin 1beta and WNT Signaling in Primary Human Chondrocytes by Reducing DKK1 and FRZB Expression. *Int J Mol Sci* **2017**, *18* (11), 2491.
- 208.Bentz, M.; Zaouter, C.; Shi, Q.; Fahmi, H.; Moldovan, F.; Fernandes, J. C.; Benderdour, M., Inhibition of inducible nitric oxide synthase prevents lipid peroxidation in osteoarthritic chondrocytes. *J Cell Biochem* **2012**, *113* (7), 2256-2267.
- 209.Salerno, L.; Sorrenti, V.; Di Giacomo, C.; Romeo, G.; Siracusa, M. A., Progress in the development of selective nitric oxide synthase (NOS) inhibitors. *Curr Pharm Des* **2002**, *8* (3),

177-200.

210. Jacobson, E. S., Pathogenic roles for fungal melanins. *Clin Microbiol Rev* **2000**, *13* (4), 708-717.
211. Liu, Y.; Ai, K.; Ji, X.; Askhatova, D.; Du, R.; Lu, L.; Shi, J., Comprehensive Insights into the Multi-Antioxidative Mechanisms of Melanin Nanoparticles and Their Application To Protect Brain from Injury in Ischemic Stroke. *J Am Chem Soc* **2017**, *139* (2), 856-862.
212. Park, S.; Geddes, T. J.; Javitch, J. A.; Kuhn, D. M., Dopamine prevents nitration of tyrosine hydroxylase by peroxynitrite and nitrogen dioxide: is nitrotyrosine formation an early step in dopamine neuronal damage? *J Biol Chem* **2003**, *278* (31), 28736-28742.
213. Yoshioka, Y.; Sugino, Y.; Tozawa, A.; Yamamuro, A.; Kasai, A.; Ishimaru, Y.; Maeda, S., Dopamine inhibits lipopolysaccharide-induced nitric oxide production through the formation of dopamine quinone in murine microglia BV-2 cells. *J Pharmacol Sci* **2016**, *130* (2), 51-59.
214. O'Brian, C. A.; Chu, F., Post-translational disulfide modifications in cell signaling--role of inter-protein, intra-protein, S-glutathionyl, and S-cysteaminy disulfide modifications in signal transmission. *Free Radic Res* **2005**, *39* (5), 471-480.
215. Starkman, B. G.; Cravero, J. D.; Delcarlo, M.; Loeser, R. F., IGF-I stimulation of proteoglycan synthesis by chondrocytes requires activation of the PI 3-kinase pathway but not ERK MAPK. *Biochem J* **2005**, *389* (Pt 3), 723-729.
216. Yin, W.; Park, J. I.; Loeser, R. F., Oxidative stress inhibits insulin-like growth factor-I induction of chondrocyte proteoglycan synthesis through differential regulation of phosphatidylinositol 3-Kinase-Akt and MEK-ERK MAPK signaling pathways. *J Biol Chem* **2009**, *284* (46), 31972-31981.
217. Poole, L. B.; Karplus, P. A.; Claiborne, A., Protein sulfenic acids in redox signaling. *Annu Rev*

Pharmacol Toxicol **2004**, *44*, 325-347.

- 218.Hosseinzadeh, A.; Kamrava, S. K.; Joghataei, M. T.; Darabi, R.; Shakeri-Zadeh, A.; Shahriari, M.; Reiter, R. J.; Ghaznavi, H.; Mehrzadi, S., Apoptosis signaling pathways in osteoarthritis and possible protective role of melatonin. *J Pineal Res* **2016**, *61* (4), 411-425.
- 219.Frudd, K.; Burgoyne, T.; Burgoyne, J. R., Oxidation of Atg3 and Atg7 mediates inhibition of autophagy. *Nat Commun* **2018**, *9* (1), 95.
- 220.Chang, J.; Wang, W.; Zhang, H.; Hu, Y.; Wang, M.; Yin, Z., The dual role of autophagy in chondrocyte responses in the pathogenesis of articular cartilage degeneration in osteoarthritis. *Int J Mol Med* **2013**, *32* (6), 1311-1318.
- 221.Sasaki, H.; Takayama, K.; Matsushita, T.; Ishida, K.; Kubo, S.; Matsumoto, T.; Fujita, N.; Oka, S.; Kurosaka, M.; Kuroda, R., Autophagy modulates osteoarthritis-related gene expression in human chondrocytes. *Arthritis Rheum* **2012**, *64* (6), 1920-1928.
- 222.Shen, C.; Yan, J.; Erkocak, O. F.; Zheng, X. F.; Chen, X. D., Nitric oxide inhibits autophagy via suppression of JNK in meniscal cells. *Rheumatology (Oxford)* **2014**, *53* (6), 1022-1033.
- 223.Shen, C.; Cai, G. Q.; Peng, J. P.; Chen, X. D., Autophagy protects chondrocytes from glucocorticoids-induced apoptosis via ROS/Akt/FOXO3 signaling. *Osteoarthritis Cartilage* **2015**, *23* (12), 2279-2287.
- 224.Sun, M. M.; Beier, F.; Pest, M. A., Recent developments in emerging therapeutic targets of osteoarthritis. *Curr Opin Rheumatol* **2017**, *29* (1), 96-102.
- 225.Morales, C. R.; Pedrozo, Z.; Lavandero, S.; Hill, J. A., Oxidative stress and autophagy in cardiovascular homeostasis. *Antioxid Redox Signal* **2014**, *20* (3), 507-518.
- 226.Sarkar, S.; Korolchuk, V. I.; Renna, M.; Imarisio, S.; Fleming, A.; Williams, A.; Garcia-Arencibia, M.; Rose, C.; Luo, S.; Underwood, B. R.; Kroemer, G.; O'Kane, C. J.; Rubinsztein,

- D. C., Complex inhibitory effects of nitric oxide on autophagy. *Mol Cell* **2011**, *43* (1), 19-32.
- 227.Wang, D.; Ji, X.; Liu, J.; Li, Z.; Zhang, X., Dopamine Receptor Subtypes Differentially Regulate Autophagy. *Int J Mol Sci* **2018**, *19* (5), 1540.
- 228.Gimenez-Xavier, P.; Francisco, R.; Santidrian, A. F.; Gil, J.; Ambrosio, S., Effects of dopamine on LC3-II activation as a marker of autophagy in a neuroblastoma cell model. *Neurotoxicology* **2009**, *30* (4), 658-665.
- 229.Halliwell, B.; Gutteridge, J. M.; Aruoma, O. I., The deoxyribose method: a simple "test-tube" assay for determination of rate constants for reactions of hydroxyl radicals. *Anal Biochem* **1987**, *165* (1), 215-219.
- 230.Brand-Williams, W.; Cuvelier, M.; Berset, C., Use of a free radical method to evaluate antioxidant activity. *Lwt Food Sci Technol* **1995**, *28* (1), 25-30.
- 231.McCord, J. M.; Fridovich, I., Superoxide dismutase. An enzymic function for erythrocuprein (hemocuprein). *J Biol Chem* **1969**, *244* (22), 6049-6055.
- 232.Meng, F.; He, A.; Zhang, Z.; Zhang, Z.; Lin, Z.; Yang, Z.; Long, Y.; Wu, G.; Kang, Y.; Liao, W., Chondrogenic differentiation of ATDC5 and hMSCs could be induced by a novel scaffold-tricalcium phosphate-collagen-hyaluronan without any exogenous growth factors in vitro. *J Biomed Mater Res A* **2014**, *102* (8), 2725-2735.
- 233.Jiang, Y.; Chen, L. K.; Zhu, D. C.; Zhang, G. R. Guo, C.; Qi, Y. Y.; Ouyang, H. W., The inductive effect of bone morphogenetic protein-4 on chondral-lineage differentiation and in situ cartilage repair. *Tissue Eng Part A* **2010**, *16* (5), 1621-1632.
- 234.Benjamin, E. J.; Muntner, P.; Alonso, A.; Bittencourt, M. S.; Callaway, C. W.; Carson, A. P.;Chamberlain, A. M.; Chang, A. R.; Cheng, S.; Das, S. R.; Delling, F. N.; Djousse, L.; Elkind, M. S. V.; Ferguson, J. F.; Fornage, M.; Jordan, L. C.; Khan, S. S.; Kissela, B. M.; Knutson, K.

- L.; Kwan, T. W.; Lackland, D. T.; Lewis, T. T.; Lichtman, J. H.; Longenecker, C. T.; Loop, M. S.; Lutsey, P. L.; Martin, S. S.; Matsushita, K.; Moran, A. E.; Mussolino, M. E.; O'Flaherty, M.; Pandey, A.; Perak, A. M.; Rosamond, W. D.; Roth, G. A.; Sampson, U. K. A.; Satou, G. M.; Schroeder, E. B.; Shah, S. H.; Spartano, N. L.; Stokes, A.; Tirschwell, D. L.; Tsao, C. W.; Turakhia, M. P.; VanWagner, L. B.; Wilkins, J. T.; Wong, S. S.; Virani, S. S.; American Heart Association Council on, E.; Prevention Statistics, C.; Stroke Statistics, S., Heart Disease and Stroke Statistics-2019 Update: A Report From the American Heart Association. *Circulation* **2019**, *139* (10), e56-e528.
235. Jilani, T. N.; Siddiqui, A. H., Tissue Plasminogen Activator. In *StatPearls*, Treasure Island (FL), 2020.
236. Durukan, A.; Tatlisumak, T., Acute ischemic stroke: overview of major experimental rodent models, pathophysiology, and therapy of focal cerebral ischemia. *Pharmacol Biochem Behav* **2007**, *87* (1), 179-197.
237. Han, J. Y.; Fan, J. Y.; Horie, Y.; Miura, S.; Cui, D. H.; Ishii, H.; Hibi, T.; Tsuneki, H.; Kimura, I., Ameliorating effects of compounds derived from *Salvia miltiorrhiza* root extract on microcirculatory disturbance and target organ injury by ischemia and reperfusion. *Pharmacol Ther* **2008**, *117* (2), 280-295.
238. Chen, H. S.; Qi, S. H.; Shen, J. G., One-Compound-Multi-Target: Combination Prospect of Natural Compounds with Thrombolytic Therapy in Acute Ischemic Stroke. *Curr Neuropharmacol* **2017**, *15* (1), 134-156.
239. Zhang, B.; Wang, B.; Cao, S.; Wang, Y., Epigallocatechin-3-Gallate (EGCG) Attenuates Traumatic Brain Injury by Inhibition of Edema Formation and Oxidative Stress. *Korean J Physiol Pharmacol* **2015**, *19* (6), 491-497.

- 240.Chen, J.; Bi, Y.; Chen, L.; Zhang, Q.; Xu, L., Tanshinone IIA exerts neuroprotective effects on hippocampus-dependent cognitive impairments in diabetic rats by attenuating ER stress-induced apoptosis. *Biomed Pharmacother* **2018**, *104*, 530-536.
- 241.Maione, F.; Piccolo, M.; De Vita, S. Chini, M. G.; Cristiano, C.; De Caro, C. Lippiello, P. Miniaci, M. C.; Santamaria, R.; Irace, C.; De Feo, V.; Calignano, A.; Mascolo, N.; Bifulco, G., Down regulation of pro-inflammatory pathways by tanshinone IIA and cryptotanshinone in a non-genetic mouse model of Alzheimer's disease. *Pharmacol Res* **2018**, *129*, 482-490.
- 242.Huang, Y.; Long, X.; Tang, J.; Li, X.; Zhang, X.; Luo, C.; Zhou, Y.; Zhang, P., The Attenuation of Traumatic Brain Injury via Inhibition of Oxidative Stress and Apoptosis by Tanshinone IIA. *Oxid Med Cell Longev* **2020**, *2020*, 4170156.
- 243.Lam, B. Y.; Lo, A. C.; Sun, X.; Luo, H. W.; Chung, S. K.; Sucher, N. J., Neuroprotective effects of tanshinones in transient focal cerebral ischemia in mice. *Phytomedicine* **2003**, *10* (4), 286-291.
- 244.Tang, C.; Xue, H.; Bai, C.; Fu, R.; Wu, A., The effects of Tanshinone IIA on blood-brain barrier and brain edema after transient middle cerebral artery occlusion in rats. *Phytomedicine* **2010**, *17* (14), 1145-1149.
- 245.Sze, F. K.; Yeung, F. F.; Wong, E.; Lau, J., Does Danshen improve disability after acute ischaemic stroke? *Acta Neurol Scand* **2005**, *111* (2), 118-125
- 246.Wu, B.; Liu, M.; Zhang, S., Dan Shen agents for acute ischaemic stroke. *Cochrane Database Syst Rev* **2007**, (2), CD004295.
- 247.Danhier, F.; Ansorena, E.; Silva, J. M.; Coco, R.; Le Breton, A.; Preat, V., PLGA-based nanoparticles: an overview of biomedical applications. *J Control Release* **2012**, *161* (2), 505-522.

- 248.Cai, B.; Wang, N., Large Animal Stroke Models vs. Rodent Stroke Models, Pros and Cons, and Combination? *Acta Neurochir Suppl* **2016**, *121*, 77-81.
- 249.Kaur, H.; Prakash, A.; Medhi, B., Drug therapy in stroke: from preclinical to clinical studies. *Pharmacology* **2013**, *92* (5-6), 324-334.
- 250.Stroke Therapy Academic Industry, R., Recommendations for standards regarding preclinical neuroprotective and restorative drug development. *Stroke* **1999**, *30* (12), 2752-2758.
- 251.Baker, E. W.; Platt, S. R.; Lau, V. W.; Grace, H. E.; Holmes, S. P.; Wang, L.; Duberstein, K. J.; Howerth, E. W.; Kinder, H. A.; Stice, S. L.; Hess, D. C.; Mao, H.; West, F. D., Induced Pluripotent Stem Cell-Derived Neural Stem Cell Therapy Enhances Recovery in an Ischemic Stroke Pig Model. *Sci Rep* **2017**, *7* (1), 10075.
- 252.Endres, M.; Dirnagl, U.; Moskowitz, M. A., The ischemic cascade and mediators of ischemic injury. *Handb Clin Neurol* **2009**, *92*, 31-41.
- 253.Bernstock, J. D.; Peruzzotti-Jametti, L.; Ye, D.; Gessler, F. A.; Maric, D.; Vicario, N.; Lee, Y. J.; Pluchino, S.; Hallenbeck, J. M., Neural stem cell transplantation in ischemic stroke: A role for preconditioning and cellular engineering. *J Cereb Blood Flow Metab* **2017**, *37* (7), 2314-2319.
- 254.Dirnagl, U.; Iadecola, C.; Moskowitz, M. A., Pathobiology of ischaemic stroke: an integrated view. *Trends Neurosci* **1999**, *22* (9), 391-397.
- 255.Rothwell, N. J.; Hopkins, S. J., Cytokines and the nervous system II: Actions and mechanisms of action. *Trends Neurosci* **1995**, *18* (3), 130-136.
- 256.Tang, Q.; Han, R.; Xiao, H.; Li, J.; Shen, J.; Luo, Q., Protective effect of tanshinone IIA on the brain and its therapeutic time window in rat models of cerebral ischemia-reperfusion. *Exp Ther Med* **2014**, *8* (5), 1616-1622.

- 257.Zhou, L.; Zuo, Z.; Chow, M. S., Danshen: an overview of its chemistry, pharmacology, pharmacokinetics, and clinical use. *J Clin Pharmacol* **2005**, *45* (12), 1345-1359.
- 258.Chen, X.; Zhou, Z. W.; Xue, C. C.; Li, X. X.; Zhou, S. F., Role of P-glycoprotein in restricting the brain penetration of tanshinone IIA, a major active constituent from the root of *Salvia miltiorrhiza* Bunge, across the blood-brain barrier. *Xenobiotica* **2007**, *37* (6), 635-678.
- 259.Savjani, K. T.; Gajjar, A. K.; Savjani, J. K., Drug solubility: importance and enhancement techniques. *ISRN Pharm* **2012**, *2012*, 195727.
- 260.Locatelli, E.; Comes Franchini, M., Biodegradable PLGA-b-PEG polymeric nanoparticles: synthesis, properties, and nanomedical applications as drug delivery system. *J Nanopart Res* **2012**, *14* (12), 1316.
- 261.Govender, T.; Stolnik, S.; Garnett, M. C.; Illum, L.; Davis, S. S., PLGA nanoparticles prepared by nanoprecipitation: drug loading and release studies of a water soluble drug. *J Control Release* **1999**, *57* (2), 171-185.
- 262.Lind, N. M.; Moustgaard, A.; Jelsing, J.; Vajta, G.; Cumming, P.; Hansen, A. K., The use of pigs in neuroscience: modeling brain disorders. *Neurosci Biobehav Rev* **2007**, *31* (5), 728-751.
- 263.Nakamura, M.; Imai, H.; Konno, K.; Kubota, C.; Seki, K.; Puentes, S.; Faried, A.; Yokoo, H.; Hata, H.; Yoshimoto, Y.; Saito, N., Experimental investigation of encephalomyosynangiosis using gyrencephalic brain of the miniature pig: histopathological evaluation of dynamic reconstruction of vessels for functional anastomosis. Laboratory investigation. *J Neurosurg Pediatr* **2009**, *3* (6), 488-495.
- 264.McKay, S. M.; Brooks, D. J.; Hu, P.; McLachlan, E. M., Distinct types of microglial activation in white and grey matter of rat lumbosacral cord after mid-thoracic spinal transection. *J Neuropathol Exp Neurol* **2007**, *66* (8), 698-710.

265. Baltan, S.; Besancon, E. F.; Mbow, B.; Ye, Z.; Hamner, M. A.; Ransom, B. R., White matter vulnerability to ischemic injury increases with age because of enhanced excitotoxicity. *J Neurosci* **2008**, *28* (6), 1479-1489.
266. Mallucci, G.; Peruzzotti-Jametti, L.; Bernstock, J. D.; Pluchino, S., The role of immune cells, glia and neurons in white and gray matter pathology in multiple sclerosis. *Prog Neurobiol* **2015**, *127-128*, 1-22.
267. Fern, R.; Waxman, S. G.; Ransom, B. R., Modulation of anoxic injury in CNS white matter by adenosine and interaction between adenosine and GABA. *J Neurophysiol* **1994**, *72* (6), 2609-2616.
268. Tu, X. K.; Yang, W. Z.; Liang, R. S.; Shi, S. S.; Chen, J. P.; Chen, C. M.; Wang, C. H.; Xie, H. S.; Chen, Y.; Ouyang, L. Q., Effect of baicalin on matrix metalloproteinase-9 expression and blood-brain barrier permeability following focal cerebral ischemia in rats. *Neurochem Res* **2011**, *36* (11), 2022-2028.
269. Tu, X. K.; Yang, W. Z.; Shi, S. S.; Wang, C. H.; Chen, C. M., Neuroprotective effect of baicalin in a rat model of permanent focal cerebral ischemia. *Neurochem Res* **2009**, *34* (9), 1626-1634.
270. Yaghi, S.; Furie, K. L.; Viscoli, C. M.; Kamel, H.; Gorman, M.; Dearborn, J.; Young, L. H.; Inzucchi, S. E.; Lovejoy, A. M.; Kasner, S. E.; Conwit, R.; Kernan, W. N.; Investigators, I. T., Pioglitazone Prevents Stroke in Patients With a Recent Transient Ischemic Attack or Ischemic Stroke: A Planned Secondary Analysis of the IRIS Trial (Insulin Resistance Intervention After Stroke). *Circulation* **2018**, *137* (5), 455-463.
271. Blankenship, D.; Niemi, J.; Hilow, E.; Karl, M.; Sundararajan, S., Oral pioglitazone reduces infarction volume and improves neurologic function following MCAO in rats. *Adv Exp Med Biol* **2011**, *701*, 157-62.

- 272.Chang, Y.; Hsieh, C. Y.; Peng, Z. A.; Yen, T. L.; Hsiao, G.; Chou, D. S.; Chen, C. M.; Sheu, J. R., Neuroprotective mechanisms of puerarin in middle cerebral artery occlusion-induced brain infarction in rats. *J Biomed Sci* **2009**, *16* (1), 9.
- 273.Zheng, Q. H.; Li, X. L.; Mei, Z. G.; Xiong, L.; Mei, Q. X.; Wang, J. F.; Tan, L. J.; Yang, S. B.; Feng, Z. T., Efficacy and safety of puerarin injection in curing acute ischemic stroke: A meta-analysis of randomized controlled trials. *Medicine (Baltimore)* **2017**, *96* (1), e5803.
- 274.Kobayashi, S.; Fukuma, S.; Ikenoue, T.; Fukuhara, S.; Kobayashi, S., Effect of Edoxaban on Neurological Symptoms in Real-World Patients With Acute Ischemic Stroke. *Stroke* **2019**, *50* (7), 1805-1811.
- 275.Lee, X. R.; Xiang, G. L., Effects of edoxaban, the free radical scavenger, on outcomes in acute cerebral infarction patients treated with ultra-early thrombolysis of recombinant tissue plasminogen activator. *Clin Neurol Neurosurg* **2018**, *167*, 157-161.
- 276.Koronowski, K. B.; Khoury, N.; Saul, I.; Loris, Z. B.; Cohan, C. H.; Stradecki-Cohan, H. M.; Dave, K. R.; Young, J. I.; Perez-Pinzon, M. A., Neuronal SIRT1 (Silent Information Regulator 2 Homologue 1) Regulates Glycolysis and Mediates Resveratrol-Induced Ischemic Tolerance. *Stroke* **2017**, *48* (11), 3117-3125.
- 277.Liang, W.; Huang, X. B.; Chen, W. Q., The Effects of Baicalin and Baicalein on Cerebral Ischemia: A Review. *Aging Dis* **2017**, *8* (6), 850-867.
- 278.Shang, Y. H.; Tian, J. F.; Hou, M.; Xu, X. Y., Progress on the protective effect of compounds from natural medicines on cerebral ischemia. *Chin J Nat Medicines* **2013**, *11* (6), 588-595.
- 279.Falcao, A. L.; Reutens, D. C.; Markus, R.; Koga, M.; Read, S. J.; Tochon-Danguy, H.; Sachinidis, J.; Howells, D. W.; Donnan, G. A., The resistance to ischemia of white and gray matter after stroke. *Ann Neurol* **2004**, *56* (5), 695-701.

280. Berrouschot, J.; Sterker, M.; Bettin, S.; Koster, J.; Schneider, D., Mortality of space-occupying ('malignant') middle cerebral artery infarction under conservative intensive care. *Intensive Care Med* **1998**, *24* (6), 620-623.
281. Hacke, W.; Schwab, S.; Horn, M.; Spranger, M.; De Georgia, M.; von Kummer, R., 'Malignant' middle cerebral artery territory infarction: clinical course and prognostic signs. *Arch Neurol* **1996**, *53* (4), 309-315.
282. Hsu, A. L.; Tang, P. F.; Jan, M. H., Analysis of impairments influencing gait velocity and asymmetry of hemiplegic patients after mild to moderate stroke. *Arch Phys Med Rehabil* **2003**, *84* (8), 1185-1193.
283. Balaban, B.; Tok, F., Gait disturbances in patients with stroke. *PM R* **2014**, *6* (7), 635-642.
284. Householder, K. T.; Dharmaraj, S.; Sandberg, D. I.; Wechsler-Reya, R. J.; Sirianni, R. W., Fate of nanoparticles in the central nervous system after intrathecal injection in healthy mice. *Sci Rep* **2019**, *9* (1), 12587.
285. Thrift, A. G.; Dewey, H. M.; Macdonell, R. A.; McNeil, J. J.; Donnan, G. A., Stroke incidence on the east coast of Australia: the North East Melbourne Stroke Incidence Study (NEMESIS). *Stroke* **2000**, *31* (9), 2087-2092.
286. Liu, L.; Zhang, X.; Wang, L.; Yang, R.; Cui, L.; Li, M.; Du, W.; Wang, S., The neuroprotective effects of Tanshinone IIA are associated with induced nuclear translocation of TORC1 and upregulated expression of TORC1, pCREB and BDNF in the acute stage of ischemic stroke. *Brain Res Bull* **2010**, *82* (3-4), 228-233.
287. Wang, L.; Zhang, X.; Liu, L.; Cui, L.; Yang, R.; Li, M.; Du, W., Tanshinone II A down-regulates HMGB1, RAGE, TLR4, NF-kappaB expression, ameliorates BBB permeability and endothelial cell function, and protects rat brains against focal ischemia. *Brain Res* **2010**, *1321*,

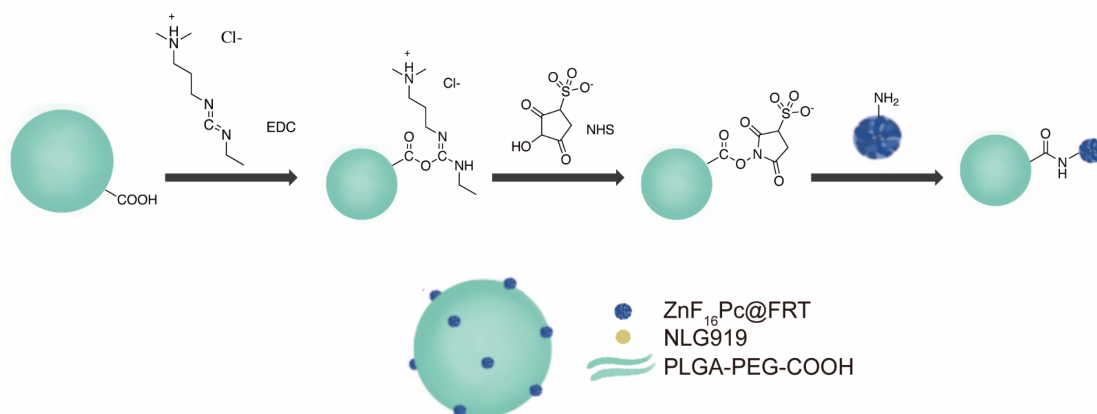
143-51.

288. Terruso, V.; D'Amelio, M.; Di Benedetto, N.; Lupo, I.; Saia, V.; Famoso, G.; Mazzola, M. A.; Aridon, P.; Sarno, C.; Ragonese, P.; Savettieri, G., Frequency and determinants for hemorrhagic transformation of cerebral infarction. *Neuroepidemiology* **2009**, *33* (3), 261-265.
289. Beslow, L. A.; Smith, S. E.; Vossough, A.; Licht, D. J.; Kasner, S. E.; Favilla, C. G.; Halperin, A. R.; Gordon, D. M.; Jones, C. I.; Cucchiara, A. J.; Ichord, R. N., Hemorrhagic transformation of childhood arterial ischemic stroke. *Stroke* **2011**, *42* (4), 941-946.
290. Ma, J.; Hou, D.; Wei, Z.; Zhu, J.; Lu, H.; Li, Z.; Wang, X.; Li, Y.; Qiao, G.; Liu, N., Tanshinone IIA attenuates cerebral aneurysm formation by inhibiting the NFkappaB-mediated inflammatory response. *Mol Med Rep* **2019**, *20* (2), 1621-1628.
291. Zhou, Z. Y.; Huang, B.; Li, S.; Huang, X. H.; Tang, J. Y.; Kwan, Y. W.; Hoi, P. M.; Lee, S. M., Sodium tanshinone IIA sulfonate promotes endothelial integrity via regulating VE-cadherin dynamics and RhoA/ROCK-mediated cellular contractility and prevents atorvastatin-induced intracerebral hemorrhage in zebrafish. *Toxicol Appl Pharmacol* **2018**, *350*, 32-42.
292. Cress, R. H.; Fleming, W. C., Treatment goals and selection of patients for rehabilitation with hemiplegia. *Ala J Med Sci* **1966**, *3* (3), 307-311.
293. Duberstein, K. J.; Platt, S. R.; Holmes, S. P.; Dove, C. R.; Howerth, E. W.; Kent, M.; Stice, S. L.; Hill, W. D.; Hess, D. C.; West, F. D., Gait analysis in a pre- and post-ischemic stroke biomedical pig model. *Physiol Behav* **2014**, *125*, 8-16.
294. Baker, E. W.; Kinder, H. A.; Hutcheson, J. M.; Duberstein, K. J. J.; Platt, S. R.; Howerth, E. W.; West, F. D., Controlled Cortical Impact Severity Results in Graded Cellular, Tissue, and Functional Responses in a Piglet Traumatic Brain Injury Model. *J Neurotrauma* **2019**, *36* (1), 61-73.

- 295.Kinder, H. A.; Baker, E. W.; Wang, S.; Fleischer, C. C.; Howerth, E. W.; Duberstein, K. J.; Mao, H.; Platt, S. R.; West, F. D., Traumatic Brain Injury Results in Dynamic Brain Structure Changes Leading to Acute and Chronic Motor Function Deficits in a Pediatric Piglet Model. *J Neurotrauma* **2019**, *36* (20), 2930-2942.
- 296.Chen, Y.; Wu, X.; Yu, S.; Fauzee, N. J.; Wu, J.; Li, L.; Zhao, J.; Zhao, Y., Neuroprotective capabilities of Tanshinone IIA against cerebral ischemia/reperfusion injury via anti-apoptotic pathway in rats. *Biol Pharm Bull* **2012**, *35* (2), 164-170.
- 297.Lapchak, P. A.; Zhang, J. H.; Noble-Haeusslein, L. J., RIGOR guidelines: escalating STAIR and STEPS for effective translational research. *Transl Stroke Res* **2013**, *4* (3), 279-285.
- 298.Platt, S. R.; Holmes, S. P.; Howerth, E. W.; Duberstein, K. J. J.; Dove, C. R.; Kinder, H. A.; Wyatt, E. L.; Linville, A. V.; Lau, V. W.; Stice, S. L.; Hill, W. D.; Hess, D. C.; West, F. D., Development and characterization of a Yucatan miniature biomedical pig permanent middle cerebral artery occlusion stroke model. *Exp Transl Stroke Med* **2014**, *6* (1), 5.

APPENDICES

A Supporting information for Chapter 2



Scheme S2.1: Schematic illustration to show the preparation of PPF NPs.

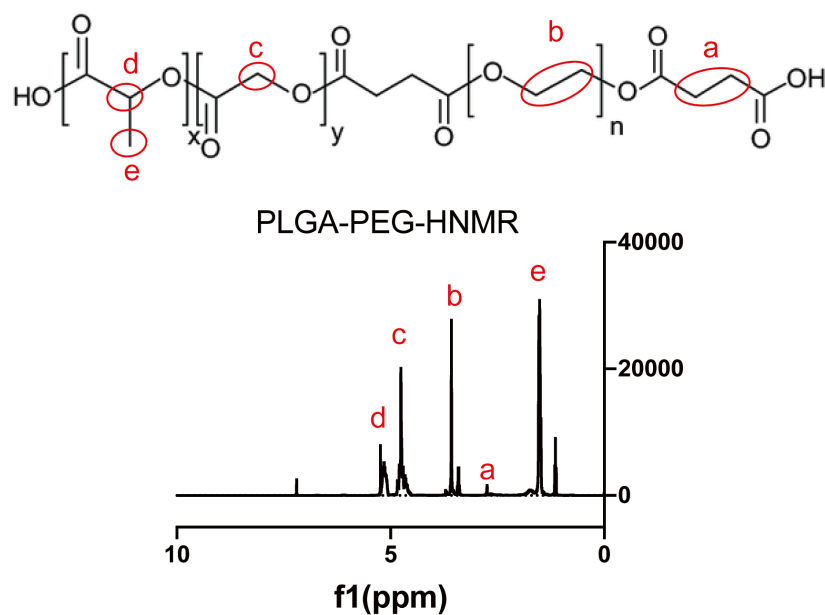


Figure S2.1: ^1H -NMR spectrum of PLGA-*b*-PEG.

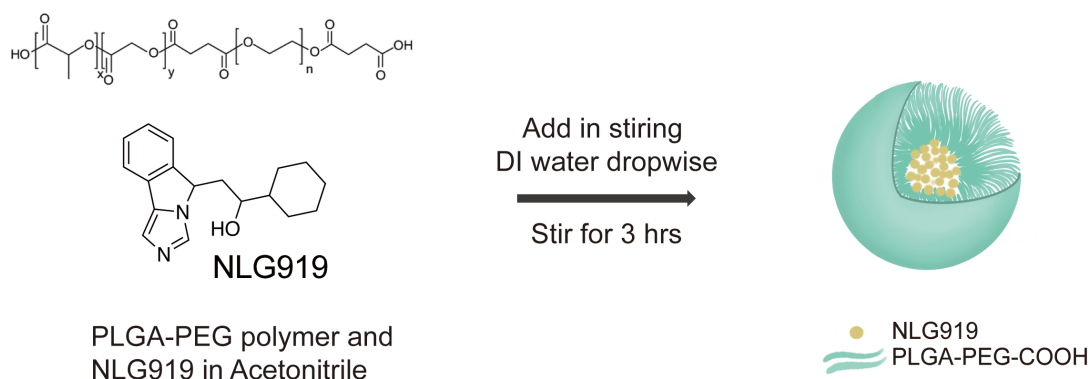


Figure S2.2: Schematic illustration to show the preparation of NLG919@PLGA NPs.

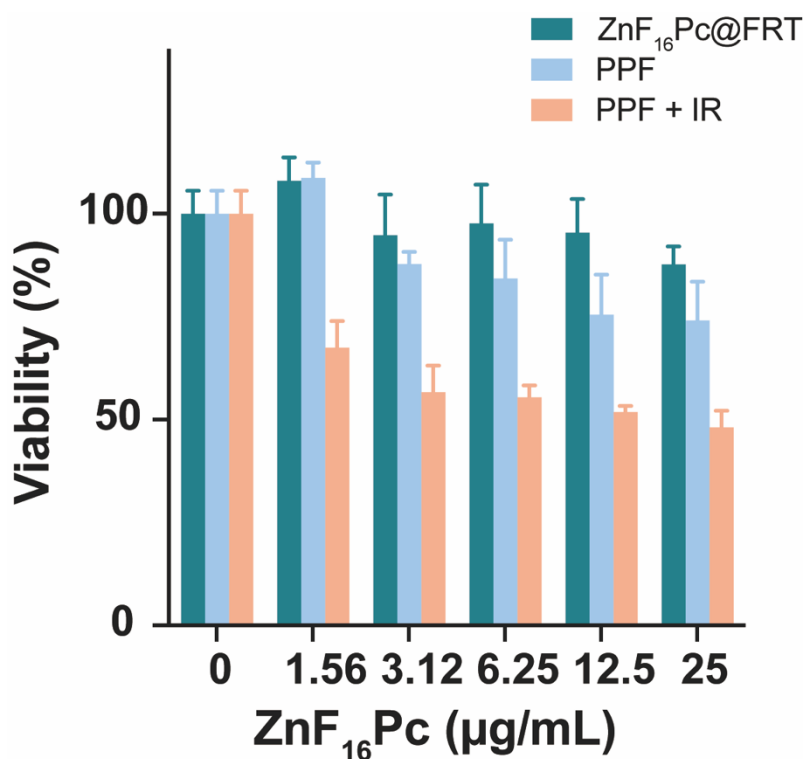


Figure S2.3: Cytotoxicity, measured with B16F10 cells by MTT assays. Cells were incubated with ZnF₁₆Pc@FRT or PPF NPs for 4 h and then irradiated by a 671-nm laser (0.1 W/cm² for 200 s). MTT assays were conducted 12 h later. *, $p < 0.05$; **, $p < 0.01$; ns, no significant difference.

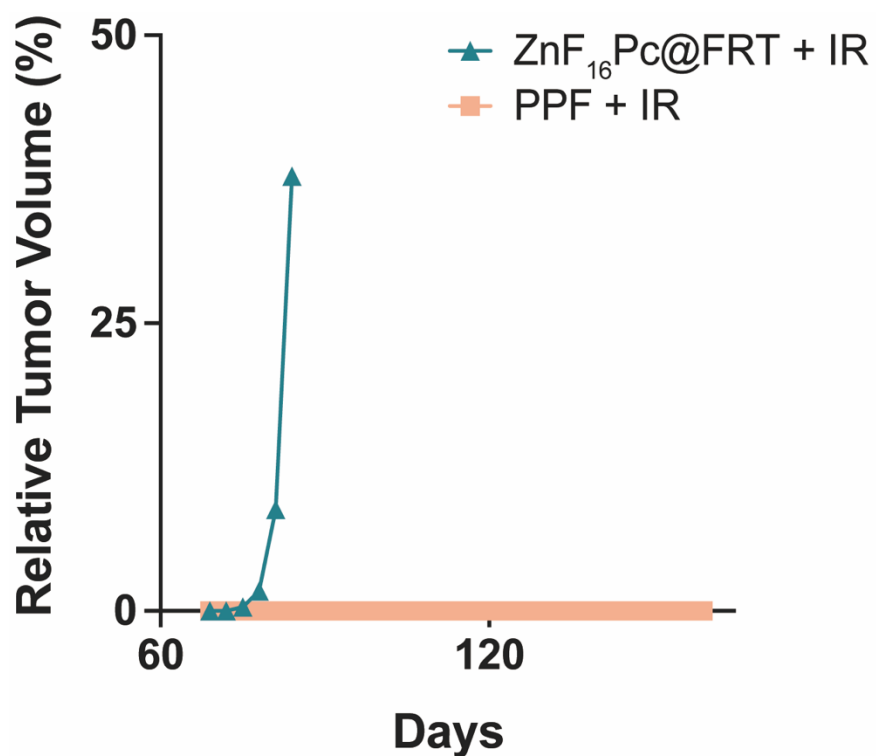


Figure S2.4: Relative tumor volume after live cell re-challenge. B16F10-tumor bearing mice surviving the initial ZnF₁₆Pc@FRT+IR or PPF+IR treatments were inoculated with live B16F10 cancer cells to opposite flank sixty on Day 60.

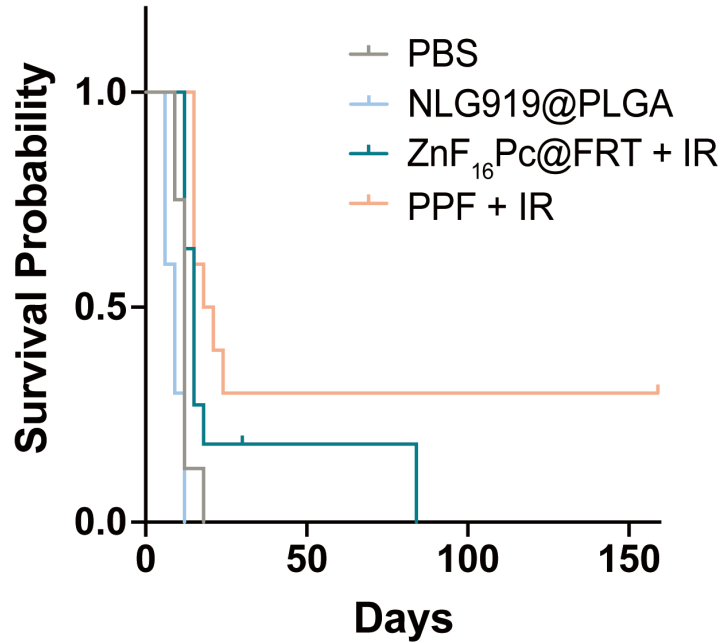


Figure S2.5: Animal survival throughout the experiment, including the re-challenge study.

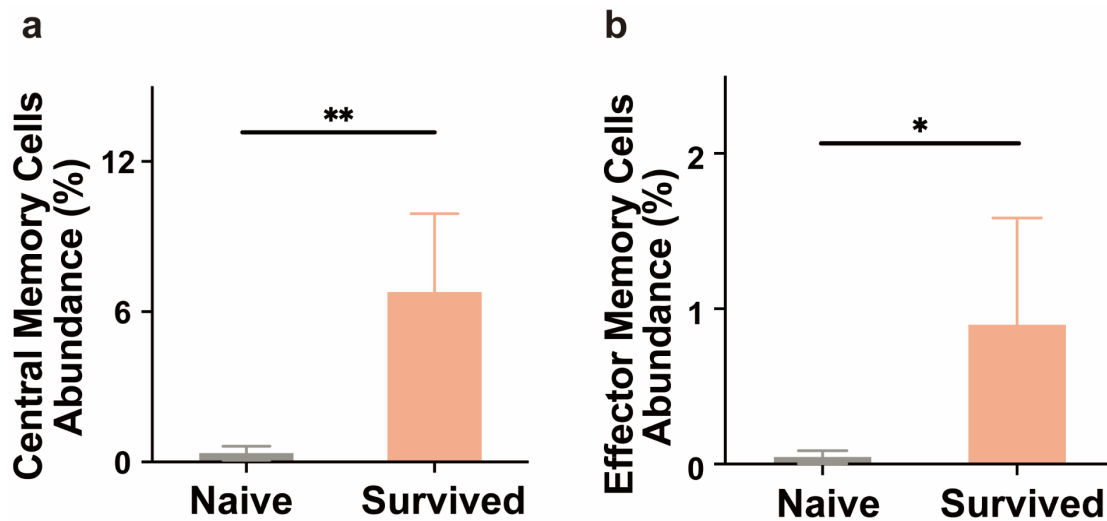


Figure S2.6: a,b) Central (a) and effector (b) memory T cells abundance, based on flow cytometry analysis of spleen tissues taken from animals treated with PPF+IR. * $p < 0.05$, ** $p < 0.01$; $n=3$. Spleen tissues from naïve animals were tested as a comparison.

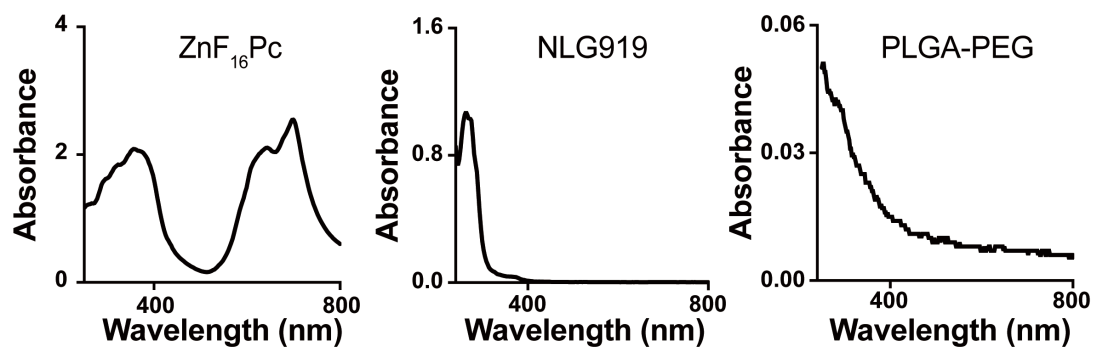


Figure S2.7: Absorbance spectra of ZnF₁₆Pc, NLG919, and PLGA-*b*-PEG in DMSO.

B Supporting information for Chapter 3

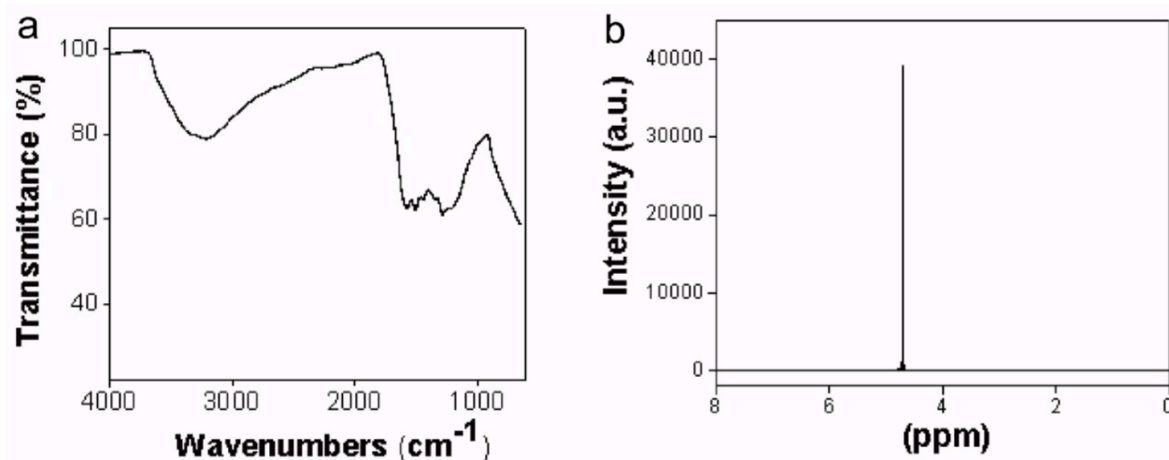


Figure S3.1. (a) FT-IR spectrum of DM nanoparticles. The peak at $\sim 3200\text{ cm}^{-1}$ corresponds to the stretching vibrations of -OH and N-H. The peaks at 1574 cm^{-1} and 1281 cm^{-1} were attributed to the C=O and C-O bonds, respectively. The peak at 1442 cm^{-1} corresponds to C=C. (b) ^1H NMR spectrum of DM nanoparticles. The peak at $\sim 4.7\text{ ppm}$ in the ^1H NMR spectrum is attributed to the D_2O solution.

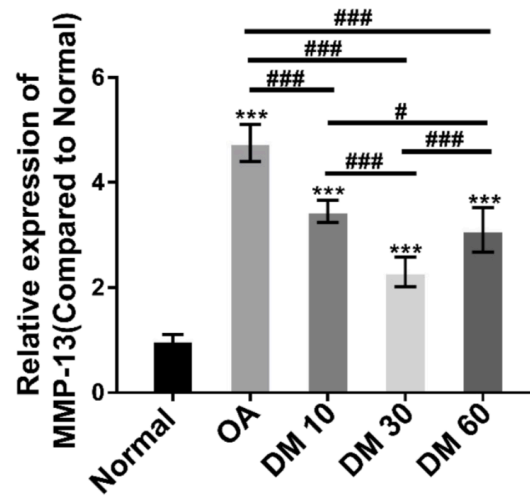


Figure S3.2. Quantitative analysis immunohistochemical staining of MMP-13 in rat cartilage tissue by Image J. Values are presented as means \pm SD, $n=6$. * indicates $P < 0.05$; **, $P < 0.01$; ***, $P < 0.001$, relative to the normal group. #, indicate, $P < 0.05$; ##, $P < 0.01$; ###, $P < 0.001$, relative to the OA group.

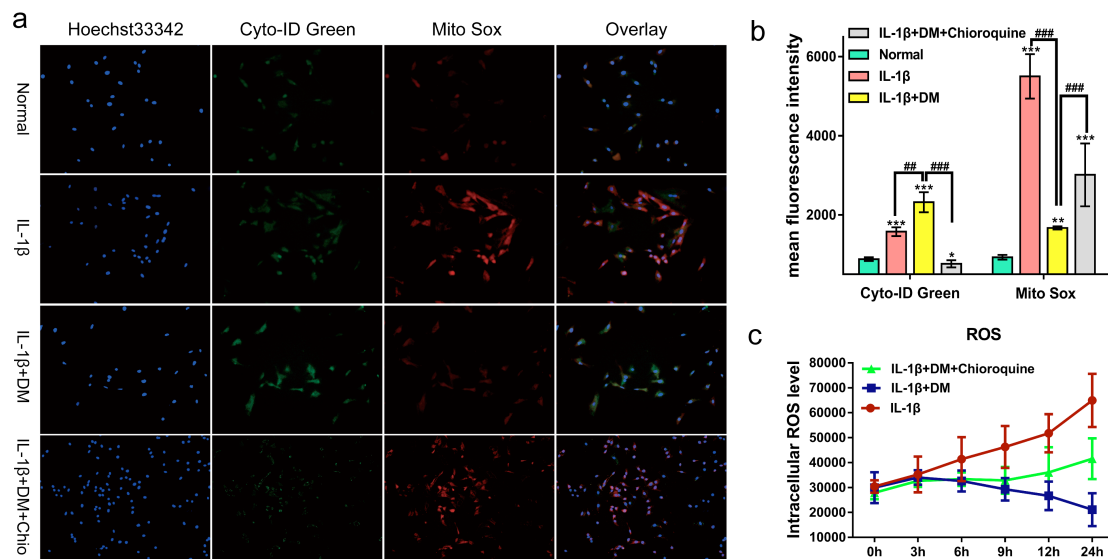


Figure S3.3. Effect of autophagy on free radical scavenging of DM nanoparticles. (a)

Chondrocyte samples concurrently stained with Cyto-ID Green dye and MitoSox Red dye were analyzed by confocal microscopy. (b) The fluorescence intensity of chondrocytes was analyzed by Image J. (c) After treated 30 $\mu\text{g/mL}$ DM Nanoparticles and/or Chloroquine for 0, 3, 6, 9, 12 and 24 h, the chondrocytes were stained with DCFH for 30 minutes, and the intracellular ROS levels were analyzed on a fluorescence microplate reader. IL-1 β (with 10ng/mL IL-1 β); IL-1 β +DM (with 10ng/mL IL-1 β and 30 $\mu\text{g/mL}$ DM nanoparticles); IL-1 β +DM+Chloroquine (with 10 ng/mL IL-1 β , 30 $\mu\text{g/mL}$ DM nanoparticles and 1 $\mu\text{mol/L}$ Chloroquine). Values are presented as means \pm SD. * indicates $P < 0.05$; **, $P < 0.01$; ***, $P < 0.001$, relative to the normal group. #, $P < 0.05$, ##, $P < 0.01$, ###, $P < 0.001$, relative to the IL-1 β +DM group.

Table S3.1. Primer Sequences Used in qRT-PCR experiments

Gene name	Forward primer	Reverse primer
GAPDH	5'-AGGGCCCTGACAACTCTTTT-3'	5'-AGGGGTCTACATGGCAACTG-3'
IL-1 β	5'-TGAGCTCGCCAGTGAAATGA-3'	5'-CATGGCCACAACAACCTGACG-3'
MMP-13	5'-GCCATTACCAGTCTCCGAGG-3'	5'-TACGGTTGGGAAGTTCTGGC-3'
TNF-a	5'-TCAGAGGGCCTGTACCTCAT-3'	5'-GGAGGTTGACCTTGGTCTGG-3'

IL-6	5'-TCTGCGCAGCTTTAAGGAGT-3'	5'-CCCAGTGGACAGGTTTCTGA- 3'
COX-2	5'-ACACTCTATCACTGGCATCC-3'	5'-GAAGGGACACCCTTTCACAT-3'
iNOS	5'GTGTTCCACCAGGAGATGTTG3'	5'CTCCTGCCCCACTGAGTTCCGTT C3'
LC3	5'-GACGTCACCGGGCGAGTTA-3'	5'-GCTGTACCTCCTTACAGCGG-3'
Beclin-1	5'-TCCGGGCTCCCGAGG-3'	5'-GGGGGATGAATCTGCGAGAG- 3'
ATG7	5'-TGGTTACAAGCTTGGCTGCT-3'	5'-TCAAGAACCTGGTGAGGCAC- 3'

C Supporting information for Chapter 4

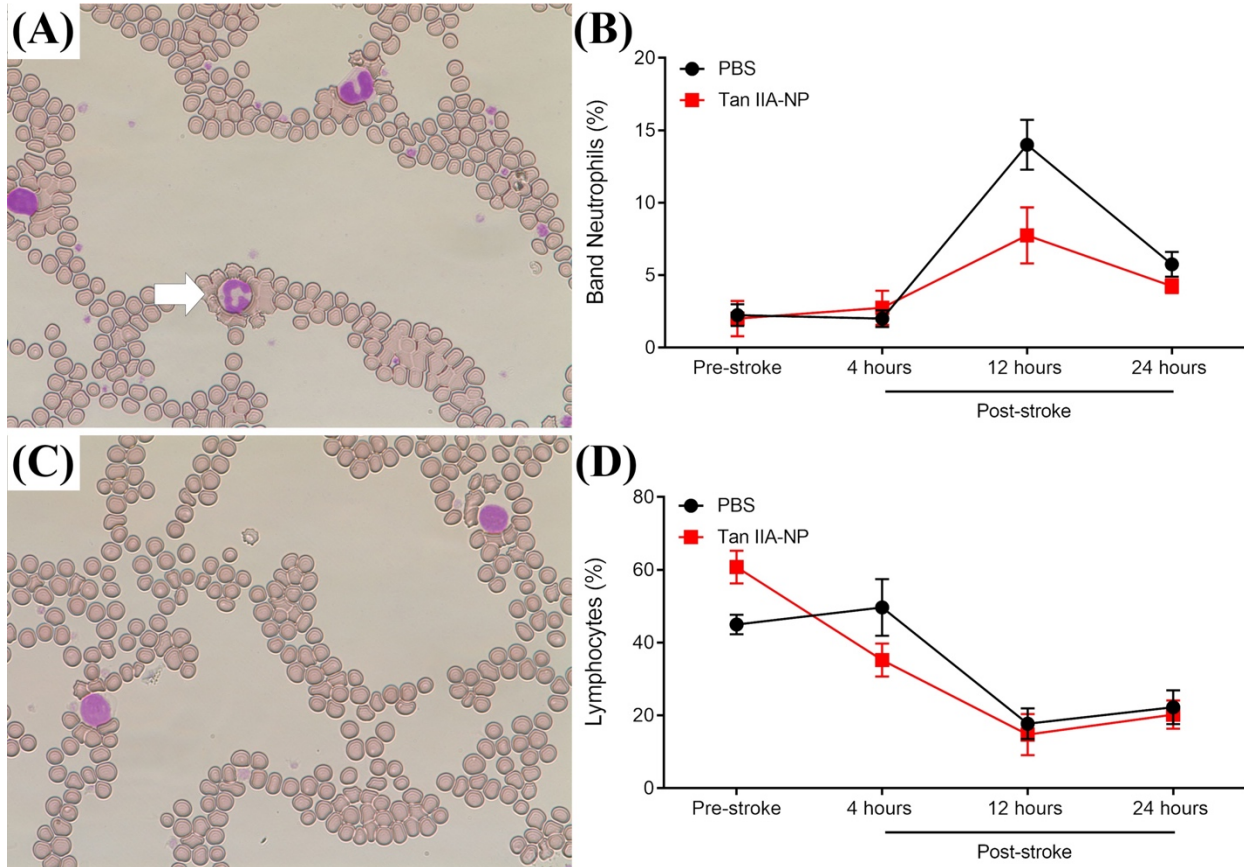


Figure S4.1: Tan IIA-NPs reduce circulating band neutrophils. Band neutrophil (A) and lymphocyte (C) populations were determined in blood samples collected pre-stroke, 4, 12, and 24 hours post-stroke. At 12 hours post-stroke the percentage of circulating band neutrophils was lower in Tan IIA-NP treated pigs than in the PBS control pigs (7.75 ± 1.93 vs. $14.00 \pm 1.73\%$, respectively; B). The percentage of circulating lymphocytes was similar in both treatment groups at all assessed time points (D).